Consortium
for
Small−Scale Modelling

Technical Report No. 4

LLM - the High-Resolving Nonhydrostatic Simulation Model in the DWD Project LITFASS
Part I: Modelling Technique and Simulation Method

by

H.-J. Herzog, U. Schubert, G. Vogel, A. Fiedler

March 2002

DOI: 10.5676/DWD_pub/nwv/cosmo-tr_4

Deutscher
Wetterdienst

MeteoSwiss

Ufficio Generale
per la Meteorologia

Hellenic National
Meteorological Service

Amt für
Wehrgeophysik

Il Servicio Meteorologico
Regionale di ARPA

www.cosmo−model.org

Editors: G. Doms and U. Schättler, Deutscher Wetterdienst, P.O. Box 100465, 63004 Offenbach, Germany
Printed at Deutscher Wetterdienst, Offenbach am Main

LLM – the High-Resolving Nonhydrostatic Simulation Model in the DWD – Project LITFASS.

Part I

Modelling Technique and Simulation Method.

Hans-Joachim Herzog, Ursula Schubert, Gerd Vogel, Adelheid Fiedler and Roswitha Kirchner

Deutscher Wetterdienst, Meteorologisches Observatorium Potsdam

Table of Contents

1 Introduction

At the Deutscher Wetterdienst (DWD) an internal project named LITFASS (Lindenberg Inhomogeneous Terrain - Fluxes between Atmosphere and Surface - a long-term Study) was founded (Müller et al. 1995) and is running up to summer 2001. The aim of that project is to determine by measurement and model simulation area-averaged turbulent fluxes of momentum, heat and moisture representative for an inhomogeneous landscape typical of Central Europe and far enough to the south-east of Berlin.

The project takes advantage of the given infra-structure of the Research Division at DWD, where model research capacity is brought together with considerable and very complex measurement capacity at and over a defined area around the Meteorological Observatory Lindenberg (MOL). LITFASS consists of two main components, a measurement/observation component, (cf. Beyrich 2000) and a numerical simulation component, which serves in a judicious and mutual way to finally help improving the parameterization of subgrid-scale fluxes at and near to the underlying surface for the operational NWP-models. For these models at DWD, and for those elsewhere, one is confronted with the notoric problem that parameterization of subgrid-scale turbulent fluxes is far from being completely solved, and so, for instance, the prediction of 2m-parameters often fails to be satisfactory.

At the end of the project time, after a great, joint achievement and with a noticeable research investment the conclusion may be drawn that due to LITFASS a complex long-term validation system could be established from which the above mentioned task can be tackled with a permanently available measurement system and an appropriate and reliable numerical simulation model. The concern of this paper is to present the numerical simulation component of LITFASS. It represents the 'heart' of the project. From utmost importance is that that model is tightly related to the high-resolution part of the new operational NWP-system, namely to the non-hydrostatic 'Lokal-Modell' (LM), which in the present mode is running with a 7 km horizontal gridpoint distance and 35 vertical layers (cf. Doms and Schättler 1999). Since the model presented here is derived from the LM, it will be designated as LITFASS-Lokal-Modell or LES-Lokal-Modell. The generic abbreviation is LLM. The strict relation to the LM is deliberately organized so as to have a high degree of consistency by using a unified program code, having similar dynamics, numerics and therefore a close reference to the LM-validation from the point of view of the LLM over the defined Lindenberg-observational and LLM-simulation area.

The latter aspect is of particular importance, because the LLM is the simulation tool to determine explicitly the relevant turbulence structures in the integration area as 'true' area-averaged fluxes which are then allowed to compare with the corresponding subgrid-scale fluxes of the LM. This is in the narrow sense the main task of the LLM. It is integrated with a very high horizontal and vertical grid resolution. The integration area covers the planetary boundary layer in the vertical. Its horizontal size corresponds to an area of 14 × 14 km^2 (or even larger: 20 × 20 km^2) in which the MOL is placed. A detailed physiographic description of the underlying surface is taken into account. In contrast to common LES models (e.g. Mason 1994, Mason and Brown 1999, Chlond 1999, Stevens 2000, Kanak et.al. 2000) which are sophisticated instruments to investigate the energy-relevant turbulence structures under clearly defined and controlled conditions (horizontally homogeneous vertical profile of wind, temperature, water content plus small randomized perturbations defining an initial state, homogeneous properties of the underlying surface with prescribed time-independent surface fluxes, or regular or stylized pattern of surface inhomogeneities, double-periodic lateral continuation of the integration domain etc.), the LLM is designed as a 'real-world'-LES model operating under general meteorological conditions.

Demonstrating the unity with the measurement component of LITFASS, the LLM integration mode is characterized by a time-dependent external forcing at the lateral and upper boundary derived from available time sequences of measured vertical profiles, and also by the physical forcing at the surface deduced from temporally variable ground-based measurements of radiation (supported by satellite data) and precipitation, and by observations describing updated surface parameters (vegetation parameters). All the LLM simulations are mainly related to two intensive measurement campaigns in the Lindenberg field. The first one is the 'LITFASS-98 Experiment' (25 May - 30 June 1998) (cf. Beyrich 2000), and the second one is an experiment named 'LINEX-2000' which took place during August/September 2000.

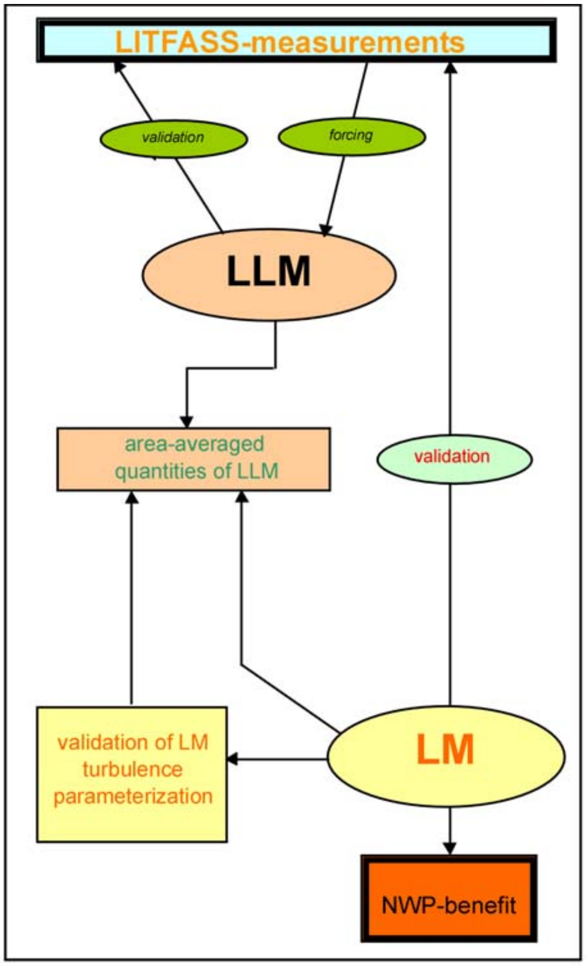

Figure 1.1: The meaning of the DWD project LITFASS from the point of view of bridging observation and simulation by use of the LLM as a tool to validate and help improving NWP models like the LM.

The entire paper is organized as follows. In Chapter 2 the model design is described. It concerns the model equations, the numerics with the vertical and horizontal grid spacing, the specific lateral, upper and lower boundary treatment, a description and explanation of the physics relevant to the LLM integration mode and, finally, the definition and position of the LLM simulation area. Chapter 3 contains a detailed discussion of the LLM-specific incorporation of the three-dimensional subgrid-scale turbulent fluxes concerning both numerical aspects and their parameterization using a prognostic scheme for the turbulent kinetic energy (TKE).

The Chapters 4 and 5 are of particular meaning with respect to the 'real-world' properties of the LLM. Chapter 4 describes how the LLM is externally driven in a lateral and upper boundary zone due to time-sequences of meteorological vertical profiles derived from different measurement sites and vertical sounding systems. In addition to this, the physical forcing of the LLM from the heterogeneous underlying surface is thoroughly discussed in Chapter 5. Here, an important aspect of the LLM integration mode is pointed out. It concerns the careful documentation of the external parameters related to the coupled soil model, and a broader description of methods is given, how to deduce the in homogeneous distribution of surface radiation components and precipitation. The actual time variation of the soil moisture distribution is also taken into account.

In Chapter 6 the model validation is carried out in detail. It reflects the primary claim to have obtained by LITFASS a reliable LLM as a simulation tool on the base of measurements. The following Chapter 7 involves a theoretical consideration. It will be shown in the context of the model equations how area-averaged subgrid- plus grid-scale fluxes are to be formulated in the LLM for referring them to the subgrid-scale fluxes of the LM. As a conclusion, the quantitative comparison of model results from LLM versus LM is particularly demonstrated in Chapter 8. Beyond the given presentation, in an additional Chapter 9 the efforts of programming and program organization on the high-capacity computers at DWD (Cray T3E) and the ECMWF (Fujitsu/VPP 700/116) are dealt with, which have guaranteed the feasibility of the computationally extensive task of LLM simulations. Summing up all partial results, a rather complex and upgraded validation system has been achieved, which makes up the main result of the present state of LLM development. This is shown in Fig. 1.1. It must be understood as a platform ready to start from for systematic and continuous work of NWP activities in the field of parameterization.

The present issue does not contain the entire content listed above, but rather Chapters 1 - 5. These Chapters together built a logical unit. They describe with a fairly completeness the LLM-design including all specific and technical aspects. While writing and preparing the full text we made an incidental decision to publish immediately that part just completed as Part I, before Part II with the following Chapters 6 - 9 will be issued next.

Remark
This paper here submitted to the COSMO community is an improved und updated version of an equally entitled contribution in *Deutscher Wetterdienst, Forschung und Entwicklung, Arbeitsergebnisse Nr.67, Offenbach, Juli 2001.*

2 Model Description

The LLM (LITFASS/LES-Lokal-Modell) is derived from the LM (Lokal-Modell) after having made a deliberate decision in this way. The most important reason for this is obvious, because the LM is the high-resolution model component of the new operational NWP-system at the DWD, and the LITFASS-project was from the very beginning thought to become directly useful to the NWP. As the LM is a nonhydrostatic, compressible model, it is from the point of view of these general properties immediately suitable to be used also as a very high-resolving model within the context of LITFASS. Therefore, the basic equations are, apart from minor modifications, for the LLM identical with the LM equation set. This makes the following model description short enough, where we, however, need the full reference to Doms and Schättler (1999).

2.1 The Model Equations

As discussed above, the LLM equations are borrowed from the LM. We write them here in the following form:

$$\begin{aligned}\frac{\partial u}{\partial t} &= -\frac{1}{\rho}\left(\frac{\partial p'}{\partial x}-\frac{1}{\sqrt{\gamma}}\frac{\partial p_0}{\partial x}\frac{\partial p'}{\partial \zeta}\right)-\left(\frac{\partial K}{\partial x}-vV\right)-\dot{\zeta}\frac{\partial u}{\partial \zeta}-\frac{1}{\rho}\left(\nabla\cdot\underline{\underline{F}}\right)\cdot\underline{e}_1\\ &\quad +M_u^{LB}+M_u^{UB}+D_u \end{aligned}\tag{1}$$

$$\begin{aligned}\frac{\partial v}{\partial t} &= -\frac{1}{\rho}\left(\frac{\partial p'}{\partial y}-\frac{1}{\sqrt{\gamma}}\frac{\partial p_0}{\partial y}\frac{\partial p'}{\partial \zeta}\right)-\left(\frac{\partial K}{\partial y}+uV\right)-\dot{\zeta}\frac{\partial v}{\partial \zeta}-\frac{1}{\rho}\left(\nabla\cdot\underline{\underline{F}}\right)\cdot\underline{e}_2\\ &\quad +M_v^{LB}+M_v^{UB}+D_v \end{aligned}\tag{2}$$

$$\begin{aligned}\frac{\partial w}{\partial t} &= \frac{g}{\sqrt{\gamma}}\frac{\rho_0}{\rho}\frac{\partial p'}{\partial \zeta}+g\frac{\rho_0}{\rho}\left\{\frac{(T-T_0)}{T}-\frac{T_0 p'}{T p_0}+\left(\frac{R_v}{R_d}-1\right)q^v-q^l\right\}\\ &\quad -\left(u\frac{\partial w}{\partial x}+v\frac{\partial w}{\partial y}\right)-\dot{\zeta}\frac{\partial w}{\partial \zeta}-\frac{1}{\rho}\left(\nabla\cdot\underline{\underline{F}}\right)\cdot\underline{e}_3+M_w^{UB}+D_w \end{aligned}\tag{3}$$

$$\begin{aligned}\frac{\partial p'}{\partial t} &= g\rho_0 w-\frac{c_{pd}}{c_{vd}}p\left(D_H-\frac{g\rho_0}{\sqrt{\gamma}}\frac{\partial w}{\partial \zeta}\right)-\left(u\frac{\partial p'}{\partial x}+v\frac{\partial p'}{\partial y}\right)-\dot{\zeta}\frac{\partial p'}{\partial \zeta}\\ &\quad +M_{p'}^{LB}+M_{p'}^{UB} \end{aligned}\tag{4}$$

$$\begin{aligned}\frac{\partial T}{\partial t} &= -\frac{p}{\rho c_{vd}}\left(D_H-\frac{g\rho_0}{\sqrt{\gamma}}\frac{\partial w}{\partial \zeta}\right)-\left(u\frac{\partial T}{\partial x}+v\frac{\partial T}{\partial y}\right)-\dot{\zeta}\frac{\partial T}{\partial \zeta}\\ &\quad +Q_T-\frac{1}{\rho c_{pd}}\nabla\cdot\underline{H}+M_T^{LB}+M_T^{UB}+D_T \end{aligned}\tag{5}$$

$$\begin{aligned}\frac{\partial q^k}{\partial t} &= -\left(u\frac{\partial q^k}{\partial x}+v\frac{\partial q^k}{\partial y}\right)-\dot{\zeta}\frac{\partial q^k}{\partial \zeta}\\ &\quad +Q_k-\frac{1}{\rho}\nabla\cdot\underline{F}_{q^k}+M_{q^k}^{LB}+M_{q^k}^{UB}+D_{q^k} \end{aligned}\tag{6}$$

with $k = v, l$ (denoting water vapour or cloud liquid water, respectively) and with the definitions

$$p = \rho R_d \left\{ 1 + (R_v/R_d - 1)q^v - q^l - q^f \right\} T \tag{7}$$

$$\dot{\zeta} = -\frac{1}{\sqrt{\gamma}} \left(u\frac{\partial p_0}{\partial x} + v\frac{\partial p_0}{\partial y} + g\rho_0 w \right) \tag{8}$$

$$D_H = \left(\frac{\partial u}{\partial x} - \frac{1}{\sqrt{\gamma}}\frac{\partial p_0}{\partial x}\frac{\partial u}{\partial \zeta} \right) + \left(\frac{\partial v}{\partial y} - \frac{1}{\sqrt{\gamma}}\frac{\partial p_0}{\partial y}\frac{\partial v}{\partial \zeta} \right) \tag{9}$$

$$K = \frac{1}{2}\left(u^2 + v^2\right) , \quad V = \frac{\partial v}{\partial x} - \frac{\partial u}{\partial y} + f \tag{10}$$

The formulation makes reference to a defined basic state, which is hydrostatic, dry and at rest. For the temperature and the pressure follows $p = p_0(z) + p'$, $T = T_0 + T'$, and the density of the basic state is $\rho_0 = p_0/(R_d T_0)$. Because the LLM integration domain has a rather limited horizontal extension (see below in 2.6), the horizontal partial derivatives are here symbolized in local cartesian coordinates ($\partial x := a\cos\varphi\partial\lambda$, $\partial y = a\partial\varphi$) instead of spherical ones. Spherical metric terms are therefore dropped, and the variation of the Coriolis parameter is neglected. Furthermore, the equations are formulated with a terrain-following vertical coordinate ζ in such a way, that the momentum equations are related to the physical wind components u, v, w. $\dot{\zeta}$ denotes a contravariant vertical velocity which by use of (8) is related to u, v, w.

The factor $\sqrt{\gamma}$ is defined by $\sqrt{\gamma} = \partial p_0/\partial\zeta$, where $\sqrt{\gamma}/(g\rho_0)$ is the Jacobian of the transformation from the z- to the ζ-coordinate. The horizontal wind divergence D_H, the kinetic energy of the horizontal wind K, and the absolute vorticity V are defined by (9) and (10). The equation of state for a mixture of dry air, water vapour and liquid water is given by (7), q^v and q^l denote the specific contents of water vapour and liquid water, respectively. Thus, (6) consists of two equations for both these moisture variables. The ice phase is not taken into account in the LLM. In contrast to the LM, we consider here the turbulent fluxes of momentum, heat and moisture in all three space directions. Therefore, F denotes in (1), (2), (3) the turbulent momentum flux tensor with its 6 components, and H, F_{q^v} and F_{q^l} the three-dimensional turbulent vector fluxes of heat, water vapour and liquid water. In addition, in the prognostic equations (1), (2), (3), (5), (6) a non-physical computational mixing is implied, where a linear fourth-order horizontal diffusion symbolized by the terms D_ψ ($\psi = u, v, w, T, q^v, q^l$) is applied.

The source terms Q_T and Q_{q^k} need also to be explained. Q_T represents the rate of diabatic heating/cooling due to phase changes of water. The atmospheric effect of radiation is deliberately neglected. This will be discussed from the point of view of the external model forcing in Sections 2.5 and Chapters 4 and 5. The terms Q_{q^v} and Q_{q^l} contain the cloud microphysical source and sink terms and the precipitation flux.

In order to complete the formal model description, the terms M_ψ^{LB} and M_ψ^{UB} must be mentioned. They have no physical background. They represent relaxation terms, acting in a *lateral boundary* zone (=superscript LB) and *upper boundary* model layer (=superscript UB), in order to bring the LLM solution within those boundary zones outward to an externally driving state deduced from measured vertical profiles. This aspect is discussed in Section 2.3 and in Chapter 4. For the rest of symbols in the equations above the meteorological standard notion is valid: R_d and R_v are the special gas constant for dry air and water vapour, respectively, g is the gravity constant, and c_{pd} (c_{vd}) denotes the specific heat capacity at constant pressure (volume).

2.2 Numerical Aspects

As argued above in the description of the continuous LLM equations, we can be brief in discussing the numerics of the LLM as far as taken directly from the LM numerical scheme. This concerns horizontal, vertical and time differences. The horizontal gridpoint position of variables is ordered in a C-grid scheme after the well-known Arakawa nomenclature: At a central point of each gridbox almost all scalar variables inclusively w are placed, while horizontal wind components are positioned halfway from that point as normal components with respect to the box sides (u to 'right' and 'left'; v 'above' and 'below'). The vertical grid is a so called Lorenz-grid. Here, most of variables are placed in the middle of each layer, which is at the so called main levels, while the vertical velocity and also the turbulent vertical flux terms are placed at half levels, which are the interfaces between those layers. The fundamentals of the vertical layer structure can easily be characterized from a strict quotation of Doms and Schättler (1999, cf. Subsection 2.5.3 in the LM-Scientific Documentation).

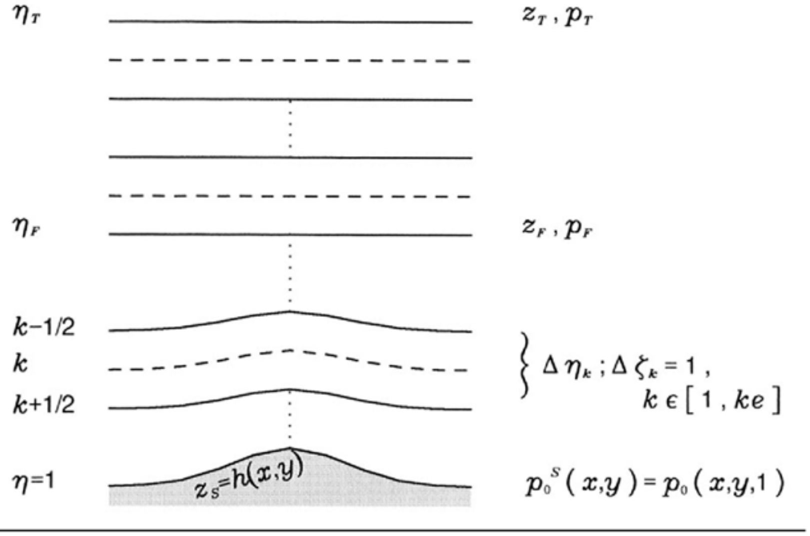

Figure 2.1: Vertical differencing scheme based on the terrain-following hybrid vertical coordinate η with some mapping $\eta = m(\zeta)$ onto the generalized coordinate ζ with the convenient property $\Delta\zeta_k = 1$. The LLM values are $z_T = 3000$ m, $p_T = 693.9075$ hPa, $\eta_T = p_T/p_{SL}$, $p_{SL} = 1000$ hPa, $z_F = 1000$ m, $p_F = 887.27$ hPA and $\eta_F = p_F/p_{SL}$. z_s is the orographic height which is also given by a standard surface pressure distribution $p_0^s(x,y)$ on $\eta = 1$.

An important aspect of the terrain-following vertical coordinate used in the LLM is specified as a pressure-based hybrid coordinate that involves a defined height of $z_F = 1000$ m separating the entire vertical domain into a terrain-following part below and a pure z-coordinate above it (Fig. 2.1). Thus, the lower model boundary is a coordinate surface formed by the highly resolved orography plus a seasonally varying field of the displacement height. The upper boundary is assumed at 3000 m height. This vertical depth of the LLM is divided into 39 layers, where the layers nearest to the lower boundary are very thin. The thickness is spreaded from 4 m to 25 m in the first two-hundred meters with 15 layers. Above, the layer thickness increases gradually up to 100 m at 425 m height where it remains so up to about 1000 m. From there the resolution becomes still coarser with a thickness of 150 m up to model top height (Tab. 2.1).

With a horizontal mesh width of $\Delta \simeq 100$ m the aspect ratio $\alpha = \Delta z/\Delta$ varies between $1/25 \leq \alpha \leq 3/2$. The vertical depth of 3000 m has been fixed after test integrations of a 52-layer model version with a model top height chosen for sake of caution at 5000 m for

k	$z(m)$	$p_0(z)$ (Pa)
1	3000.0	69390.8
2	2850.0	70704.6
3	2700.0	72039.5
4	2550.0	73395.5
5	2400.0	74773.5
6	2250.0	76173.1
7	2100.0	77594.8
8	1950.0	79039.1
9	1800.0	80506.1
10	1650.0	81006.1
11	1500.0	83509.5
12	1350.0	85046.7
13	1200.0	86607.8
14	1050.0	88193.2
15	925.0	89533.2
16	825.0	90617.7
17	725.0	91713.3
18	625.0	92820.2
19	525.0	93939.5
20	425.0	95068.2
21	350.0	95923.1
22	300.0	96496.7
23	266.0	96888.4
24	233.0	97269.9
25	200.0	97652.6
26	175.0	97943.5
27	150.0	98235.0
28	125.0	98527.3
29	105.0	98761.7
30	90.0	98937.8
31	77.5	99084.7
32	65.0	99231.9
33	52.5	99379.2
34	42.5	99497.2
35	32.5	99615.3
36	22.5	99733.5
37	15.0	99822.3
38	9.0	99893.3
39	4.0	99525.8
40	0.0	100000.0

Table 2.1: Vertical structure of layers. The index $k \in [1, 40]$ counts the half-levels with associated heights and basic-state pressure values.

a convective case. The outcome has indicated that a 3000 m upper boundary height is sufficient.

The time differencing scheme used for the LLM integration is completely taken from the LM-code as the dominant scheme amongst three options. In brief, we selected the mode-splitting time integration method originally proposed by Klemp and Wilhelmson (1978), refined by Skamarock and Klemp (1992) and completed by further implicit manipulations. In this line the model equations are split up into a slowly varying part and a fast one. The former consists of horizontal advection, vertical advection, turbulent diffusion in all three space directions, horizontal computational mixing and source/sink terms. The water balance equations for vapour and liquid water and the turbulent kinetic energy equation are exclusively slow equations, while the momentum equations for the wind components u, v, w, the temperature equation and the prognostic perturbation pressure equation have also a fast part.

In the slow equations/equation parts different terms are treated differently as follows. The horizontal advection is integrated by use of the leap-frog scheme. The vertical advection and the vertical turbulent flux terms are approximated by an implicit Crank-Nicholson scheme, and the horizontal turbulent flux terms, the computational mixing (fourth-order diffusion), and the source/sink-terms as well, are formulated by a simple forward scheme. The corresponding time step (large time step) is chosen $\Delta t = 2$ s with respect to the horizontal gridpoint distance $\Delta = 96.5$ m. The entire time marching per Δt consists in extrapolating the fast equation part with a small timestep $\Delta\tau$ several times over each time span $2\Delta t$ keeping the before determined slow tendencies fixed over this intervall. The fast-mode part involves, apart from the slow tendencies of momentum, temperature and perturbation pressure, all terms representing inertial-gravity waves and sound-waves. Those terms describing vertically propagating waves are treated implicitly in order to prevent any dependence on high vertical grid resolution. Thus, the choice of the small time increment $\Delta\tau$ is governed by the linear stability condition $\Delta\tau \leq \Delta/(\sqrt{2}\,c_s)$ with an estimate for the sound speed $c_s = (R_d(c_{pd}/c_{vd}) \times 303K)^{1/2}$. With respect to the relation $\Delta\tau = 2\Delta t$ follows $N = 22$ as the number of small timesteps over twice the large step giving $\Delta\tau = 0.182$ s.

Each time step Δt ends with the application of a Robert-Asselin time filter followed by the upper and lateral boundary relaxation technique in order to match the inner LLM solution with an external forcing. The latter aspect is of special interest for the LLM integration mode and will therefore be discussed separately in the next Section.

Lest we ignore possibly a time integration scheme being less time consuming than the mode splitting scheme, it was mandatory for us to test further options available for the LM. Thomas et al. (1998 a, b) had developed a three-dimensional semi-implicit time integration method suitable for a non-hydrostatic compressible model which they also introduced in the LM program code. Their method rests on a GMRES (General Minimal Residual Krylov Iterative Solver) algorithm and seemed to promise computational advantages. Therefore, rather time-expensive tests of that scheme applied to the LLM have been carried out (Herzog and Fiedler 1999). The computational efficiency of the fully 3D semi-implicit (SI) time-scheme versus the above described split-explicit (SE) scheme has been investigated by comparable real data runs for the 14.06.97 day. Unfortunately, the outcome of these runs was negative. Compared to the SE reference run with the 'slow mode'-time step of $\Delta t = 2$ s the SI runs led to an unexpected computational overhead. The slow convergence rate of the elliptic solver could not be influenced by an enlarged Krylow space dimension and an aspect ratio $\Delta z/\Delta$ chosen always smaller than unity. The conclusion had to be drawn that the SI-scheme cannot compete with the SE-scheme in case of the LLM which simulates the planetary boundary layer with its inherent three-dimensional micro-scale structures. For a comparably larger-scale LM computational problems discussed seem different (Saito et al. 1998).

2.3 Lateral and Upper Boundary Techniques

Integrating a very high-resolving model over a rather limited area like the LLM, one is confronted with an extremly underestimated problem in view of external atmospheric information needed to drive the model via its lateral boundaries and the upper boundary as well. We assume the relatively low-resolved boundary data provided from measurements (cf. Chapter 4) to be in general variable in time. For that reason it is important to have some desirable control of such boundary forcing. Particularly, the effect of local physical forcing in the near-surface Planetary Boundary Layer domain of the LLM should be maintained as far as possible. Trying to find a solution, a pragmatic, engineering strategy is reasonable to be pursued. Unfortunately, there is no standard method that has been demonstrated to be satisfactory for the wide-spread spectrum of atmospheric motions, and so for the LLM problem neither.

In view of this, rather extended numerical experiments have been made both as transparent simplified tests and as complex real-data model runs, in order to come to a decision for an acceptable compromise. Basically, two types of lateral boundary methods have been tested. The first type is the *radiation condition* in its approximate form (Orlanski 1976). The principal difficulty to incorporate a radiation condition into a realistic model is that the speed normal to the boundary is generally unknown. The approach (Miller and Thorpe 1981) locally diagnoses the normal speed component, whereas in Klemp and Wilhelmson (1978) it is specified to be a representative phase speed of internal gravity waves. In each case tested, the approach remains approximative and is linear. The boundary condition becomes, however, necessarily nonlinear which means that this type of method works successful only when the solution is dominated by a single wave. In all other cases we are mainly interested in, the solution is severely polluted with errors. By the way, there is also no convincing theoretical support for the radiative idea, since the original variables are not characteristic. The outcome of numerous test integrations gave us a sufficient reason to discard this type of lateral boundary technique from further consideration.

The second type uses a certain *adjustment or 'sponge' effect* in a zone next to the lateral boundary (Davies 1976, Perkey and Kreitzberg 1976, Chen 1973, Miyakoda and Rosati 1977 etc.). Our interest is to apply a method of that type which was introduced in a particularly easy and therefore practicable form by Kallberg and Gibson (1977) starting from Davies' original approach. The so called 'Davies-Kallberg'-technique is a preferable method which is always available because of its ease to be used in general situations, where the boundary data are time-dependent. The property of easy use is also a very important aspect in view of parallel programming. Nevertheless, one must not ignore the inevitable shortcomings of the Davies-Kallberg boundary relaxation or blending method from which dynamical imbalances in the relevant boundary adjustment zone may be produced.

Before we start describing a version of the Davies-Kallberg technique applied to the LLM regime, some remarks concerning a hybrid method are given. The latter one has also been tested because there were arguments in literature (Arakawa 1984) for a pragmatic solution, in which a scheme that is nonreflective – at least for idealized cases – is combined with some adjustments near the boundary. An attempt was therefore made to adapt such a method to the compressible, non-hydrostatic LLM with its specific time-splitting technique. The working hypothesis was to introduce also a mode splitting for the radiative scheme. In doing so, the acoustic-gravity equation part is treated with open boundaries at each short timestep. For the advection part, however, a mixed scheme is applied: At the outflow boundary points a radiative scheme is used again, but now for the advective wind speed, while at outflow points a modified Davies-scheme operates.

In short, this rather sophisticated scheme works well in case of simplified flow situations, where outflow points and inflow points can easily be separated (e. g. the most simple case of a diagonal basic current). In more general cases problems emerge at boundary points, where the relaxation scheme and the radiative scheme influence and conflict with each other in an uncontrolled way. Therefore, this method was also discarded, which has finally led to our choice of a 'pure' Davies-Kallberg technique. That method is applied in the LLM in a modified form.

The prototype for each prognostic LLM equation may be written

$$\frac{\psi_j^{(\tau+1)} - \psi_j^{(\tau-1)}}{2\Delta t} = RHS_j^{(\tau-1,\tau,\tau+1)} - \mu_j \left(\psi_j - \psi_j^B\right)^{(\tau+1)} . \tag{11}$$

In a more symbolized form the tendency is approximated by a centered time difference with $2\Delta t$. In $RHS_j^{(\tau-1,\tau,\tau+1)}$ all terms of each equation are absorbed, and the second term on the r. h. s. represents the lateral boundary relaxation term of interest. Towards the boundary the inner LLM solution is forced to become equal to the external solution represented by the boundary data ψ_j^B. The index j numbers the gridpoints of a grid row inwards and normal to the boundary point $j = 0$.

In line with the philosophy of that relaxation term, abbreviated by M_ψ^{LB} in the model equations, the relaxation coefficient μ_j is a prescribed function of distance of an inner gridpoint

j to the boundary point. At the boundary the coefficient becomes infinity and it approaches to zero in the inner region defining so the prescribed width of the lateral boundary relaxation zone. The time levels $\tau-1$, τ, $\tau+1$ in (11) indicate in a common way of notation the different time difference approximations (leap-frog centered, forward and implicit treatment of involved terms) in the prototype equation. As known from many descriptions of Kallberg's approach, the equation type (11) can be brought into an astonishing simple linear form

$$\psi_j \;=\; (1-\alpha_j)\,\psi_j^{LLM} + \alpha_j \psi_j^B \,, \tag{12}$$

where the internal LLM data ψ_j^{LLM} – not influenced by the relaxation term M_ψ^{LB} – are linearly combined with the external driving boundary data ψ_j^B to produce per timestep the boundary data adjustment of the inner solution in terms of ψ_j. Far from being ideal the simple procedure is thought to avoid most of dangerous reflections and contaminations originating from overestimated and generally unfitted boundary data. The blending weights α_j are related to the relaxation coefficients μ_j by

$$\alpha_j \;=\; \frac{2\Delta t\mu_j}{1+2\Delta t\mu_j} \;. \tag{13}$$

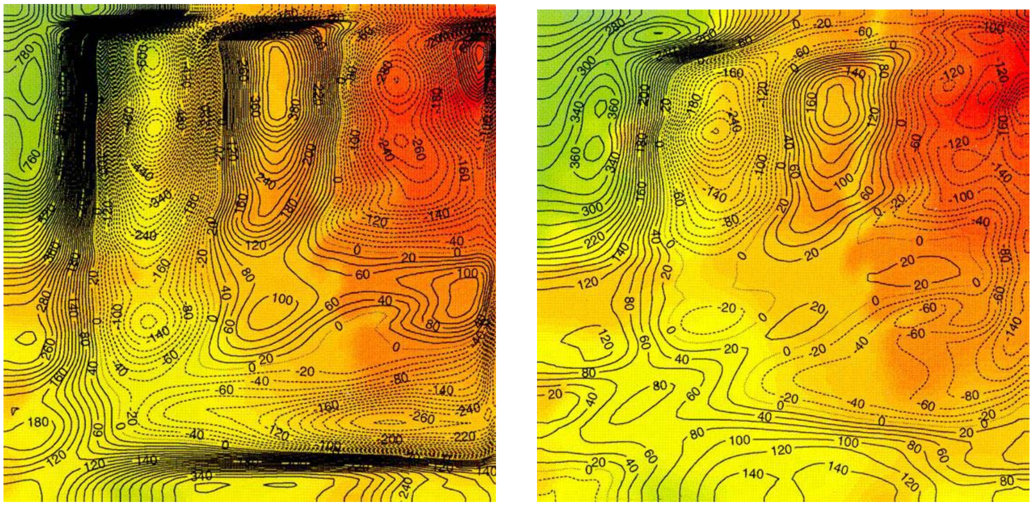

a=0.5, max = 884mm/s, min = -675mm/s

a=0.25, max = 388mm/s, min = -302mm/s

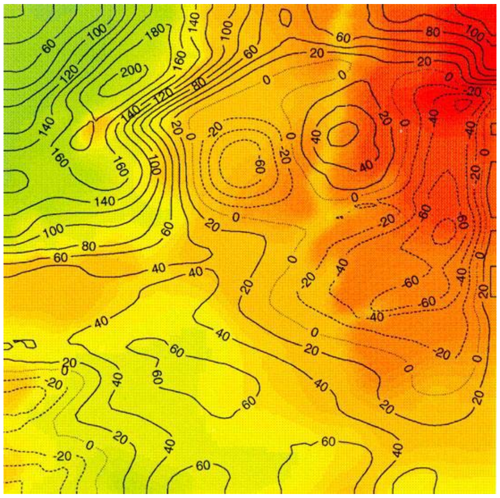

a=0.125, max = 206 mm/s, min = -86 mm/s

Figure 2.2: Horizontal section of vertical velocity w at altitude z = 1500 m after an one-hour integration over a LLM subdomain of 81 × 81 gridpoints assuming a basic flow over the real orography with U = 10 m/s. The w-field is shown for three values of the Kallberg-parameter a. Top left: a = 0.5, top right: a = 0.25, bottom left: a = 0.125.

For the α_j-weights follows $0 \leq \alpha_j \leq 1$ with $\alpha_{j=0} = 1$. Formula (13) is, however, unpractical to be used. Since Kallberg (1977) it is common practice to apply an ad hoc formula

$$\alpha_j \;=\; 1 \;-\; \tanh(aj)\,; \quad j = 0, 1, 2, ..., \tag{14}$$

which describes a damping curve like (13). The parameter a determines the essential decrease of that curve because of $(\partial\alpha/\partial j)_{j=0} = -a$. In many limited area models (e.g. EM, DM, LM) the value $a = 0.5$ has shown to be sufficient. To find out an appropriate steepness of the α_j-curve for the LLM with its significantly higher grid resolution, some numerical experimentation was carried out starting from the default value $a = 0.5$. The result is shown in Fig. 2.2. It suggests an α_j-curve with a sufficiently weaker slope. Thus, $a = 0.125$ is chosen further on instead of 0.25 or 0.5. Fig. 2.3 demonstrates the weight curves (14) for those three slope values.

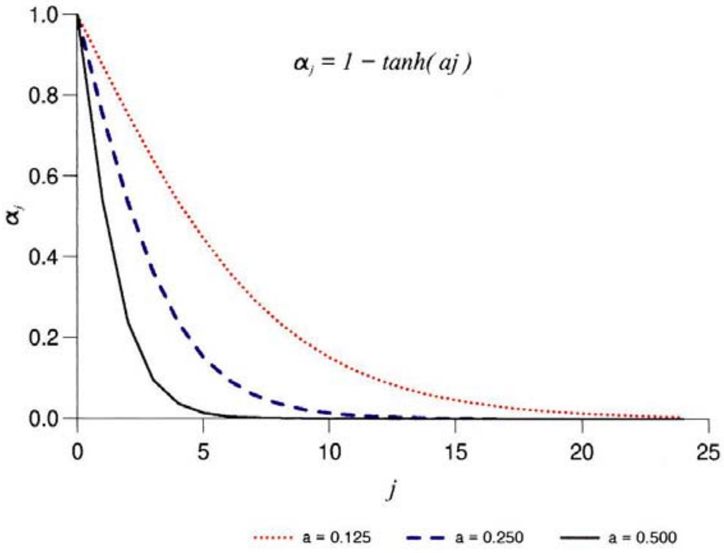

Figure 2.3: Boundary weight curve (Equation (14), see text) as a function of distance of an inner gridpoint j to the boundary point $j = 0$ for three different slope parameters a = 0.5, 0.25, 0.125.

In order to obtain more insight from the result shown in Fig. 2.2, it is illuminating to take into account also the first and second derivative of relation (12):

$$\frac{\partial\psi}{\partial x} = (1-\alpha)\frac{\partial\psi^{LLM}}{\partial x} + \alpha\frac{\partial\psi^{B}}{\partial x} - \frac{\partial\alpha}{\partial x}(\psi^{LLM} - \psi^{B})\,, \tag{15}$$

$$\frac{\partial^2\psi}{\partial x^2} = (1-\alpha)\frac{\partial^2\psi^{LLM}}{\partial x^2} + \alpha\frac{\partial^2\psi^{B}}{\partial x^2} - 2\frac{\partial\alpha}{\partial x}\left(\frac{\partial\psi^{LLM}}{\partial x} - \frac{\partial\psi^{B}}{\partial x}\right) - \frac{\partial^2\alpha}{\partial x^2}(\psi^{LLM} - \psi^{B})\,. \tag{16}$$

x is a continuous coordinate measured in grid distance units. While the blending formula (12) is actually applied per timestep for prognostic variables ψ $(= u, v, T, p)$, one obtains, in effect, due to (15) and (16), no similar blending of $\partial\psi/\partial x$ (which, for instance, is related to the horizontal wind divergence and vorticity) and $\partial^2\psi/\partial x^2$ (related to the horizontal gradient of vertical motion, respectively). It can be seen that the dissimilarity is fundamentally marked by the always existing difference between inner solution (ψ^{LLM}, $\partial\psi^{LLM}/\partial x$) and the external one ($\psi^{B}$, $\partial\psi^{B}/\partial x$). (15) and (16) tell us furthermore that the significant

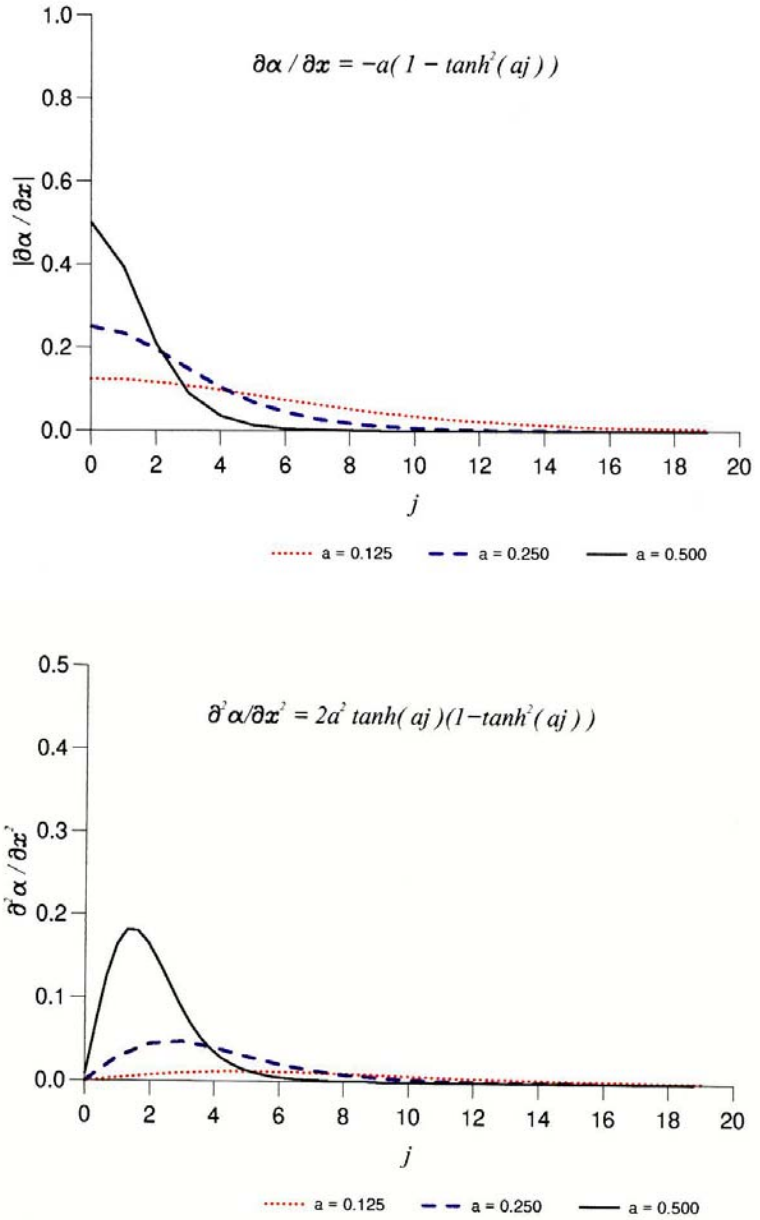

Figure 2.4: The first (top) and second (bottom) derivatives of the Kallberg boundary weight function α (x is measured in grid distance units) for $a = 0.5, 0.25, 0.125$.

difference is multiplied by $\partial\alpha/\partial x$ and $\partial^2\alpha/\partial x^2$. By an appropriate choice of the weights α we are, however, able to keep the unwanted effect due to those terms rather small. This depends obviously on the choice of the parameter a. Fig. 2.4 shows in addition to Fig. 2.3 the functions

$$\frac{\partial\alpha}{\partial x} = -a(1 - \tanh\{ax\}), \quad \frac{\partial^2\alpha}{\partial x^2} = 2a^2 \tanh\{ax\}(1 - \tanh^2\{ax\})\,. \tag{17}$$

The conclusion from Fig. 2.3 together with Fig. 2.4 is that $a = 0.125$ is the best value to be used in case of the LLM. The strong gradient of w in a short distance from the boundary, as shown in Fig. 2.2 for $a = 0.5$, may be explained by use of the continuity equation summing up the gradient of the horizontal wind divergence from the earth surface to the height z.

In this way the vertically accumulated effect of the $\partial\alpha/\partial x$ and $\partial^2\alpha/\partial x^2$-terms in (16) is involved. It is not demonstrated here from the background experiment of Fig. 2.2 that the near-boundary gradient of vertical motion shown for $a = 0.5$ is actually not observed on the lowest model levels but will be formed and amplified with increasing height. All our experimentation with numerous real data cases so far have indicated that with $a = 0.125$ the unwanted gradients discussed do vanish.

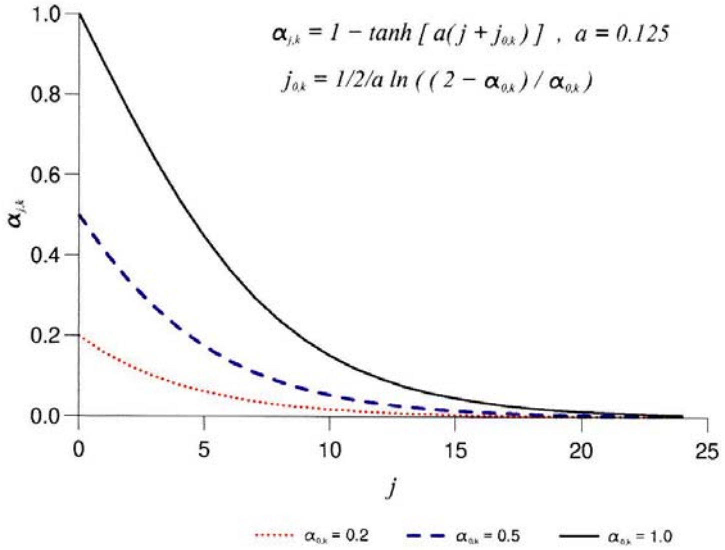

Figure 2.5: Plot of vertically varying weight function $\alpha_{j,k}$ showing how in the LLM the external boundary data influence is reduced downwards by using a phase parameter $\alpha_{0,k}$ in the intervall $0.2 \leq \alpha_{0.k} \leq 1$ (see text).

In order to complete the description of the LLM-specific lateral boundary technique another engineering component is added to the original Kallberg approach. The motivation follows from the decision to use the weight curve parameter $a = 0.125$. Though necessary, some nuisance might come from the relatively far inward reaching influence of boundary data information connected with a low-steepness curve. To alleviate possible problems from this, the following vertically varying weight functions differing from (14) are introduced:

$$\alpha_{j,k} \;=\; 1 \;-\; \tanh\left[a(j + j_{0,k})\right] \;, \tag{18}$$

with a phase parameter

$$j_{0,k} \;=\; \frac{1}{2a}\ln\left(\frac{2-\alpha_{0,k}}{\alpha_{0,k}}\right) \;.$$

k is the vertical model level index, and a is always equal to 0.125 (Fig. 2.5). The new parameters $\alpha_{0,k}$ are user-prescribed values, which for the lowest LLM levels $14 \leq k \leq 39$ (cf. Tab.2.1) are linearly distributed in the range $0.2 \leq \alpha_{0,k} \leq 1$ by $\alpha_{0,k} = 1 - 0.8(k-14)/39-14)$. This empirical operation, entirely determined from experimentation, makes sure that the influence of the always not exactly adapted boundary data is in the planetary boundary layer towards the earth surface gradually diminished, where, however, the near-surface turbulent fluxes produced in the LLM are allowed to remain dominating. Instead of (12) a similar blending formula, now also depending on k, must be applied, which evaluates the above described weights (18) instead of (14),

$$\psi_{j,k} \;=\; (1-\alpha_{j,k})\,\psi_{j,k}^{LLM} + \alpha_{j,k}\psi_{j,k}^{B}\,. \tag{19}$$

It follows from this philosophy that in any case of $\alpha_{0,k} < 1$ also internal LLM information is needed at the boundary points which from the numerical integration is not directly available. Therefore, a simple linear extrapolation as computational boundary condition is additionally applied.

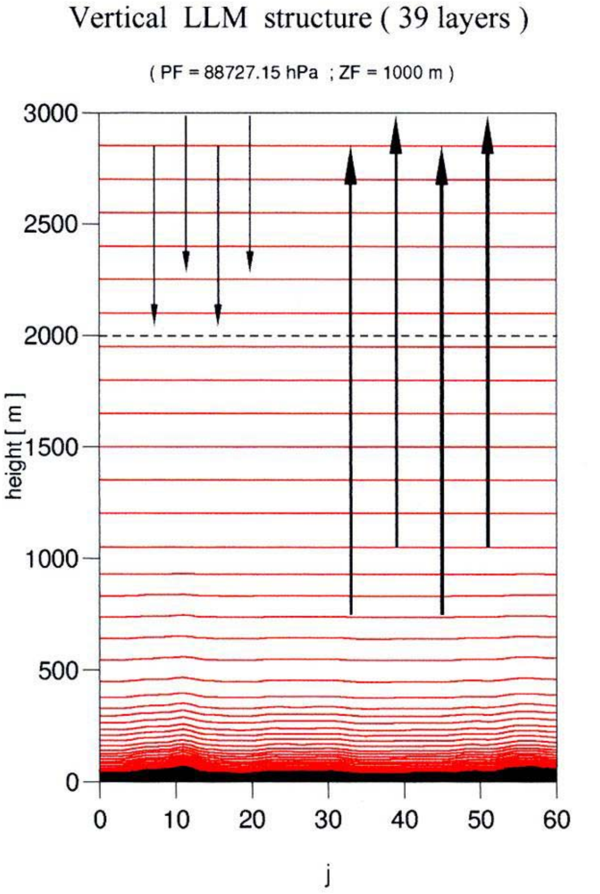

Figure 2.6: Position of the Rayleigh damping layer connected with vertical layering of the LLM.

In the following the *upper boundary technique* will be explained. It is directly adopted from the LM-scheme. The method is similar to the lateral boundary technique, which is a Rayleigh-damping mechanism. In the model equations (1) - (6) this is symbolized by the terms M_{ψ}^{UB}. Here, the vertical motion w is included. The original motivation for that sort of upper boundary relaxation is to allow an upper lid condition $w = 0$ at the top of the model, from which artificial gravity wave reflection can take place. The Rayleigh damping method prevents that by absorption of energy of those waves penetrating upward through an upper absorption zone before arriving the top elevation. In case of the LLM, the purpose of that method is, however, twofold. In addition, the technique is thought to be an adaptation method as at the lateral boundary in order to match the inner solution also in an upper boundary zone with an outer solution which serves as a driver from measured data in the free atmosphere (cf. Chapter 4). Similar to equation (11) the mechanism rests here on a prognostic equation like that

$$\frac{\psi_k^{(\tau+1)} - \psi_k^{(\tau-1)}}{2\Delta t} = \cdots - \nu_k^{rd}\left(\psi_k - \psi_k^B\right)^{(\tau+1)} . \tag{20}$$

In (20) only a relaxation term M_ψ^{UB} is of interest. The vertical model level index k emphasizes its operation in vertical direction. ν_k^{rd} is a relaxation coefficient corresponding to a reciprocal relaxation time. After Ikawa and Saito (1991) it is assumed to have the form

$$\nu_k^{rd} = \frac{1}{2N_{rd}\Delta t}\left[1 - \cos\left(\pi \frac{z_k - z_{rd}}{z_T - z_{rd}}\right)\right] . \tag{21}$$

The parameters in formula (21) are specified as follows: $\Delta t = 2$ s, $N_{rd} = 10$, $z_T = 3000$ m and $z_{rd} = 2000$ m. They define a Rayleigh damping layer being 1000 meters thick and resolved by the 7 uppermost layers, $k \in [1, 7]$ (Fig. 2.6). From the cosine-profile function follows an increasing absorption effect towards the model top. There, the damping effect reaches its maximum. The parameter $N_{rd} = 10$ means, that the perturbation $(\psi - \psi^B)$ will be reduced to its e^{-1}-th part at the top height $z_T = 3000$ m after 10 large LLM timesteps. For levels below 2000 meters the method is ineffective. The practical execution of the Rayleigh damping is similar to the lateral boundary technique, where a blending like (11) or (19) is applied. The associated weight function is here $\alpha_k = 2\Delta t \nu_k^{rd} / (1 + 2\Delta t \nu_k^{rd})$.

A radiative scheme instead of the presently applied method is still under development. The hydrostatic radiation condition after Klemp and Durran (1983) and Bougeault (1983) successfully introduced in the former DM/HRM (Herzog 1995, Binder and Herzog 1995), seems not directly suited in the non-hydrostatic and compressible world of LM/LLM.

2.4 Lower Boundary Condition and Forcings

For the sake of completeness, the lower boundary condition/treatment must be added here after having described the LLM-specific lateral and upper boundary technique in the previous Section. Because the lower bounding surface is the earth surface (without deeper thinking how it is defined from the point of view of modelling), it is assumed rigid. Frictional forces are important at that surface. Therefore, the classical adherence condition or non-slip condition holds there. Consequently, the horizontal wind components u and v vanish at the surface. Since the contravariant vertical motion $\dot{\zeta}$ in the LM/LLM-equations always vanishes then, it follows from equation (8) a vanishing physical vertical velocity, that is $w = 0$.

The boundary layer processes are of vital interest in LLM modelling. Thus, the turbulent fluxes of momentum, heat and moisture at the surface must be available as exact as possible. For their determination the surface temperature and moisture must be known. These parameters again are determined from an LLM-coupled prognostic soil model 'terra'. That model is also incorporated in the present operational LM version and was already operating in the former DWD-models EM and DM/HRM (Jacobsen and Heise 1982). Intensive work is underway to insert for the thermal part, still being an 'extended force-restore' method, a higher resolved heat conduction equation.

All the external parameters needed have been derived in case of the LLM problem from a detailed physiographic description of the landscape around Lindenberg. Furthermore, horizontally distributed, time-varying fields of precipitation and short-wave plus long-wave radiation balance at the earth surface determined from measurements constitute the physical forcing of LLM from the underlying surface. This aspect is of greatest importance for reasonable and successful LLM simulations. Therefore, the LLM forcing from the earth surface is the matter of thorough discussion in Chapter 5.

2.5 Model Physics Different to LM

In view of the fact that near-surface turbulent fluxes are very sensitive to forcing from the underlying surface, that process must be kept as close as possible to reality. This will be achieved by using real surface precipitation and radiation balance fields for that forcing as mentioned above in Section 2.4. The consequence is, however, to make an operation in both the cloud-precipitation scheme and the radiation parameterization scheme as they are originally available from the LM.

In contrast to well-defined LES studies taking into account cloud-radiation interaction and a precipitation scheme, the LLM real-case simulations cannot operate with that philosophy. Although forming of clouds and precipitation is in the LLM allowed, the precipitation flux reaching the earth is ignored and replaced by a real-data precipitation field. Furthermore, the radiation scheme available from the LM is even completely discarded. The radiative long- and short-wave balance field at the surface is exclusively deduced from measurements and supported by satellite information (cf. Chapter 5). The input-frequency of the radiation balance and of the surface precipitation field amounts to 10 minutes. In this way the ground surface and therefore the soil model 'terra' perceives radiation and precipitation as would be obtained from properly simulated atmospheric conditions like cloudiness and radiation in and over the LLM integration domain.

A weak point of this strategy might be the omission of any radiation scheme in the atmospheric part of the LLM. This is just taken into the bargain in order to avoid an erroneous radiative heating/cooling from insufficient simulations of all conditions influencing the radiation processes. To keep on the right way, it is tacitly assumed that the long-wave radiative effect on the temperature field is implied in the measured vertical profiles from which the LLM is driven from outside with an 1 hour-updating frequency. Summing up that, the reduction in the precipitation and radiation parameterization in case of LLM studies is believed to be compensated by sets of real forcing data where these processes are implicitly contained.

In the LLM also the soil model 'terra' (already commented in Section 2.4) is incorporated, which is directly taken from the LM system. For a detailed description we refer to the LM Scientific Documentation (Doms and Schättler 1999, Chapter 10). Its use in the LLM and minor adjustments are detailed in Chapter 5, where the forcing of LLM will be discussed thoroughly.

The most important sub-grid parameterization in the LLM is undoubtedly an adequate turbulence scheme. Because this physical component has been developed as a primary task of the LLM-development, it deserves to be documented in the present report in the following Chapter 3.

2.6 Specification of the Horizontal Integration Area

This Section deals with a technical issue concerning the exact size and placement of the horizontal grid net . Its fixation must be explained from a historical situation when the 'Deutschland-Modell' (DM) was in operational use. At the beginning of the LITFASS-project there was a common agreement to think of an integration area for the LLM having exactly the size of a DM-gridbox. The gridbox selected encloses the location of the Lindenberg Observatory and contains almost all measurement places in it (Beyrich 2000). The size of that gridbox (so called 'Lindenberg gridbox') is defined by a mesh width of the DM which is $(\Delta\lambda')_{DM} = (\Delta\varphi')_{DM} = 0.125^\circ$ defining an area of about 14×14 km^2. The primes refer to a rotated latitude-longitude coordinate system (λ', φ') with its rotated north pole at a location $\lambda = 170.0°W$, $\varphi = 32.5°N$ given in geographical coordinates.The same rotated system is valid for the LM (cf. Doms et al. 1999, Chapter 4; Schättler and Doms 1998, p. 27), and so for the LLM. The DM-gridpoint is positioned exactly in the centre of the Lindenberg gridbox. It coincides with an LM-gridpoint and an LLM-gridpoint as well. In terms of a C-grid valid for DM, LM and LLM this gridpoint is a so called 'mass'-point, where almost all model variables and parameters but the horizontal wind components are placed. (We tacitly make the agreement that all gridpoints considered are the mass-points of a C-grid where the places of u and v are automatically related to.)

The coordinates of the central gridpoint are given by $\lambda' = 2.5°$ and $\varphi' = -5.25°$, corresponding to $\lambda = 14.0617°W$ and $\varphi = 52.1752°N$. For the transformation $(\lambda', \varphi') \leftrightarrow (\lambda, \varphi)$ we refer to Schrodin (1995). The size of the standard LLM integration area is shown in Fig. 2.7 a,b. It is a square having 145 × 145 gridpoints. Therefore, the LLM mesh width can be found from $(\Delta\varphi)_{DM}/144 = (\Delta\varphi)_{LLM} = (\Delta\varphi)_{LLM} \simeq 96.53$ m (assuming $a = 6371229$ m for the earth radius and 111.19892 km for a 1°-distance on a great circle). With a gridpoint indexing $i \in [1, 145]$ in west-east direction and $j \in [1, 145]$ in south-north direction, the central point is determined by $(i, j) = (73, 73)$. In the following the coordinates of the four corner points are noted.

LLM domain corners	λ' (°)	ϕ' (°)	λ (°E)	ϕ (°N)
lower left $(i = 1, j = 1)$	2.4375	- 5.3125	13.9544	52.1165
upper left $(i = 1, j = 145)$	2.4375	- 5.1875	13.9663	52.2413
lower right $(i = 145, j = 1)$	2.5625	- 5.3125	14.1567	52.1091
upper right $(i = 145, j = 145)$	2.5625	- 5.1875	14.1692	52.2339

Besides this standard area another option of integration area has been agreed with the people of the measurement branch, which is the so called 'extended Lindenberg' - area having all local measurement points enclosed and more possibilities of testing the LLM. Compared to the standard area it is extended about 2km to south and north and 4km to north and west. The total is about 20×20 km^2 covered by 199 × 199 gridpoints. It corresponds to the entire area shown in Fig. 2.7. In order to note at least the relative placement of that 'extended area', the corner points of the 'standard area' are to be noted in terms of the 'extended area' indices $i_{ext} \in [1, 199]$ and $j_{ext} \in [1, 199]$:

$$\begin{aligned} (1,1) &= (37,19)_{ext} \\ (1,145) &= (37,163)_{ext} \\ (145,1) &= (181,19)_{ext} \\ (145,145) &= (181,163)_{ext} \end{aligned}$$

Finally, the location of the corner points of the central LM-gridbox ($\simeq 7 \times 7$ km^2) is given in terms of the 'standard area' gridpoint indices $i \in [1, 145]$ and $j \in [1, 145]$: (37,37), (37,109), (109,37) and (109,109).

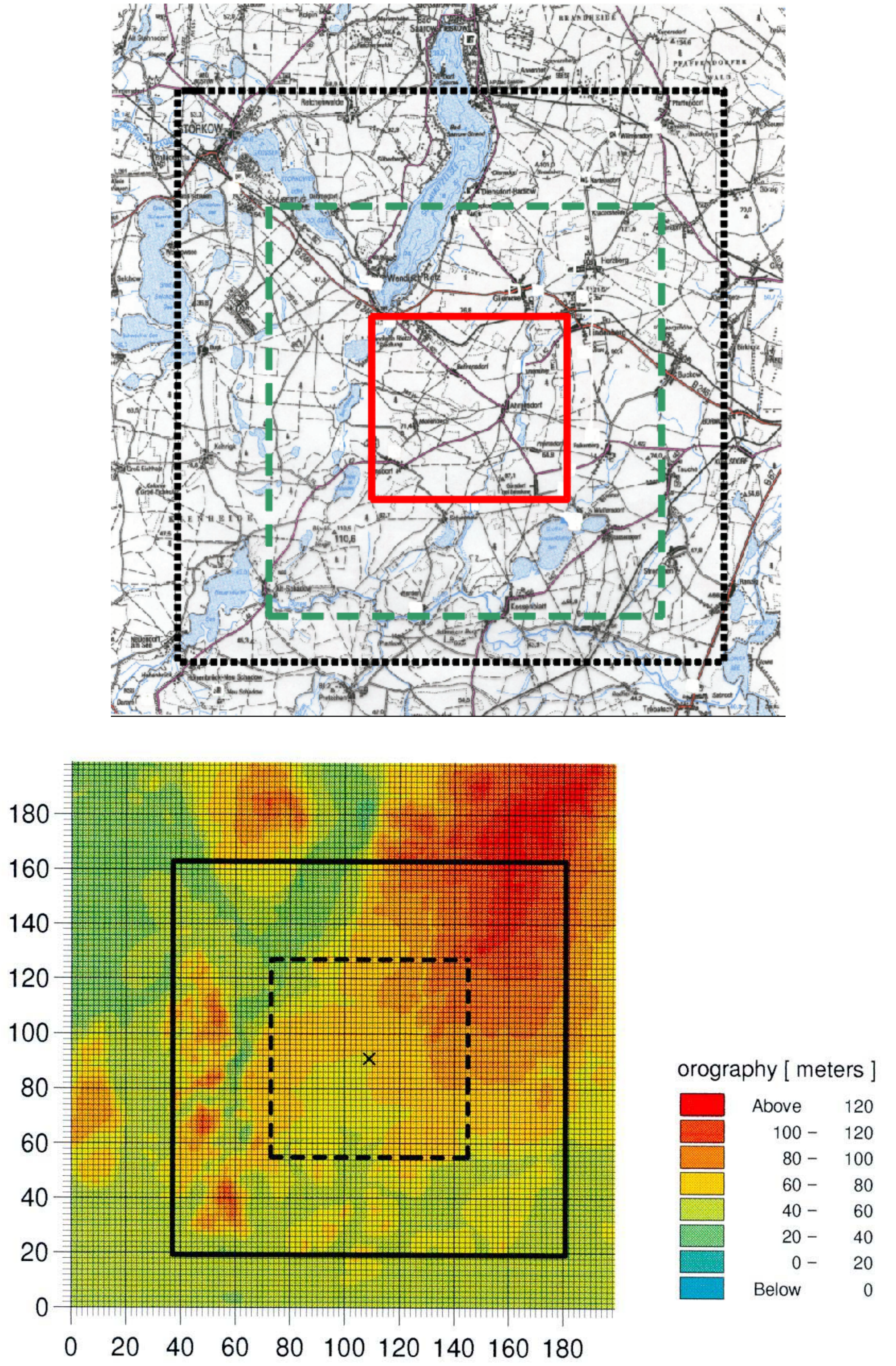

Figure 2.7: Position of the LLM integration area laid over a map of Lindenberg (top) and over a grid net with twice the mesh width and underlaying orography.

Top: Black broken line – boundary of the extended area ($\sim 20 \times 20$ km^2, 199 × 199 gridpoints). Green dashed line – boundary of standard area ($\sim 14 \times 14$ km^2, 145 × 145 gridpoints). Red full line – boundary of centered LM grid box ($\sim 7 \times 7$ km^2).

Bottom: Whole area corresponding to the extended area, with standard area (black line) and LM grid box (dashed line) in it. The cross point marks the central LM gridpoint.

3 Parameterization of Subgrid-Scale Turbulence

The parameterization of subgrid-scale (actually subfilter) turbulent processes, also called a subgrid-scale (SGS) model, is of particular meaning for the LES-like LLM. Because such an SGS model was not available from the LM system, we had to do an extra development. For this, a completely three-dimensional flux scheme was necessary to implement instead of only vertical turbulent flux terms as included in the given LM scheme. This part of work was with considerable effort an extension of the original LM code. In a further step, the SGS model itself, which must be written as function of the resolved scales (unaffected by a filter application), seems to be easier for the LLM compared to LM. Namely, in the latter the parameterization embraces more complex processes than in case of the LLM. The SGS model we decided to use is a prognostic turbulent kinetic energy (TKE) scheme taking into account the three space directions. This is documented in the following. In a first step, the SGS model is described, while in the following step the numerical incorporation is exactly demonstrated for the first time.

3.1 The SGS - TKE Model

We start from the LLM equation set (1)-(3), (5), (6) (see Section 2.1), which is rewritten here, emphasizing the turbulent flux terms:

$$\begin{aligned}
\frac{\partial u}{\partial t} &= \ldots - \frac{1}{\rho}\left(\nabla \cdot \underline{\underline{F}}\right) \cdot \underline{e}_1 \\
\frac{\partial v}{\partial t} &= \ldots - \frac{1}{\rho}\left(\nabla \cdot \underline{\underline{F}}\right) \cdot \underline{e}_2 \\
\frac{\partial w}{\partial t} &= \ldots - \frac{1}{\rho}\left(\nabla \cdot \underline{\underline{F}}\right) \cdot \underline{e}_3 \\
\frac{\partial T}{\partial t} &= \ldots - \frac{1}{\rho c_{pd}} \nabla \cdot \underline{H} \\
\frac{\partial q^k}{\partial t} &= \ldots - \frac{1}{\rho} \nabla \cdot \underline{F}_{q^k}
\end{aligned}$$

For the following the three-dimensionality of those terms is completely retained. $\underline{\underline{F}}$ denotes the turbulent momentum flux tensor with its 6 independent components τ_{ij} $(i,j = 1,2,3)$, and $\underline{H}$ and $\underline{F}_{q^k}$ are the vector fluxes of heat and water components. From these fragments of equations we change, as often usual, to the more convenient tensor notation:

$$\frac{\partial u_i}{\partial t} = \cdots - \frac{1}{\rho}\frac{\partial \tau_{ij}}{\partial x_j}\,, \tag{22}$$

$$\frac{\partial X^n}{\partial t} = \cdots - \frac{1}{\rho}\frac{\partial Y_j^n}{\partial x_j}\,, \tag{23}$$

where there is $(u_i) = (u, v, w)$, $(\tau_{ij}) = \underline{\underline{F}}$, $(X^1, X^2) = (T, q^k)$, $(Y_j^1) = \underline{H}$ and $(Y_j^1) = \underline{F}_{q^k}$ for $i = 1,\ 2,\ 3$ and $j = 1,\ 2,\ 3$. The fluxes are specified by use of a first-order closure assumption. It means that the fluxes are set proportional to the local gradient multiplied by a local turbulence coefficient:

$$\tau_{ij} = -\rho K_m \left(\frac{\partial u_i}{\partial x_j} + \frac{\partial u_j}{\partial x_i}\right)\,, \tag{24}$$

$$Y_j^1 \;=\; -c_p \pi \rho K_h \frac{\partial \Theta_v}{\partial x_j}\,, \qquad Y_j^2 \;=\; -\rho K_h \frac{\partial q^k}{\partial x_j}\,. \tag{25}$$

For this specification we refer, for instance, to Mason (1994), and Mason and Brown (1999). There, a distinction is drawn between a turbulence coefficient for momentum, K_m, and heat, K_h, respectively. Here, ρ is density, Θ_v denotes virtual potential temperature and π is the Exner function. The SGS-TKE model is determined by specifying the turbulence coefficients after Prandtl and Kolmogorov:

$$K_m \;=\; \phi_m \Lambda \sqrt{\overline{e}}\,, \qquad K_h \;=\; \phi_h \Lambda \sqrt{\overline{e}}\,. \tag{26}$$

Apart from having still undetermined factors ϕ_m, ϕ_h, that $K_{m,h}$-specification needs the knowledge of turbulent kinetic energy, $\overline{e}$, and some assumption, how to set the turbulence length scale Λ. In order to come to a closure of the system, we need a relation/equation, which allows the calculation of TKE from the resolved/filtered fluid regime. For that purpose we invoke the prognostic TKE-equation which may be written

$$\frac{\partial \overline{e}}{\partial t} + u_j \frac{\partial \overline{e}}{\partial x_j} \;=\; \delta_{i3} \frac{g}{\overline{\Theta}_v} (\overline{u_i' \Theta_v'}) - \overline{u_i' u_j'} \frac{\partial \overline{u_i}}{\partial x_j} - \frac{\partial (\overline{u_j' e})}{\partial x_j} - \frac{1}{\rho} \frac{\partial (\overline{u_i' p'})}{\partial x_i} - \varepsilon\,. \tag{27}$$

Here, the TKE is defined by

$$\overline{e} \;=\; \frac{1}{2} (\overline{u_i' u_i'}) \tag{28}$$

and $e = u_i' u_i'/2$. We quote Stull (1988, p. 152) for the derivation of that TKE-equation (27). The physical meaning of all terms, and so the definition of variables in it, can also be found in Stull's bible of turbulence quoted. It is important to note here that the derivation of (27) implies the Boussinesq-approximation, the hypothesis of Reynolds averaging and the assumption of incompressibility and shallow convection. This is not strictly in agreement with the more general LM/LLM-equations and, we may think that it does not need so. Here, we remind of experiences that errors in the parameterization of SGS processes in case of an LLM-like resolution do not influence the resolved scales in a significant manner. In view of determining K_m and K_h according to (26a,b), one needs in a further step suitable parameterizations in (27). Here, the 'flux-gradient' specification, like (24) and (25), is also used,

$$\overline{u_i' u_j'} \;=\; -K_m \left(\frac{\partial u_j}{\partial x_i} + \frac{\partial u_i}{\partial x_j} \right) \tag{29}$$

$$\overline{u_i' \Theta_v'} \;=\; -K_h \frac{\partial \Theta_v}{\partial x_i} \tag{30}$$

in order to make the buoyant production term and the shear production term applicable. The term describing the turbulent transport of TKE and the pressure correlation term are collected,

$$\frac{\partial (\overline{u_j' e})}{\partial x_j} + \frac{1}{\rho} \frac{\partial (\overline{u_j' p'})}{\partial x_j} \;\simeq\; \frac{\partial}{\partial x_j} \overline{\left(u_j' e + \frac{u_j' p'}{\rho} \right)}\,, \tag{31}$$

in order to parameterize the resulting flux also in accordance with a gradient specification:

$$\overline{u_j' \left(e + \frac{p'}{\rho} \right)} \;=\; -2 K_m \frac{\partial \overline{e}}{\partial x_j}\,. \tag{32}$$

For the latter we refer to Stevens et al. (1999). Finally, as usual the dissipation term is set equal to

$$\varepsilon = c_\varepsilon \frac{(\overline{e})^{3/2}}{\Lambda}\,. \tag{33}$$

The length scale Λ will be defined later. The value of c_ε is assumed different in literature. Here, we adopt $c_\varepsilon = 0.93$ (Stevens et al. 1999). In that way the following TKE-equation is found to be useful for our purpose:

$$\frac{\partial \overline{e}}{\partial t} + u_j \frac{\partial \overline{e}}{\partial x_j} = -K_h N^2 + K_m S^2 + 2\frac{\partial}{\partial x_j}\left(K_m \frac{\partial \overline{e}}{\partial x_j}\right) - c_\varepsilon \frac{(\overline{e})^{3/2}}{\Lambda}\,. \tag{34}$$

(The tacit change of denotation for the resolved/filtered variables must be noted, that is $\overline{u}_j = u_j$, $\overline{\Theta}_v = \Theta_v$, etc.) There we have introduced the Brunt-Väisälä frequency squared

$$N^2 = \frac{g}{\Theta_v}\frac{\partial \Theta_v}{\partial z}\,, \tag{35}$$

and the definition

$$S^2 = 2S_{ij}S_{ij} = \left(\frac{\partial u_i}{\partial x_j} + \frac{\partial u_j}{\partial x_i}\right)\frac{\partial u_i}{\partial x_j} = \frac{1}{2}\left(\frac{\partial u_i}{\partial x_j} + \frac{\partial u_j}{\partial x_i}\right)^2\,, \tag{36}$$

where S_{ij} is the strain tensor and S^2 the deformation squared.

By solving the TKE from the prognostic equation (34), we would be able to determine K_m, K_h according to (26a,b), provided the coefficients ϕ_m and ϕ_h are known. Therefore, we think about these factors how to determine them as some reasonable functions of stability and having then a stability-dependent Prandtl-number

$$Pr = \frac{K_m}{K_h} = \frac{\phi_m}{\phi_h}\,. \tag{37}$$

In order to come to a reasonable solution, we start as an interlude from another more simple SGS-model, that is the extension of the Smagorinsky (1963) model presented by Brown et al. (1994) (cf. also Mason and Brown 1999). We call it, in brief, a Smagorinsky-SGS-model. It is characterized by the following K_m-, K_h-specification:

$$K_m = \lambda^2 S F_m(Ri)\,, \quad K_h = \lambda^2 S F_h(Ri)\,. \tag{38}$$

The stability dependence is imposed through the functions F_m and F_h. These functions are based on observations which are loosely the 'Kansas data'. S is defined in (36), and λ is the length scale in the Smagorinsky model. That length scale may be rewritten

$$\lambda = c_s \Lambda \tag{39}$$

defining the constant c_s. We assume here $c_s = 0.25$. Λ is a length scale closely related to the grid spacing as a measure of the numerical resolution envisaged and may be identical with the length scale Λ in the Prandtl-Kolmogorov specification (26). Following Brown et al. (1994) the stability functions F_m and F_h are specified as separate functions for statically unstable conditions and statically stable conditions, and it is ensured that these functions match in value (not in gradient) at $Ri = 0$. Anticipating our three-dimensional TKE-model, the local Richardson number may be defined as

$$Ri = \frac{N^2}{S^2} \tag{40}$$

with reference to (35) and (36).

For the unstable case, $Ri < 0$, one assumes

$$F_m = (1 - 16Ri)^{1/2}\,, \quad F_h = (1 - 40Ri)^{1/2} Pr_N^{-1}\,, \tag{41}$$

while in case of stability, $0 \leq Ri \leq Ri_c$,

$$F_m = (1 - Ri/Ri_c)^4\,, \quad F_h = (1 - Ri/Ri_c)^4 (1 - 1.2Ri) Pr_N^{-1} \tag{42}$$

is used. The critical value of Ri is taken $Ri_c = 0.25$. The value $Pr_N^{-1} = 0.7$ which is the Prandtl number in neutral condition is chosen consistent with the Kansas data and LES experiments. In order to specify the length scale Λ we deviate from Brown et al. (1994) and introduce

$$\Lambda = (\Delta x \Delta y \Delta z)^{1/3} f(a_1, a_2)\,. \tag{43}$$

The function $f(a_1, a_2)$ serves as a corrective factor in case of an anisotropic grid and has been proposed by Scotti et al. (1993, 1997). If $\Delta_1, \Delta_2, \Delta_3$ are the dimensions of a grid box, where we can always assume $\Delta_1 \leq \Delta_2 \leq \Delta_3$, the two aspect ratios of the given grid are defined as

$$a_1 = \frac{\Delta_1}{\Delta_3}\,, \quad a_2 = \frac{\Delta_2}{\Delta_3}\,. \tag{44}$$

For the present LLM grid configuration (cf. Section 2.2) the relevant aspect ratio $\Delta z/\Delta$ (with $\Delta x = \Delta y = \Delta$ and $(\Delta x \Delta y \Delta z)^{1/3} = \Delta^{2/3} \Delta z^{1/3}$) ranges from 1/25 to 3/2. Thus, we meet with a 'pancake-like' grid ($\Delta z/\Delta \leq 1$) and a 'pencil-like' grid ($\Delta z/\Delta > 1$). Scotti et al. (1993) have shown on the base of theoretical arguments for isotropic turbulence that there exists an estimate for the grid anisotropy function as follows

$$f(a_1, a_2) \simeq \cosh\left[\frac{4}{27}(\ln^2 a_1 - \ln a_1 \ln a_2 + \ln^2 a_2)\right]^{1/2}\,. \tag{45}$$

In case of $\Delta z/\Delta \leq 1$ ($\Delta_1 = \Delta z, \Delta_2 = \Delta_3 = \Delta$):

$$\begin{aligned} a_1 &= \Delta z/\Delta \leq 1 \quad a_2 = 1 \\ f(a_1, a_2) &= f(\Delta z/\Delta) = \cosh(0.3849 \ln[\Delta z/\Delta])\,. \end{aligned} \tag{46}$$

In case of $\Delta z/\Delta > 1$ ($\Delta_1 = \Delta_2 = \Delta, \Delta_3 = \Delta z$):

$$\begin{aligned} a_1 &= \Delta/\Delta z = a_2 \\ f(a_1, a_2) &= f(\Delta/\Delta z) = \cosh(0.3849 \ln[\Delta/\Delta z])\,. \end{aligned} \tag{47}$$

In case of grid isotropy we have $f = 1$, of course. By now, our Smagorinsky SGS model is sufficiently described. In passing, it was the first SGS model we had incorporated in the LLM scheme. Here it serves as a special case of the general TKE model, in order to deduce the specifications of ϕ_m and ϕ_h in (26) from that. In this line, we recall the Smagorinsky model to be the equilibrium limit of the prognostic TKE equation (34). It can actually be shown the equivalence of the K_m-, K_h-specifications (38) and (26), provided that the equilibrium TKE equation

$$K_m S^2 - K_h N^2 - c_\varepsilon \frac{(\overline{e})^{3/2}}{\Lambda} = 0 \tag{48}$$

is valid. From that special case the equality

$$K_m = \phi_m \Lambda \sqrt{\overline{e}} = c_s^2 \Lambda^2 S F_m(Ri)\,, \quad K_h = \phi_h \Lambda \sqrt{\overline{e}} = c_s^2 \Lambda^2 S F_h(Ri)\,, \tag{49}$$

is used to find the TKE

$$\overline{e} = \phi_m c_\varepsilon^{-1} \Lambda^2 S^2 \left(1 - Pr^{-1} Ri\right)\,, \tag{50}$$

which is, therefore associated to the Smagorinsky model. The Prandtl-number is

$$Pr = \frac{\phi_m}{\phi_h} = \frac{F_m}{F_h}\,. \tag{51}$$

With $-\infty \le Ri \le Ri_c = 0.25$ and $Pr = Pr_N = 0.7$ for $Ri = 0$ it follows the stability dependence of Pr in a range

$$0.4427 \le Pr \le 1 \tag{52}$$

in accordance with the Kansas data-fitted stability functions F_m and F_h. By inserting (50) in (49), an expression for ϕ_m is then easily found:

$$\phi_m = c_s^{4/3} c_\varepsilon^{1/3} F_m^{2/3}(Ri) \left(1 - Pr^{-1} Ri\right)^{-1/3}\,. \tag{53}$$

That result is now used to be valid in specifying ϕ_m in (26) for the general problem to solve the prognostic TKE equation (34). ϕ_h follows by use of (51) from the known functions F_m and F_h. The grid scale length is found to be

$$\Lambda = \Delta^{2/3} \Delta z^{1/3} \begin{cases} \cosh[0.3849 \ln(\Delta z/\Delta)]\,, & \Delta z/\Delta \le 1\,, \\ \cosh[0.3849 \ln(\Delta/\Delta z)]\,, & \Delta/\Delta z < 1\,. \end{cases} \tag{54}$$

3.2 Numerical Treatment

We focus our attention first on the incorporation of the three-dimensional 'divergence of turbulent flux'-terms in the given numerical LM-scheme. For this reason, we write down the discretized form of those terms as parts of the momentum, heat and moisture transport equations. For the momentum equations we have

$$\left(\frac{\partial u}{\partial t}\right)^{(n)} = \cdots - \frac{1}{\overline{\rho^{(n)}}^{\lambda} a \cos\varphi} \left(\delta_\lambda \tau_{11} + \cos\varphi\, \delta_\varphi \tau_{12}\right)^{(n,n-1)} + \frac{g}{\overline{\sqrt{\gamma}}^{\lambda}} \overline{\left(\frac{\rho_0}{\rho^{(n)}}\right)}^{\lambda} \left(\delta_\zeta \tau_{13}\right)^{(n-1,n,n+1)} \tag{55}$$

$$\left(\frac{\partial v}{\partial t}\right)^{(n)} = \cdots - \frac{1}{\overline{\rho^{(n)}}^{\varphi} a \cos\varphi} \left(\delta_\lambda \tau_{12} + \cos\varphi\, \delta_\varphi \tau_{22}\right)^{(n,n-1)} + \frac{g}{\overline{\sqrt{\gamma}}^{\varphi}} \overline{\left(\frac{\rho_0}{\rho^{(n)}}\right)}^{\varphi} \left(\delta_\zeta \tau_{23}\right)^{(n-1,n,n+1)} \tag{56}$$

$$\left(\frac{\partial w}{\partial t}\right)^{(n)} = \cdots - \frac{1}{\overline{\rho^{(n)}}^{\zeta} a \cos\varphi} \left(\delta_\lambda \tau_{13} + \cos\varphi\, \delta_\varphi \tau_{23}\right)^{(n,n-1)} + \frac{g}{\overline{\sqrt{\gamma}}^{\zeta}} \overline{\left(\frac{\rho_0}{\rho^{(n)}}\right)}^{\zeta} \left(\delta_\zeta \tau_{33}\right)^{(n-1,n,n+1)} \tag{57}$$

Here, the slow tendencies are approximated as

$$\left(\frac{\partial\psi}{\partial t}\right)^{(n)} = \frac{\psi^{(n+1)} - \psi^{(n-1)}}{2\Delta t}, \quad \psi = (u, v, w, T, q^k)\,. \tag{58}$$

Δt is the 'large' timestep. For the 6 turbulent stress components we assume

$$\tau_{11} = -\frac{\left(\rho\overline{K}_m^{\varphi}\right)^{(n)}}{a\cos\varphi} 2\delta_\lambda u^{(n-1)} \tag{59}$$

$$\tau_{12} = -\frac{\left(\overline{\rho K}_m^{\lambda,\varphi}\right)^{(n)}}{a\cos\varphi}\left(\delta_\lambda v^{(n-1)} + \cos\varphi\delta_\varphi u\right)^{(n-1)} \tag{60}$$

$$\tau_{13} = -\frac{\left(\overline{\rho K}_m^{\lambda}\right)^{(n)}}{a\cos\varphi}\delta_\lambda w^{(n-1)} + g\overline{\left(\overline{\left[\frac{\rho_0\rho^{(n)}}{\sqrt{\gamma}}\right]}^{\zeta} K_m^{(n)}\right)}^{\lambda}\left(\beta_d^{+}\delta_\zeta u^{(n+1)} + \beta_d^{-}\delta_\zeta u^{(n-1)}\right) \tag{61}$$

$$\tau_{23} = -\frac{\left(\overline{\rho K}_m^{\varphi}\right)^{(n)}}{a}\delta_\varphi w^{(n-1)} + g\overline{\left(\overline{\left[\frac{\rho_0\rho^{(n)}}{\sqrt{\gamma}}\right]}^{\zeta} K_m^{(n)}\right)}^{\varphi}\left(\beta_d^{+}\delta_\zeta v^{(n+1)} + \beta_d^{-}\delta_\zeta v^{(n-1)}\right) \tag{62}$$

$$\tau_{22} = -\frac{\left(\rho\overline{K}_m^{\zeta}\right)^{(n)}}{a} 2\delta_\varphi v^{(n-1)} \tag{63}$$

$$\tau_{33} = g\overline{\left(\overline{\left[\frac{\rho_0\rho^{(n)}}{\sqrt{\gamma}}\right]}^{\zeta} K_m^{(n)}\right)}^{\zeta} 2\left(\overline{\beta_d^{+}}^{\zeta}\delta_\zeta w^{(n+1)} + \overline{\beta_d^{-}}^{\zeta}\delta_\zeta w^{(n-1)}\right) \tag{64}$$

We have strictly adopted here and in the following formulae all the rules and definitions of differencing and averaging operators applied in the LM numerics as documented in the work of Doms and Schättler (1999). In a similar way the turbulent fluxes of sensible heat and moisture are considered in the following approximations.

$$\left(\frac{\partial T}{\partial t}\right)^{(n)} = \cdots - \frac{1}{\rho^{(n)} a\cos\varphi}\left(\delta_\lambda h_1 + \cos\varphi\delta_\varphi h_2\right)^{(n,n-1)} + \frac{g}{\sqrt{\gamma}}\left(\frac{\rho_0}{\rho^{(n)}}\right)\left(\delta_\zeta h_3\right)^{(n-1,n,n+1)} \tag{65}$$

$$h_1 = -\frac{\left(\overline{\pi\rho K}_h^{\lambda}\right)^{(n)}}{a\cos\varphi}\delta_\lambda\left(T/\pi\right)^{(n-1)} \tag{66}$$

$$h_2 = -\frac{\left(\overline{\pi\rho K}_h^{\varphi}\right)^{(n)}}{a}\delta_\varphi\left(T/\pi\right)^{(n-1)} \tag{67}$$

$$h_3 = g\left(\overline{\left[\frac{\pi\rho_0\rho^{(n)}}{\sqrt{\gamma}}\right]}^{\zeta} K_h^{(n)}\right)\left(\beta_d^{+}\delta_\zeta(T/\pi)^{(n+1)} + \beta_d^{-}\delta_\zeta(T/\pi)^{(n-1)}\right) \tag{68}$$

$$\left(\frac{\partial q^k}{\partial t}\right)^{(n)} = \cdots - \frac{1}{\rho^{(n)} a\cos\varphi}\left(\delta_\lambda F_1^k + \cos\varphi\delta_\varphi F_2^k\right)^{(n,n-1)} + \frac{g}{\sqrt{\gamma}}\left(\frac{\rho_0}{\rho^{(n)}}\right)\left(\delta_\zeta F_3^k\right)^{(n-1,n,n+1)} \tag{69}$$

$$F_1^k = -\frac{\left(\overline{\rho K_h}^{\lambda}\right)^{(n)}}{a\cos\varphi}\delta_\lambda(q^k)^{(n-1)} \tag{70}$$

$$F_2^k = -\frac{\left(\overline{\rho K_h}^{\varphi}\right)^{(n)}}{a}\delta_\varphi(q^k)^{(n-1)} \tag{71}$$

$$F_3^k = g\left(\overline{\left[\frac{\rho_0\rho^{(n)}}{\sqrt{\gamma}}\right]}^{\zeta} K_h^{(n)}\right)\left(\beta_d^{+}\delta_\zeta(q^k)^{(n+1)} + \beta_d^{-}\delta_\zeta(q^k)^{(n-1)}\right) \tag{72}$$

In these terms of interest, metrical simplifications are implied, that is, metrical terms both related to spherical coordinates and the generalized, terrain-following vertical coordinate are dropped. As can be seen, all horizontal turbulent diffusion terms are treated by forward-in-time differences, and so those terms of vertical momentum fluxes arising from the consideration of horizontal inhomogeneities. The rest of vertical diffusion terms is treated partially implicit by a Crank-Nicholson scheme. This leads together with the vertical advection terms to a tridiagonal vertical structure equation to be solved by a Gaussian elimination procedure as provided from the LM code. In case of the LLM the given method has also been applied due to the τ_{33}-term in the w-equation (57).

On this level the numerical treatment considered is independent of any specified SGS model. With the preparations shown the numerics of the SGS-TKE model must now be put forward. Therefore, we start from the TKE equation (34), which is here rewritten in spherical coordinates neglecting metrical terms and by use of the LM-specific vertical coordinate. We have instead of (34)

$$\begin{aligned}\frac{\partial\overline{e}}{\partial t} = & -\frac{1}{a\cos\varphi}\left(u\frac{\partial\overline{e}}{\partial\lambda} + v\cos\varphi\frac{\partial\overline{e}}{\partial\varphi}\right) - \dot{\zeta}\frac{\partial\overline{e}}{\partial\zeta} - K_h N^2 + K_m S^2 - c_\varepsilon\frac{(\overline{e})^{3/2}}{\Lambda} \\ & + \frac{1}{a\cos\varphi}\frac{\partial}{\partial\lambda}\left(2K_m\frac{\partial\overline{e}}{a\cos\varphi\partial\lambda}\right) + \frac{1}{a}\frac{\partial}{\partial\varphi}\left(2K_m\frac{\partial\overline{e}}{a\partial\varphi}\right) \\ & + \frac{g\rho_0}{\sqrt{\gamma}}\frac{\partial}{\partial\zeta}\left(\frac{g\rho_0}{\sqrt{\gamma}}2K_m\frac{\partial\overline{e}}{\partial\zeta}\right),\end{aligned} \tag{73}$$

where

$$N^2 = \frac{g}{\Theta_v}\frac{\partial\Theta_v}{\partial z}, \tag{74}$$

and

$$\begin{aligned}S^2 = & \; 2\left[\left(\frac{\partial u}{a\cos\varphi\partial\lambda}\right)^2 + \left(\frac{\partial v}{a\partial\varphi}\right)^2 + \left(\frac{g\rho_0}{\sqrt{\gamma}}\frac{\partial w}{\partial\zeta}\right)^2\right] \\ & + \left(\frac{\partial u}{a\partial\varphi} + \frac{\partial v}{a\cos\varphi\partial\lambda}\right)^2 + \left(\frac{\partial w}{a\cos\varphi\partial\lambda} - \frac{g\rho_0}{\sqrt{\gamma}}\frac{\partial u}{\partial\zeta}\right)^2 \\ & + \left(\frac{\partial w}{a\partial\varphi} - \frac{g\rho_0}{\sqrt{\gamma}}\frac{\partial v}{\partial\zeta}\right)^2 .\end{aligned} \tag{75}$$

Next, the differencing in space and time must be carried out. This has to be made also by strict adaptation to the LM numerics. In detail, the C-grid in the horizontal and the Lorenz-grid in the vertical is mandatory to be used inclusively the appropriate differencing and averaging. Concerning the time difference scheme a 'mixed' scheme is applied: horizontal advection is approximated by a leap-frog scheme, for vertical advection plus vertical diffusion a partially implicit Crank-Nicholson scheme is applied, and horizontal diffusion as well as source/sink-terms like shear production, buoyant production/consumption, dissipation are treated by a time-forward scheme. In effect, by use of a Gaussian elimination algorithm a tridiagonal form for solving the slow-mode regime of the LLM will be found. The resulting $\overline{e}^{(n+1)}$ is then available to specify K_m and K_h. Here we skip the rather lengthy derivation of that tridiagonal form from the discretized TKE-equation. It may suffice to write down the relevant result. In order to support the following notation of differencing, averaging and the definition of the placement of variables on different gridpoints we refer to Figure 3.1 and Figure 3.2.

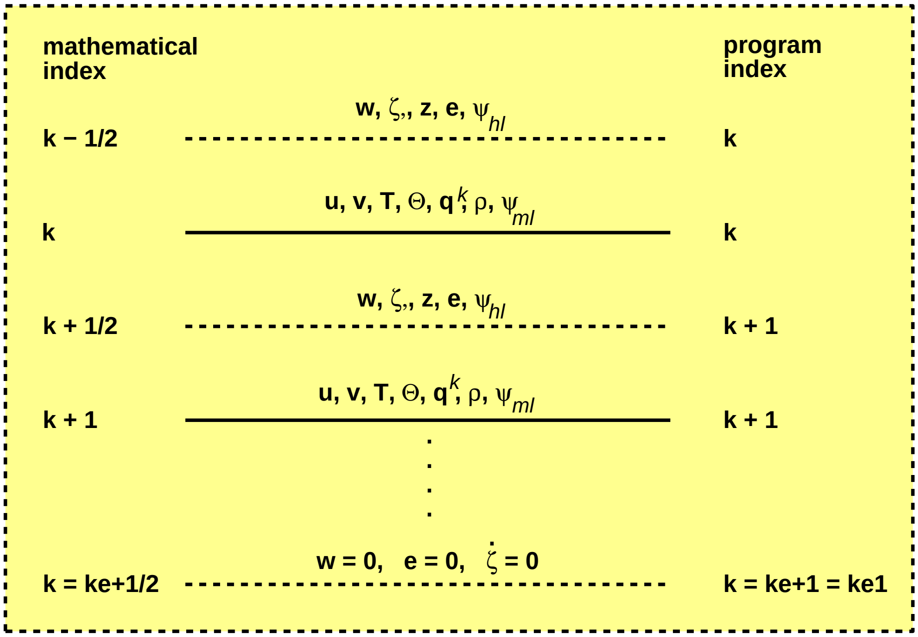

Figure 3.1: Vertical grid scheme (Lorenz-grid) with placement of variables at half-levels (dashed lines) and main levels (black lines). Further half-level variables (ψ_{hl}) and main-level variables (ψ_{ml}) are:
$\psi_{hl} = (\tau_{13}, \tau_{23}, h_3, F_3, K_m, K_h, S, N^2, Ri, \beta_v^{+,-}, \beta_d^{+,-})$,
$\psi_{ml} = (\tau_{11}, \tau_{12}, \tau_{22}, \tau_{33}, h_1, h_2, F_1, F_2, \sqrt{\gamma}, p_0, \rho_0)$.

The tridiagonal structural equation for determining $\overline{e}^{(n+1)}$, which is TKE at vertical half-level k (in accordance with program code indexing) and time level $n+1$, may be written

$$\begin{aligned} B_2\overline{e}_2^{(n+1)} + C_2\overline{e}_3^{(n+1)} &= D_2^{(n,n-1)} \\ A_k\overline{e}_{k-1}^{(n+1)} + B_k\overline{e}_k^{(n+1)} + C_k\overline{e}_{k+1}^{(n+1)} &= D_k^{(n,n-1)} \quad (k \in [3, ke-1]) \\ A_{ke}\overline{e}_{ke-1}^{(n+1)} + B_{ke}\overline{e}_{ke}^{(n+1)} &= D_{ke}^{(n,n-1)} \end{aligned} \tag{76}$$

The functions $D_k^{(n,n-1)}$ for $k \in [2, ke]$ in (76) are known. They contain only variables at the present and previous time level. The same is valid for the coefficients A_k, B_k, C_k. By use of the Gaussian elimination procedure the $\overline{e}_k^{(n+1)}$ follow by assuming the boundary condition $\overline{e}_1 = \overline{e}_{ke1} = 0$. For the coefficients A_k, B_k, C_k and D_k we find:

$$
\begin{aligned}
A_k &= \beta_v^+ A_k^v + \overline{\beta_d^+}^{\zeta} A_k^d \\
A_k^v &= -\frac{(\sqrt{\gamma})_k \overline{(W^c)}_{k-1}^{\zeta}}{\overline{(\sqrt{\gamma})}_k^{\zeta}\left((\sqrt{\gamma})_k + (\sqrt{\gamma})_{k-1}\right)}\,, \quad A_k^d = -\frac{2g^2\overline{(\rho_o)}_k^{\zeta}}{\overline{(\sqrt{\gamma})}_k^{\zeta}} \overline{\left(\frac{\overline{(\rho_o)}^{\zeta}}{\overline{(\sqrt{\gamma})}^{\zeta}} K_m^{(n)}\right)}_{k-1}^{\zeta} \\
B_k &= \frac{1}{2\Delta t} - A_k - C_k \\
C_k &= \beta_v^+ C_k^v + \overline{\beta_d^+}^{\zeta} C_k^d \qquad (77) \\
C_k^v &= \frac{(\sqrt{\gamma})_{k-1} \overline{(W^c)}_{k}^{\zeta}}{\overline{(\sqrt{\gamma})}_k^{\zeta}\left((\sqrt{\gamma})_k + (\sqrt{\gamma})_{k-1}\right)}\,, \quad C_k^d = -\frac{2g^2\overline{(\rho_o)}_k^{\zeta}}{\overline{(\sqrt{\gamma})}_k^{\zeta}} \overline{\left(\frac{\overline{(\rho_o)}^{\zeta}}{\overline{(\sqrt{\gamma})}^{\zeta}} K_m^{(n)}\right)}_{k}^{\zeta} \\
D_k &= \frac{1}{2\Delta t}\overline{e}_k^{(n-1)} + \Sigma_k^{(n,n-1)} + (\beta_v^- A_k^v + \overline{\beta_d^-}^{\zeta} A_k^d)(\overline{e}_k^{(n-1)} - \overline{e}_{k-1}^{(n-1)}) \\
&\qquad - (\beta_v^- C_k^v + \overline{\beta_d^-}^{\zeta} C_k^d)(\overline{e}_{k+1}^{(n-1)} - \overline{e}_k^{(n-1)})
\end{aligned}
$$

with the further definition

$$
W_k^c = \overline{(\sqrt{\gamma})}_k^{\zeta}\, \dot{\zeta}_k\,. \qquad (78)
$$

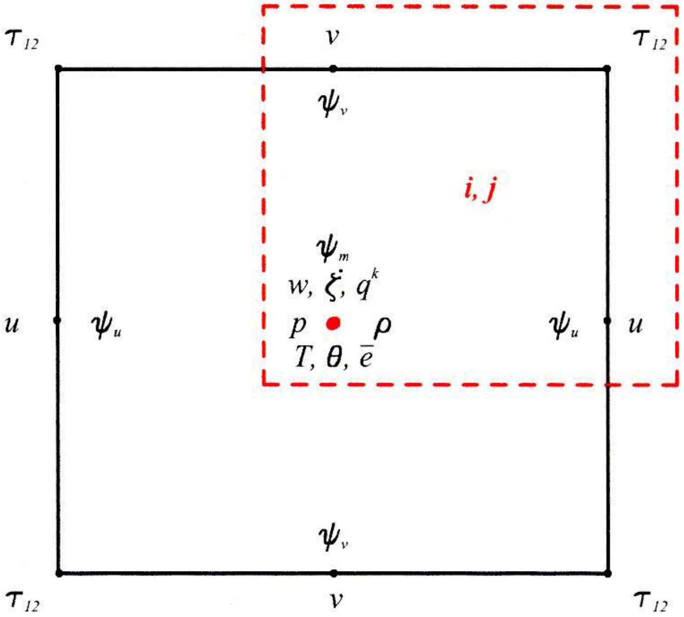

Figure 3.2: Position of variables in the horizontal grid (C-grid). Dashed-line square embraces a cluster of variables having the same horizontal program index pair i, j. Further variables at mass point (ψ_m), u-point (ψ_u) and v-point (ψ_v) are:
$\psi_m = (\tau_{11}, \tau_{22}, \tau_{33}, h_3, F_3, K_m, K_h, S, N^2, Ri, \sqrt{\gamma}, p_0, \rho_0)\,,$
$\psi_u = (\tau_{13}, h_1, F_1)\,, \quad \psi_v = (\tau_{23}, h_2, F_2)\,.$

The auxiliary variable $\Sigma_k^{(n,n-1)}$, emerging in the expression for D_k, implies horizontal advection and turbulent horizontal diffusion of TKE as well as source/sink-terms as follows:

$$
\begin{aligned}
\Sigma_k^{(n,n-1)} \; = \; & -\frac{1}{\overline{\sqrt{\gamma}}^{\zeta} a\cos\varphi}\left[\overline{\left(\overline{\overline{\sqrt{\gamma}}^{\zeta} u}^{\zeta}\; \delta_\lambda \overline{e}\right)}^{\lambda} + \overline{\left(\overline{\overline{\sqrt{\gamma}}^{\zeta} v}^{\zeta}\; \cos\varphi\, \delta_\varphi \overline{e}\right)}^{\varphi}\right] \\
& + \frac{1}{a\cos\varphi}\delta_\lambda\left(2(\overline{K_m}^{\lambda})^{(n)}\frac{\delta_\lambda(\overline{e})^{(n-1)}}{a\cos\varphi}\right) + \frac{1}{a}\delta_\varphi\left(2(\overline{K_m}^{\varphi})^{(n)}\frac{\delta_\varphi(\overline{e})^{(n-1)}}{a}\right) \\
& - K_h^{(n)}(N^2)^{(n-1)} + K_m^{(n)}(S^2)^{(n-1)} - c_\varepsilon\frac{((\overline{e})^{3/2})^{(n-1)}}{\Lambda}\,.
\end{aligned}
\tag{79}
$$

To complete the description of the tridiagonal form, we need finally the difference approximation of S^2 and Ri. For the deformation squared we have

$$
\begin{aligned}
S^2 \; = \; & 2\left[\left(\frac{\overline{\delta_\lambda u}^{\zeta}}{a\cos\varphi}\right)^2 + \left(\frac{\overline{\delta_\varphi v}^{\zeta}}{a}\right)^2 + \left(\frac{g\overline{\rho_0}^{\zeta}}{\overline{\sqrt{\gamma}}^{\zeta}}\delta_{2\zeta} w\right)^2\right] \\
& + \left(\frac{\delta_\varphi\overline{\overline{u}^{\lambda,\varphi}}^{\zeta}}{a} + \frac{\partial\overline{\overline{v}^{\lambda,\varphi}}^{\zeta}}{a\cos\varphi}\right)^2 + \left(\frac{\delta_\lambda\overline{w}^{\lambda}}{a\cos\varphi} - \frac{g\overline{\rho_0}^{\zeta}}{\overline{\sqrt{\gamma}}^{\zeta}}\delta_\zeta\overline{u}^{\lambda}\right)^2 \\
& + \left(\frac{\delta_\varphi\overline{w}^{\varphi}}{a} - \frac{g\overline{\rho_0}^{\zeta}}{\overline{\sqrt{\gamma}}^{\zeta}}\delta_\varphi\overline{v}^{\varphi}\right)^2
\end{aligned}
\tag{80}
$$

and the local Richardson number is written

$$
Ri \; = \; 2g\frac{(\Theta_{v,k} - \Theta_{v,k-1})\left(\sqrt{\gamma}_{k-1} + \sqrt{\gamma}_k\right)}{(z_{k+1} - z_{k-1})\left(\sqrt{\gamma}_{k-1}\Theta_{v,k} + \sqrt{\gamma}_k\Theta_{v,k-1}\right)\, S^2}
\tag{81}
$$

provided $S^2 > S^2_{min} > 0$. The equilibrium case (50) is used to determine an initial value of $\overline{e}_k$. A final remark is made concerning the incorporation of the turbulent surface fluxes. They are determined just as in the LM (cf. Doms and Schättler 1999, Chapter 6). A stability and roughness-length dependent formulation is used, which is based on modified Businger relations. As known, the approach makes use of a drag-law relation

$$
F^{\psi}_{sfc} \; = \; -\rho\, C^d_\psi\, |\vec{v}_h|\, (\psi - \psi_{sfc})
\tag{82}
$$

specified for $\psi = (u, v, T, q^k)$. The surface flux F^{ψ}_{sfc} follows then according to (82), provided the drag coefficient is given by a parameterization

$$
C^d_\psi \; = \; \frac{\chi^2}{[\ln(h/z_0)]^2}\, f_\psi(Ri_B, h/z_0)
\tag{83}
$$

dependent on the bulk Richardson number

$$
Ri_B \; = \; g\frac{(\Theta - \Theta_{sfc})\,(h - z_0)}{\Theta_{sfc}(u^2 + v^2)}
\tag{84}
$$

as a measure of stability. With given surface values ψ_{sfc}, Θ_{sfc}, provided from the soil model 'terra', the surface flux will be determined using atmospheric values ψ, Θ and $|\vec{v}_h|$ at the

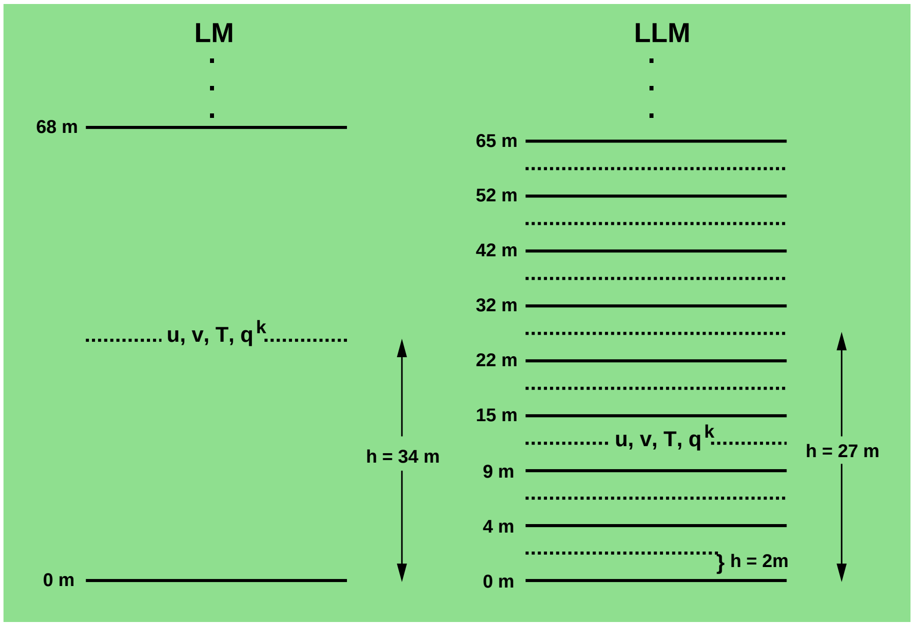

Figure 3.3: Different vertical resolution of the Prandtl-layer in LM (left) and in LLM (right). Further explanation see text.

model altitude h within the Prandtl-layer. In case of the LM this altitude is assumed to be placed at the lowest main-level being $h = 34$ m (Fig 3.3, left). By direct use of that LM-algorithm in case of the LLM the height h would also be positioned at the lowest model main-level, which is only about 2 meters above ground. In order to avoid a value of h too near to the roughness-length z_0, it has been set sufficiently higher than z_0 (Fig 3.3, right). Consequently, some more involved manipulations in the given LM-numerics not mentioned in detail were necessary to be done for that kind of LLM adaptation.

4 External Forcing at the Lateral and Upper Boundary

Since the LLM is thought to be a 'real-world' - LES model with its declared bridge-function in the scope of an observation-simulation conception, it must externally be driven somehow by real-world time-dependent states of the boundary layer atmosphere and the underlying surface. The initial state must also be a realistic one to start the LLM simulation from. While the physical forcing from the underlying surface will be treated in the following Chapter 5, we are dealing here with the atmospheric part of forcing the LLM.

4.1 Method

Before we describe some technical details, how lateral and upper boundary data, and initial data as well, are organized by use of time sequences of measured vertical profiles available, some general remarks about the strategy of an external LLM-driving are necessary. In contrast to 'pure' LES studies the LLM simulations have been planned to cover a wide range of real meteorological weather situations. This needs a more general approach not limited to special cases. This statement does not deny the general virtue of large eddy simulations which by fortunate circumstances can investigate general problems from simplified modelling, e.g. by ignoring the lateral limitation of the integration area. In our case a limited area integration mode must be accepted, and the technique to handle that problem had to be borrowed from the field of NWP. The method of interest has been described in Section 2.3. As explained there, the boundary technique is chosen in such a way that it anticipates the specific problem of application. From the point of view of information content of measured data we meet with a very underestimated problem for providing the LLM with initial and boundary data. In Fig. 4.1 the following argumentation is to be supported. In that manner we are forced to assume only one measured vertical profile for each relevant LLM variable like horizontal wind, temperature and moisture.

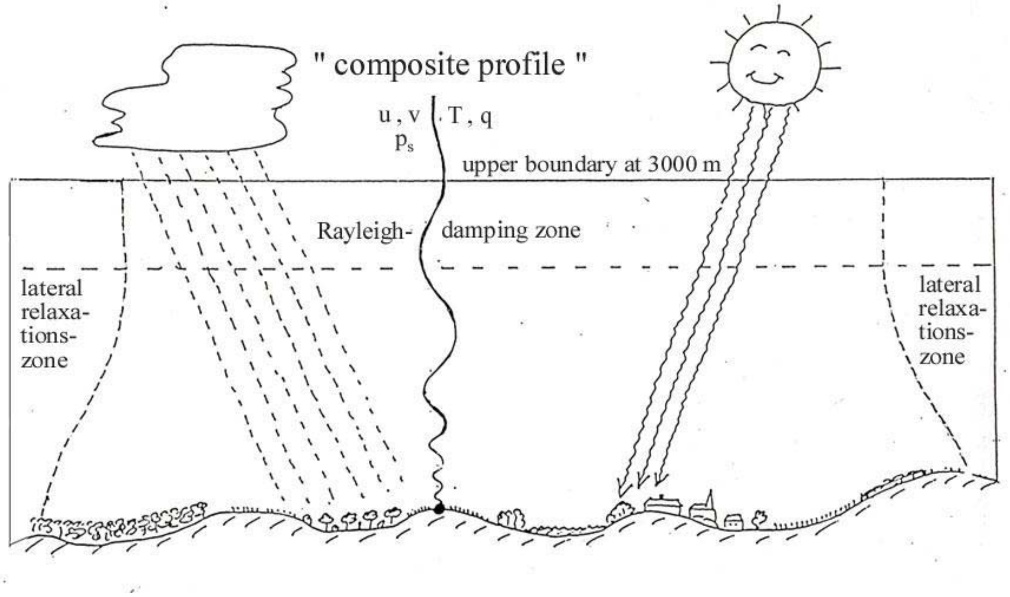

Figure 4.1: A sketch showing how the LLM is externally driven by taking into account a detailed physiographic description of the underlying surface plus surface measurements of precipitation and radiation and by use of a driving composite profile which operates through a vertical and lateral transmission zone.

We call it a 'composite profile' (CP), because it is deduced from vertical profiles of different sounding systems available at and around the MOL (Görsdorf et al. 2000), and it may be available at a time frequency of say, one hour. This CP is assumed to be associated to a distinct location laying in the interior of the LLM integration area. Further, the CP gives the only base of temporally and vertically distributed information for constructing the three-dimensional initial and boundary data due to a quasi-horizontal distribution of that given vertical profiles. How this is carried out will be shown in the next section.

Here some arguments to support this approach will be given. By horizontally distributing the CP we make use of the 'hypothesis of fast local adaptation', provided that the physical forcing from the underlying surface works well (cf. Sections 2.4, 2.5, Chapter 5 and Fig. 4.1). Therefore, the near-surface information of a CP is unsuitable at other places than the original location which is assumed to be assimilated by the LLM very fast and in case of boundary data in a rather short distance from the boundary. The mechanism of dominating near-surface turbulent fluxes, essentially coined by carefully treated lower boundary properties, makes thus the CP-data model-friendly and brings them automatically into a 'ready-to-eat' form. From the point of view of the lateral boundary technique this kind of near-surface adaptation is deliberately supported by reduced boundary weights. Towards higher levels of the LLM the CP information approaches to larger scales and even to scales governing the free atmosphere up to 3 kilometers. Because the essential integration mode of the LLM is given by a non-stationary boundary data forcing, the time-dependent boundary data rely on time series of CPs with an up-dating frequency of 1 hour with a linear time interpolation onto every 2-second timestep.

It is important to note that by use of that CP sequence the LLM perceives relevant large-scale information in an implicit way. That is, changes of the temperature profile imply realistic effects of large scale warm/cold air advection, changes of stability indicating large-

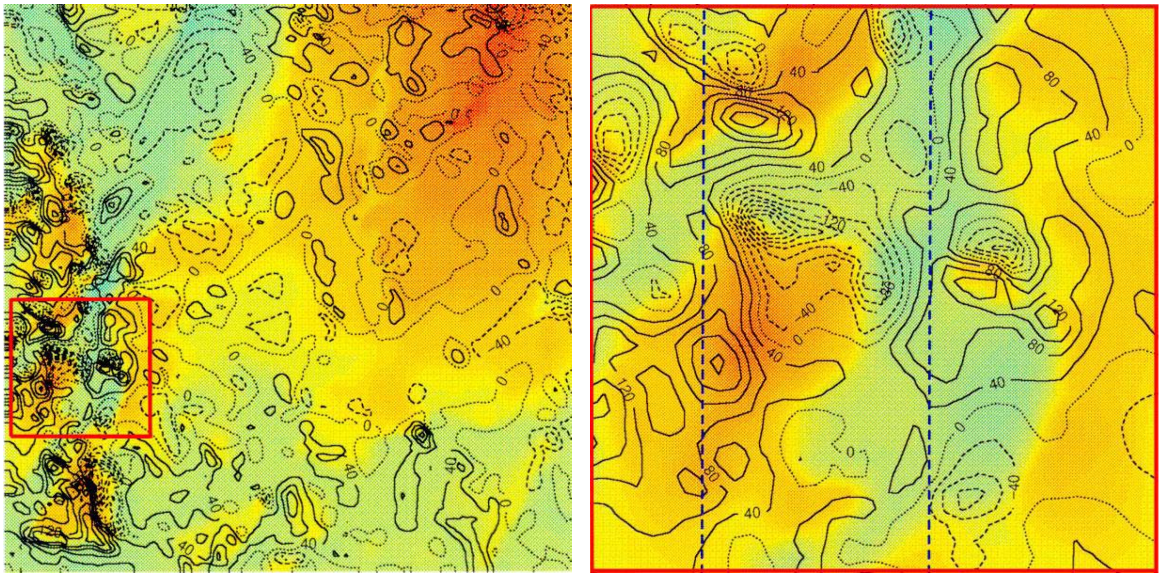

Figure 4.2a: Results from a 24-h integration after 12 hours, on 14 June 1997 at noon, for vertical motion w. Left: in a horizontal section over the whole 145 × 145 gridpoint area at a model level about 100 m above ground. Right: enlargement for the red-marked 3.5 × 3.5 km^2 sub-area, where the vertical velocity varies in an interval -310 mm/s $\leq w \leq$ 277 mm/s. Cross sections along the two dashed lines are shown in Fig. 4.2b.

scale divergence and so subsidence, and also effects of radiative warming/cooling. From each profile an estimate of the geostrophic wind and so the large-scale pressure gradient is derived for determining the pressure field of the initial and boundary data.

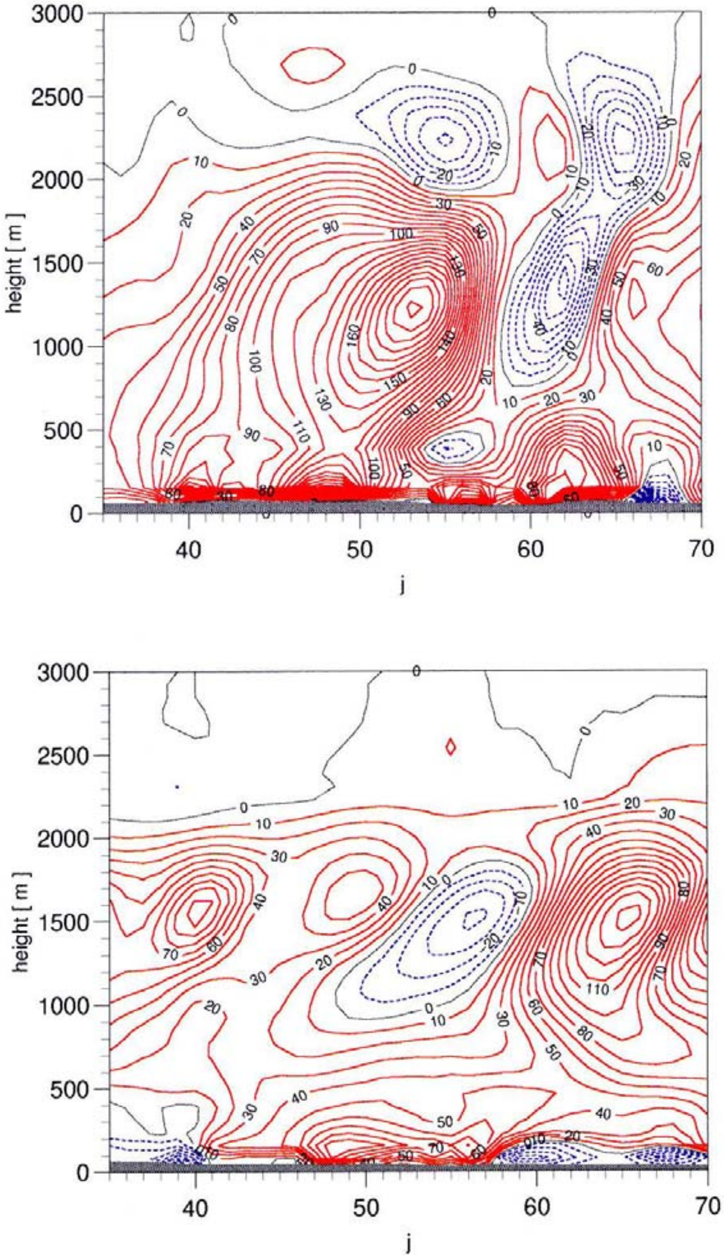

Figure 4.2b: South-north vertical cross sections of vertical velocity (isolines in mm/s, negative values dashed) along the two dashed lines in Fig 4.a. Top: Cross section referring to the left dashed line in Fig. 4.2a. Bottom: Cross section referring to the right dashed line in Fig.4.2a.

Concerning the ability of local adaptation even in the very proximity of the lateral boundary, an example is shown in Figs. 4.2a and 4.2b, where the fine-scale structures are obviously established against the external influence of the boundary data derived from CP's. The example of a 24-hour simulation has been carried out on 14 June 1997. The vertical motion is shown in a horizontal section covering the whole area of 145 × 145 gridpoints, after a 12-

hour integration time, at noon (Fig. 4.2a, left). By zooming over an indicated 3.5×3.5 km^2 sub-area (Fig. 4.2a, right) and by further inspection from two selected south-north-vertical cross sections coherent w-structures related to local orographic structures are observed (Fig. 4.2b). With that case a rather involved synoptic situation has been chosen by chance. The basic current at noon was directed from WSW.

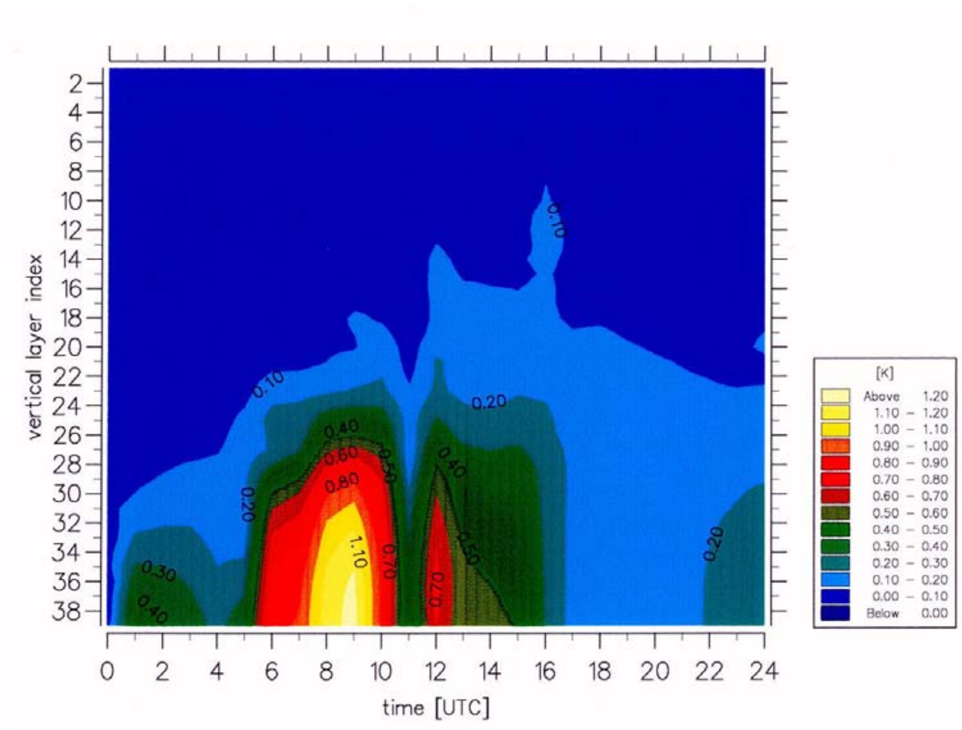

Figure 4.3: The standard deviation of temperature as a function of height and time for the LITFASS day 1 June 1998.

For another 'non-textbook case' (1 June 1998, arbitrarily selected from the LITFASS '98 period) the standard deviation of temperature deduced from the standard LLM integration domain with its variation in time and along the vertical is shown in Fig. 4.3. It demonstrates here in a more qualitative manner the local forcing by the inhomogeneities of the underlying surface: Though the standard deviation is not too large for such a case in June, it shows a rather changable variation over the day with convective intervals in the morning and significant rainfall in the late afternoon and evening.

4.2 Technical Approach

Assuming given vertical profiles of horizontal wind, temperature and moisture as a Composite Profile (CP) constructed from different measurement systems at MOL (Görsdorf et al. 2000, Beyrich 2000) and from the Falkenberg measurement site ('Gemeinsames Messfeld' = GM), the specific task is to determine the initial field and the boundary data fields from that information by use of a reasonable extrapolation approach with the above mentioned philosophy behind. As a matter of fact, those profiles are from technical reasons hourly available, which defines the updating frequency of boundary data for the LLM. By an agreement the CP provides u^M, v^M, T^M and the specific humidity q^M at all LLM-main levels along a vertical gridpoint column (the superscript M denotes a measured value). The surface pressure p_s^M is also assumed to be known.

The location of this vertical profile is given at the horizontal gridpoint i=118, j=67 with respect to the LLM standard grid net (cf. Section 2.6). As a first step, the variables u^M, v^M, T^M are horizontally distributed on (terrain-following) model levels. Due to a lack of more information this procedure has to be tolerated having in mind that the orography in the LLM area is formed by a gently undulating earth surface with surface heights in between about 40 and 120 meters above sea level. Above 1000 meters the model levels are genuinely horizontal (cf. Section 2.2). In mountainous regions this method seems insufficient. Here, the surface pressure field p_s is calculated on the base of p_s^M using T_{ke}^v and the given orographic height values z_s:

$$p_s = p_s^M \exp\left[-\frac{g(z_s - z_s^M)}{RT_{ke}^v}\right] . \tag{86}$$

T_{ke}^v is the virtual temperature at the lowest main level ($ke = 39$). In a further step the large-scale pressure gradient is determined from averaging the five uppermost wind values of the CP which are assumed to be representative for the free atmosphere. From this gradient assuming barotropy a pressure correction is added to the ps-field. In the following step the perturbation pressure field $p'_{ke} = p - p_0(z)$ is calculated for each vertical gridpoint column using p_s and a first guess value of virtual temperature T_{ke}^v. For the present we obtain

$$p'_{ke} = p_s \exp\left[-\frac{g(z_{ke} - z_s)}{RT_{ke}^v}\right] - p_{0,ke} . \tag{87}$$

Next, the p'_{ke} for $k < ke$ can be determined upwards by a recurrent formula following from the hydrostatic equation, which is here the LM-consistent differencing analogue of a balance equation with the first three terms on the r.h.s. of equation (3) (these are vertical pressure gradient -, buoyant- and water loading term). A more detailed description of that hydrostatic approach with an iterative improvement of T^v is given in Doms and Schättler (1999).

Normally, the given CP information consists of a synthesis of measured data from radiosonde, wind profiler, RASS, microwave profiler and 100m-mast. In a program module src_obsdata.f90 that CP estimate is used to construct both the initial field and the hourly boundary data fields as described above. As an important generalization the latest completion in this program module is the possibility to use a pseudo-CP having data exclusively from an LM-profile over the central gridpoint (i,j) = (73,73). In parallel to genuine CP-driven runs some selected 24h-runs with LM-profile forcing from the LITFASS '98 episode have been successfully carried out (cf. Chapter 6). The option of an LM-profile forcing is seen to be a necessary step for integrating the LLM off from Lindenberg over a transportable area imbedded in the LM integration domain. Moreover, that kind of forcing is of interest for a broader LM validation by use of the LLM as the declared validation tool.

In view of the following Chapter 5, where the physical forcing from the surface is dealt with, we add some further functions of the mentioned module src_obsdata.f90 providing the LLM with inhomogeneous fields of soil parameters. These are: land/water fraction per gridbox and soil typ as time-fixed values; all other parameters are in principle temporally variabel due to the annual vegetation cycle: orographic plus displacement height, roughness length, root depth, leaf-area index, degree of plant covering. Finally, two-dimensional fields of the water content of the upper (0-10cm) and medium (10-100cm) soil layer of the soil model 'terra', following from a homogeneous distribution of measured values or a longer series of precursory LLM runs with the desired effect of an inhomogeneous soil moisture spin-up, are read for starting the actual run. All these values have to be distributed among all computing processors.

5 Physical Forcing at the Lower Boundary

As already outlined, the most important forcing of the LLM is caused from the underlying surface with its natural inhomogeneities. In contrast to the lateral and upper boundary, the lower one is a physical interface, where the exchange of energy and water between atmosphere and soil takes place. These processes are characterized by the presence of turbulent near-surface fluxes of momentum, heat and moisture. In a complex way these fluxes depend strongly on physical conditions as e.g. local soil properties, soil moisture, radiation received at the surface, specific land use and realistic orography. In order to have a local forcing from below as exact as possible in the sense of 'real-world' - simulations with the LLM, the careful treatment of the mentioned physical properties is found to be a main task of the LLM development.

In that way, the detailed physiographic description of the underlying surface consists in deriving external parameters which are the key parameters of the coupled soil model to describe the dominating processes of soil, surface and vegetation with them. These parameters will be described in Section 5.1. To determine the relevant energetic processes at the bounding surface, it is important to know the short- and long-wave radiation balance there as well as the precipitation flux reaching the earth surface. These fields are derived from all the surface radiation and precipitation measurements available over the Lindenberg area. This is shown in detail in the following Sections 5.2 and 5.3. Since realistic LLM simulations are strongly dependent on a proper soil moisture distribution in connection with the given soil model, but soil moisture measurements are extremely sparse, an empirical adaptation method by using the LLM system itself is carried out and described in Section 5.4.

5.1 External Parameters

The kind and number of external parameters depend on the soil model in the LLM. Apart from minor changes, the soil model, which is the program module 'terra', is identically taken from the LM. In order to determine the appropriate external parameters over the high-resolving LLM grid, a comprehensive physiographic data set has been made available. It consists of orography data, of actualized airborne land use information (Zimmermann 1994a, b) and of soil property data (Hierold et al., 1997). All these data were provided in a vectorized form and had been transformed to LLM gridpoint data by Rosenow (1998).

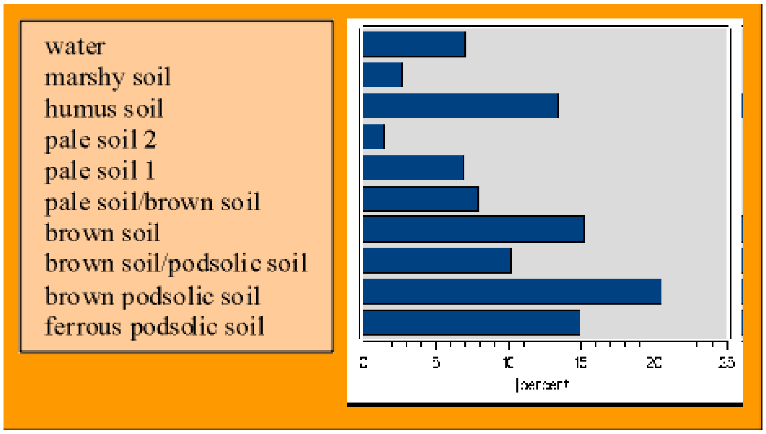

Figure 5.1: Soil type cover in percent of the total LLM area.

In the following a short description is given how the external parameters of interest are deduced from these data. According to a given soil map having 27 different soil types in the LLM simulation area, these types had to be reduced and fitted to only 9 types distinguished in the soil model. Fig 5.1 shows a histogram with the coverage of relevant soil types in percent of the total area of 199 × 199 gridpoints (see Section 2.6). The most frequent soils are brown-podsolic soil (20.5%), brown soil (15.2%) and ferrous podsolic soil (14.9%), while the coverage of water amounts to 7%.

In Fig. 5.2 the areal distribution of soil types is shown indicating the predominance of brown soils in the eastern part, whereas ferrous podsolic soils are found in the west. At some locations in the southern part and also in the proximity of lakes marshy soils sometimes prevail.

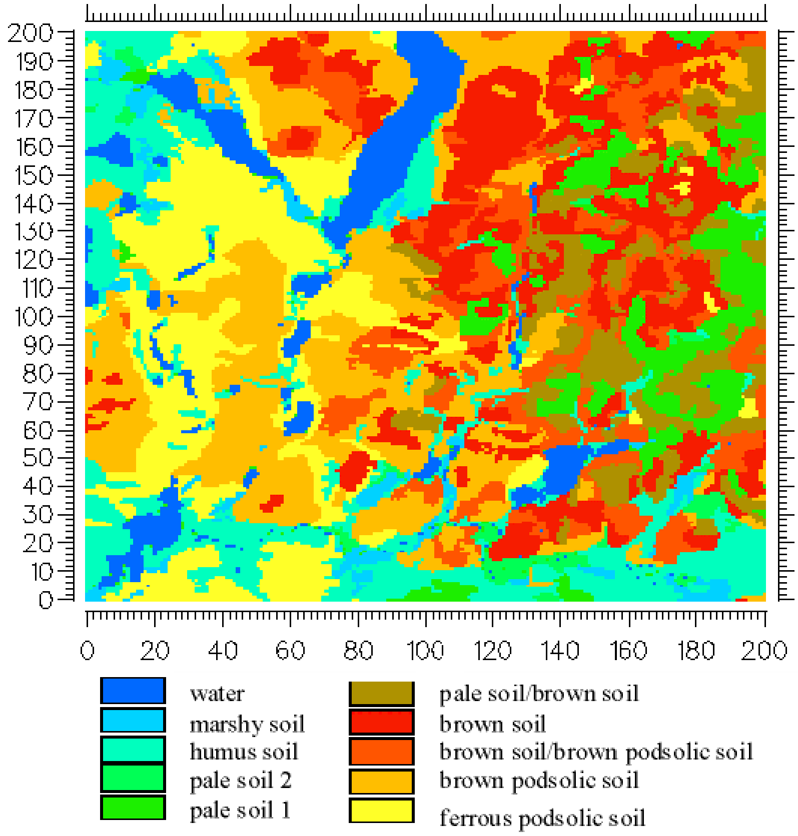

Figure 5.2: Distribution of soil types over the LLM area.

In the following Fig 5.3 topographic information is compiled showing e.g. the placement of important settlements, roads and lakes, and indicating specific locations associated to horizontal gridpoint indices. To add still more information, Tab. 5.1 provides a list of local soil parameters as valid in 'terra'. These parameters are additionally put in relation to processes like water storage, vertical water transfer within the soil, transpiration of plants and radiation near the surface. In order to demonstrate the horizontal heterogeneity of soil parameters, in Figs. 5.4 and 5.5 are shown the patterns of field capacity (a measure of maximal ability to store water in a soil layer) and soil heat capacity, respectively. Comparing both fields, it can be seen that podsolic soils in the west are able to store somewhat more of water and have a larger thermal inertia than brown soils in the eastern part. In contrast, marshy soils indicate a relatively high field capacity, but a relatively low soil heat capacity.

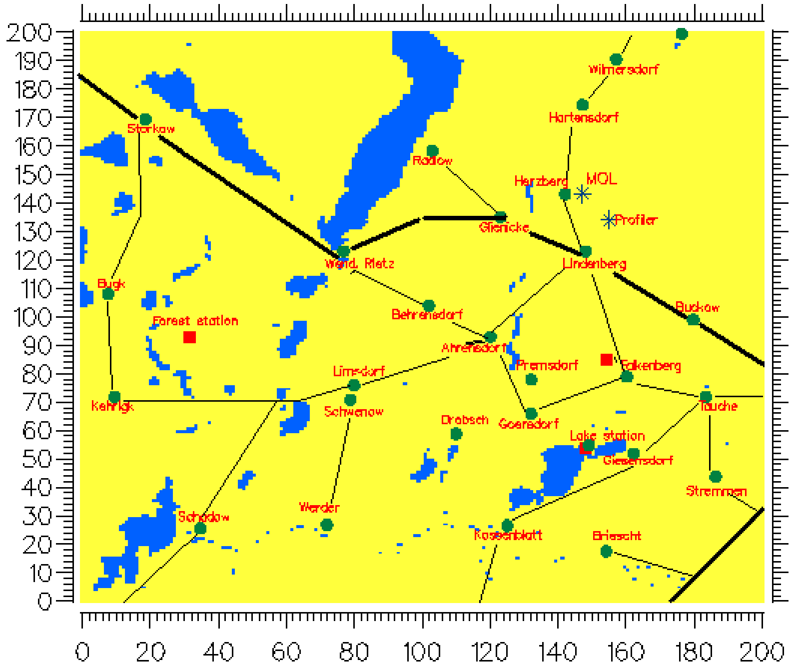

Figure 5.3: Map of local topographic information.

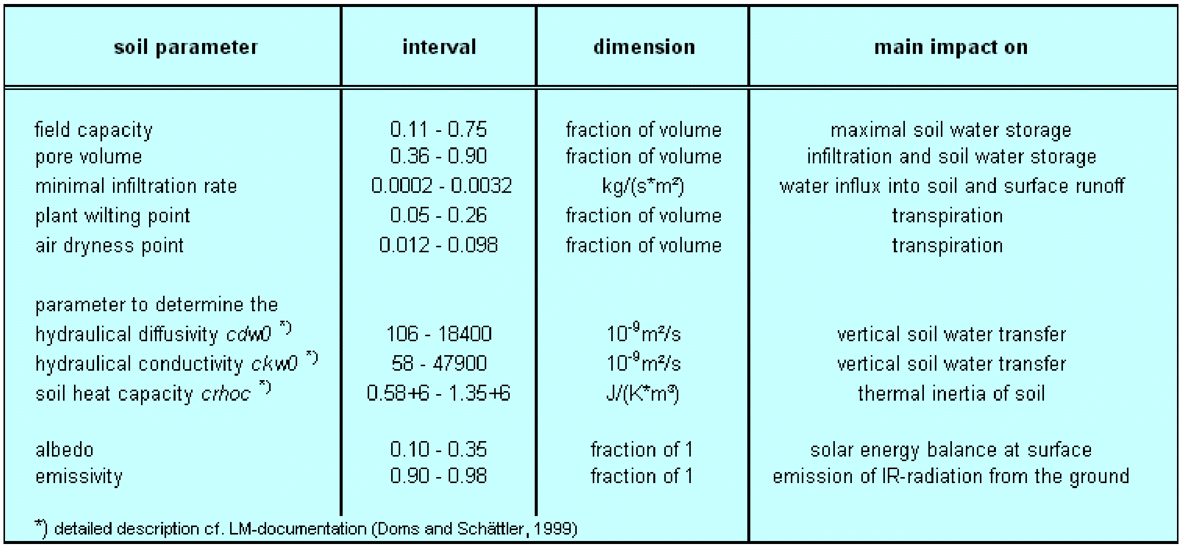

soil parameter	interval	dimension	main impact on
field capacity	0.11 - 0.75	fraction of volume	maximal soil water storage
pore volume	0.36 - 0.90	fraction of volume	infiltration and soil water storage
minimal infiltration rate	0.0002 - 0.0032	kg/(s*m^2)	water influx into soil and surface runoff
plant wilting point	0.05 - 0.26	fraction of volume	transpiration
air dryness point	0.012 - 0.098	fraction of volume	transpiration
parameter to determine the			
hydraulical diffusivity *cdw0* *)	106 - 18400	10^{-9}m^2/s	vertical soil water transfer
hydraulical conductivity *ckw0* *)	58 - 47900	10^{-9}m^2/s	vertical soil water transfer
soil heat capacity *crhoc* *)	0.58+6 - 1.35+6	J/(K*m^3)	thermal inertia of soil
albedo	0.10 - 0.35	fraction of 1	solar energy balance at surface
emissivity	0.90 - 0.98	fraction of 1	emission of IR-radiation from the ground
*) detailed description cf. LM-documentation (Doms and Schättler, 1999)			

Table 5.1: Local soil parameters used in LLM.

Another sort of external parameters concerning the simulation of effects related to the coupled surface-vegetation system must be derived from the given land use data. The original data set comprises 35 biotopes resolving details smaller than the LLM grid mesh distance of about 100m. In view of the limited vegetation parameterization model the number of biotopes had to be reduced to 13 main types with water included. The resulting parameters distinguish between vegetation with constant height and a monthly varying leaf area index (e.g. forest, grass- and greenland as well as fen) and those having even daily variations (agricultural plants).

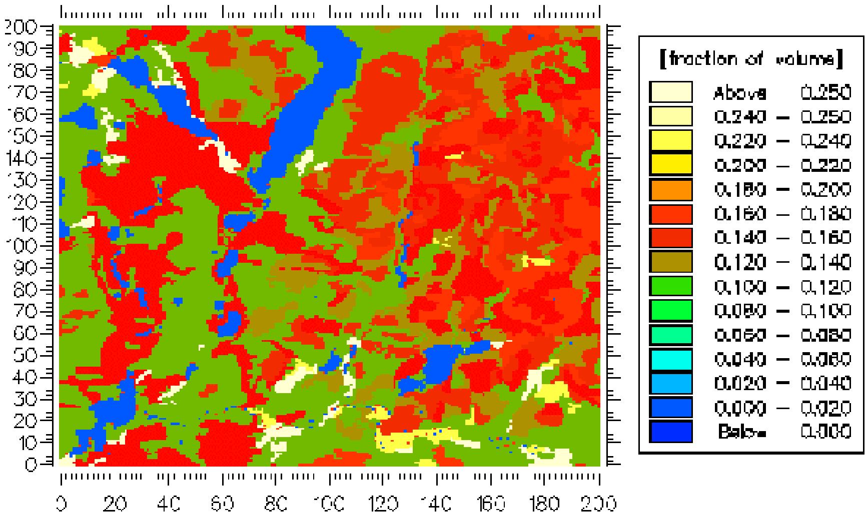

Figure 5.4: Field capacity distribution of the relevant soil types.

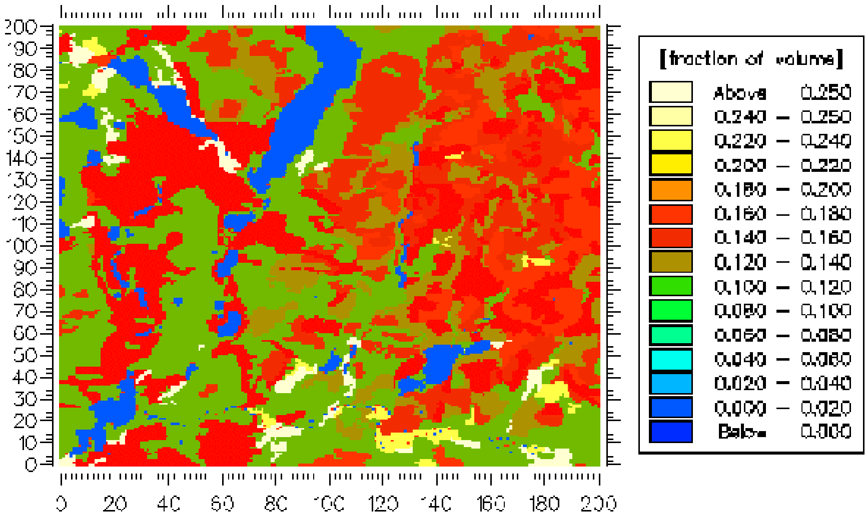

Figure 5.5: Distriubution of soil heat capacity.

As can be seen in Tab. 5.2 the predominant land use pattern is significantly influenced by human activity. The result is a high amount of coniferous forest (40.5%) and farmland (27.5%), while forest of deciduous trees has a portion of 8%. Greenland (here defined as fallow land, covered by several uncultured plants differing from forest) covers 14.5% of the total area.

Forests and fields are unequally distributed over the whole integration domain. According to the land use map shown in Fig. 5.6, forest prevails in the south-west while farmland dominates in the north-eastern part of the region. The most important agricultural plants are triticale, maize and rape. The variety seen in the actual land use map of June 1998 is largely determined from the different sorts of agricultural plants growing in that season. This concerns our simulation period for the LITFASS-98 experiment. In order to adapt the associated parameter distribution to the LINEX-2000 experiment (August-September 2000), the agricultural areas are assumed to be covered by grass after the harvest. That amounts to be an area portion of 28.6% for grassland compared to only 1.1% during June 1998.

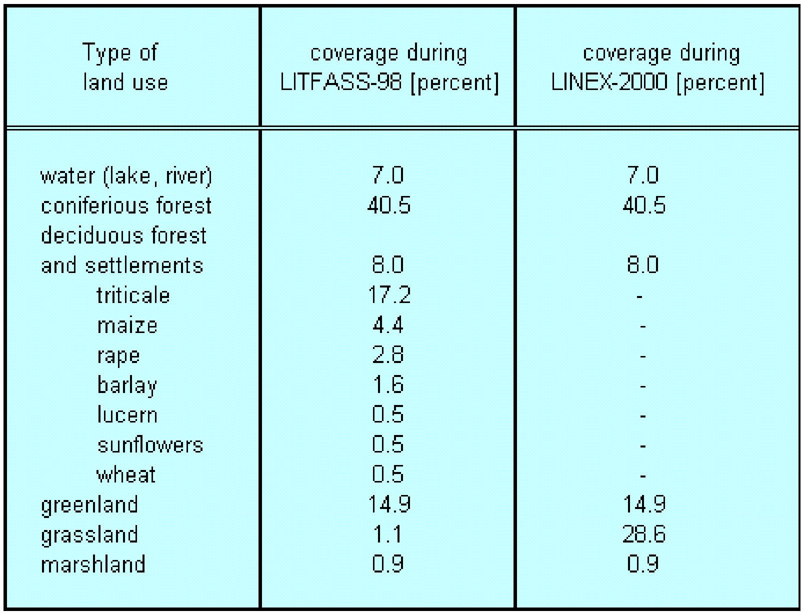

Type of land use	coverage during LITFASS-98 [percent]	coverage during LINEX-2000 [percent]
water (lake, river)	7.0	7.0
coniferious forest	40.5	40.5
deciduous forest and settlements	8.0	8.0
triticale	17.2	-
maize	4.4	-
rape	2.8	-
barlay	1.6	-
lucern	0.5	-
sunflowers	0.5	-
wheat	0.5	-
greenland	14.9	14.9
grassland	1.1	28.6
marshland	0.9	0.9

Table 5.2: Land use cover in percent for the campaigns LITFASS-98 and LINEX-2000.

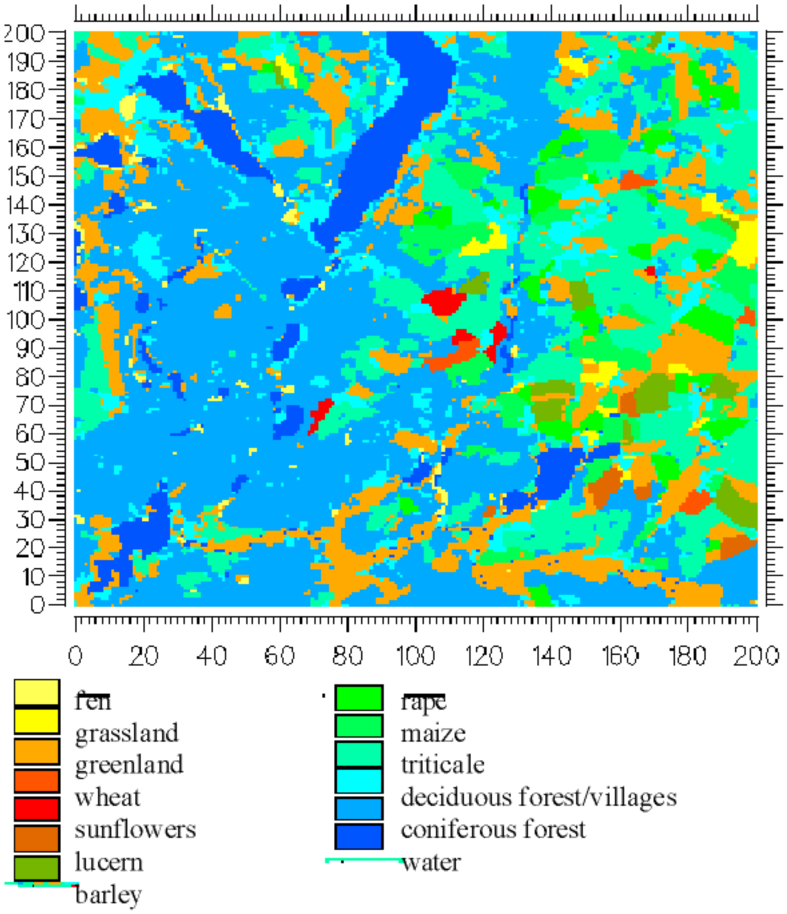

Figure 5.6: Land use cover (see text).

The external parameter set required for the LLM simulations is eventually listed in Tab. 5.3. In addition, the relevant land-surface processes playing a major role in driving the LLM from below are noted in that table.

Among all parameter maps, the landpoint mask can be obtained immediately from the map of soil types indicating where areas of water are located. Considering the fine grid resolution, it suffices to entirely assume a grid point to be either water or land. Concerning the specification of the root depth parameter, it is necessary to accept facts given by the present soil model. With respect to the hydrological part this model is assumed to have two active vertical layers, from 0 - 10 cm and 10 cm - 1 m depth. Therefore, in case of forest and greenland a constant root depth of 0.5 m has been chosen, while the root depth of farm- and grassland as well as fen is taken 0.05 m.

Some more effort is needed to determine the other external parameters mentioned in Tab. 5.3, since they depend explicitly on the type of vegetation. For the sake of convenience they have been estimated separately for vegetation and bare soil, before the final fields are determined by averaging both components with weights of the given degree of plant covering. This approach seems to be valid for the surface roughness length and the displacement height.

external parameter	**interval**	**dimension**	**main impact on**
landpoint mask	0 or 1		distribution of land and water gridpoints
roughness length	0.0002 - 1.52	m	vertical wind profile
displacement length	0 - 12	m	vertical wind profile
leaf area index	0 - 8	m^3/m^3	transpiration of plants
fractional plant cover	0 - 0.99	fraction	vegetation and bare soil components of the external parameters
root depth	0.05 or 0.50	m	transpiration of plants
albedo	0.10 - 0.35	fraction	solar energy balance at surface
emissivity	0.90 - 0.98	fraction	emission of IR-radiation from the ground

Table 5.3: Local external parameters used in the soil/vegetation module of LLM.

land use type	**vegetation height [m]**	**LAI-variation in the annual course**
coniferious forest	~15	8.0
deciduous forest	10	0.1 - 8.0
grassland	0.15	0.2 - 1.4
greenland	4	0.1 - 4.0
marshland	1	0.1 - 4.0

Table 5.4: Vegetation heights and LAI-values for some land use types.

In case of vegetation these values depend on the actual height of plants and the leaf area index. For some sorts of vegetation it is sufficient to use fixed plant heights, which are given in Tab. 5.4. Based on observational data from Lindenberg area a forest of coniferous trees is, on average, assumed to have a height of 15 m with a random variation superimposed within an intervall of ± 5 m. Only in case of agricultural plants the vegetation height is assumed time-variable.

For agricultural plants the time-variation of the plant height h_v and the LAI is considered over the vegetation period until the harvest using simple formulae proposed by Vogelgesang (1993) and Jürrens, respectively. For both parameters $\psi = (h_v, LAI)$ a linear time-interpolation formula is applied, where n counts the Julian days during the annual course:

$$\psi = \begin{cases} \psi_s & , n \le n_s \\ \psi_s + \frac{\psi_z - \psi_s}{n_z - n_s}(n - n_s) & , n_z < n \le n_s \\ \psi_s + \frac{\psi_{max} - \psi_z}{n_{max} - n_z}(n - n_z) & , n_{max} < n \le n_e \\ \psi_s & , n_e < n \end{cases} \tag{88}$$

$\psi_s, \psi_z, \psi_{max}$ denote the values of parameters at selected Julian days n_s, n_z and n_{max}, where n_s is a Julian day at the very beginning after the seed-time, n_z marks a day characterizing a particular change of the plant property in order to ameliorate the linear approach due to a nonlinear growth in reality, and n_{max} denotes a day when the plant has obtained its maximal height, n_e is the day of the harvest.

Thus, both key parameters indicate the progress of plant growth and the degree of maturity (cf. Tab's. 5.5 and 5.6). In Fig. 5.7 the time-variation of the plant height as used in the LLM is shown in comparison to some measured heights (triangles), where these measurements are used to derive the parameters in (88). In view of these curves the model-relevant time of the LITFASS-98 experiment (1-20 June 1998) can be characterized by the end of a rapid growth, with exception of maize. Most of plants have obtained their maturity stage. In the following Fig. 5.8 a time-averaged field of LAI over the same LITFASS-98 period is depicted illustrating the typical physiographic structure of the Lindenberg simulation area. High LAI-values of about 8 are found in the south-west, while values of about 2 - 4 can be found in the eastern part of the area. The minimum value is found to be not below 0.7.

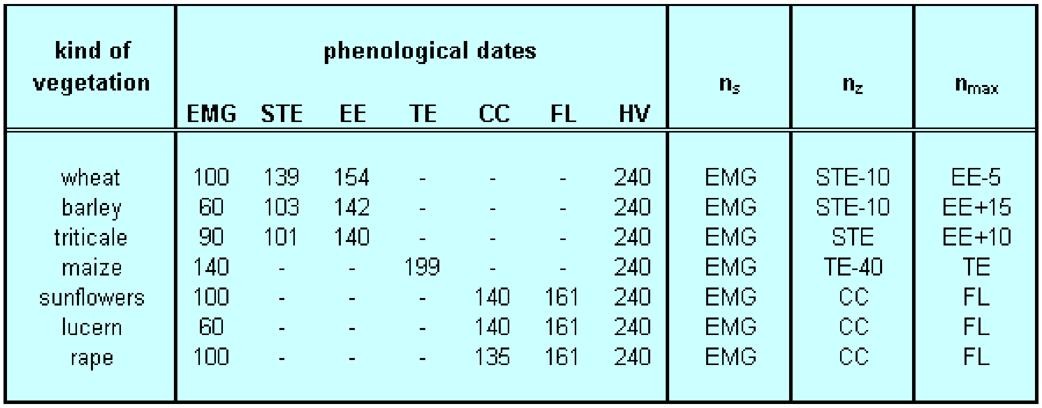

kind of vegetation	phenological dates							n_s	n_z	n_{max}
	EMG	STE	EE	TE	CC	FL	HV			
wheat	100	139	154	-	-	-	240	EMG	STE-10	EE-5
barley	60	103	142	-	-	-	240	EMG	STE-10	EE+15
triticale	90	101	140	-	-	-	240	EMG	STE	EE+10
maize	140	-	-	199	-	-	240	EMG	TE-40	TE
sunflowers	100	-	-	-	140	161	240	EMG	CC	FL
lucern	60	-	-	-	140	161	240	EMG	CC	FL
rape	100	-	-	-	135	161	240	EMG	CC	FL

Table 5.5: Dates (in Julian days) of phenological events and characteristic plant heights after Löpmeier (1983), Jürrens (1996) and own studies (see text). EMG: emergence; STE: stem elongation; EE: ear emergence, heading; TE: tessel emergence, heading; CC: canopy closed, crop cover complete; FL flowering; HR: harvest.

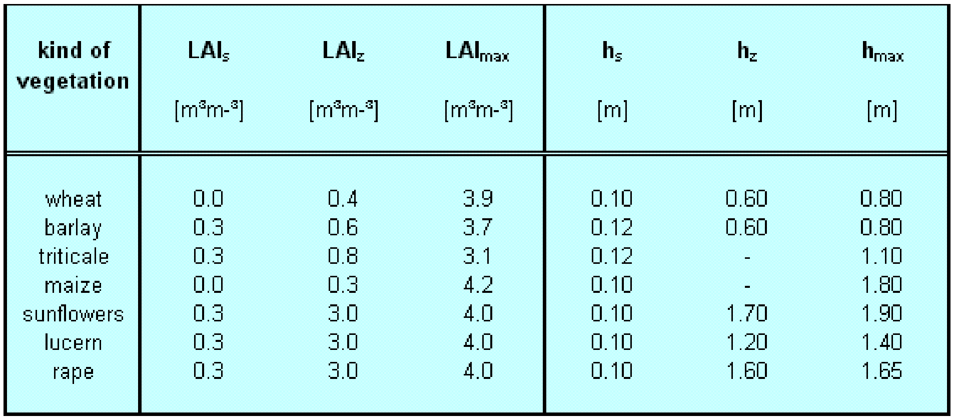

kind of vegetation	LAI_s $[m^3m^{-3}]$	LAI_z $[m^3m^{-3}]$	LAI_{max} $[m^3m^{-3}]$	h_s [m]	h_z [m]	h_{max} [m]
wheat	0.0	0.4	3.9	0.10	0.60	0.80
barlay	0.3	0.6	3.7	0.12	0.60	0.80
triticale	0.3	0.8	3.1	0.12	-	1.10
maize	0.0	0.3	4.2	0.10	-	1.80
sunflowers	0.3	3.0	4.0	0.10	1.70	1.90
lucern	0.3	3.0	4.0	0.10	1.20	1.40
rape	0.3	3.0	4.0	0.10	1.60	1.65

Table 5.6: LAI-values and typical vegetation heights.

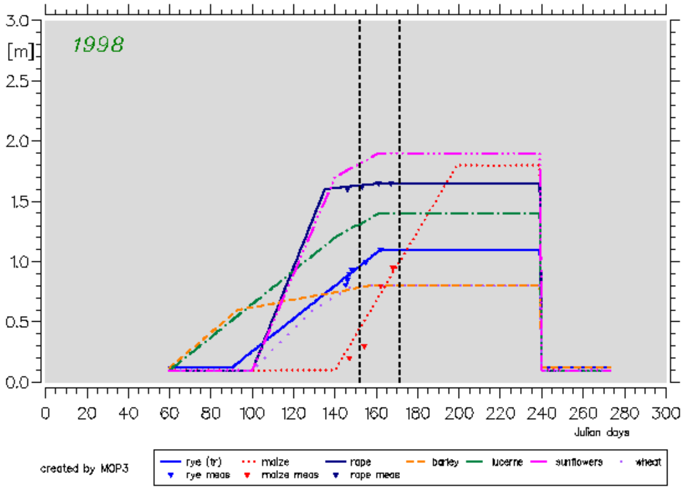

Figure 5.7: Time-variation of the plant height (see text).

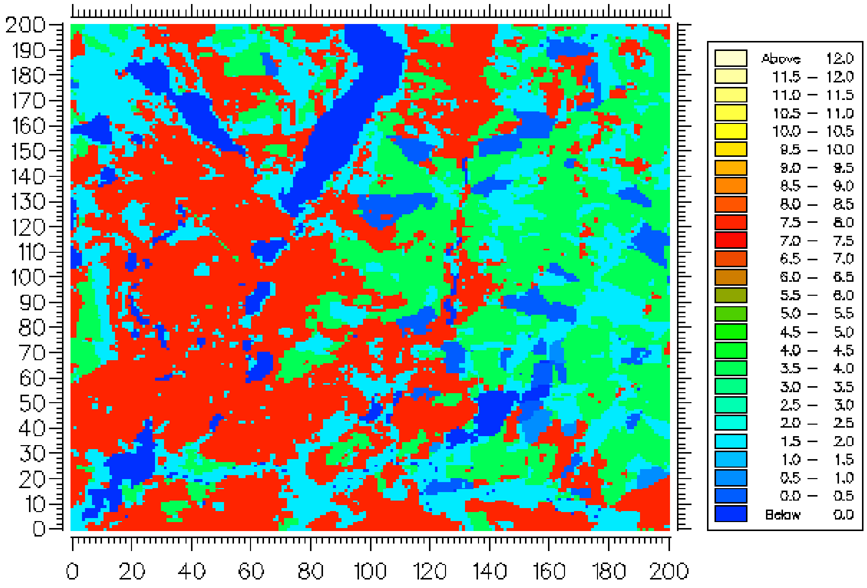

Figure 5.8: Time-averaged field of LAI over the LITFASS-98 simulation period.

In a following step it is necessary to determine the roughness length z_{0v} [m] and the displacement height d_v [m] over vegetation in dependence of the plant height h_v and LAI. In case of a forest with conifers and/or deciduous trees we use formulae by Brücher (1997):

$$z_{0v} = 0.1 h_v \, , \quad d_v = 0.67 h_v \, . \tag{89}$$

Having green- or grassland, fen or agricultural plants, an approach of Bailey and Davies (1980) is taken instead, where the LAI is also involved:

$$z_{0v} = 0.0275 + 0.281 h_v - 0.028 LAI \, , \quad d_v = 0.245 h_v + 0.091 LAI \, . \tag{90}$$

The only exception is made for z_{0v} in case of maize, where the LAI is not taken into account (Uchijima 1976):

$$z_{0v} = 0.062 h_v^{1.08} \tag{91}$$

We use the fractional plant cover expressed as a function of the LAI (Vogelgesang 1993),

$$f_p = 1.0 - \exp\left(-0.4 \, LAI \right) . \tag{92}$$

Gridpoint values of the roughness length and of the displacement height over a gridbox area are weighted averages from the partial areas with vegetation and bare soil:

$$\begin{aligned} z_0 &= (1.0 - f_p) \, z_{0,surf} + f_p \, z_{0,v} \, , \\ d &= (1.0 - f_p) \, d_{surf} + f_p \, d_v \, . \end{aligned} \tag{93}$$

In the case of bare soil we assume $z_{0,surf} = 0.01$ m and $d_{surf} = 0$ m. For a water surface, $z_{0,surf} = 0.0002$ m is taken. Any dependence on the wind speed is ignored. By z_0 a roughness length $z_{0,M}$ is actually meant, which is defined for momentum fluxes. For latent and sensible heat fluxes we assume a similar length defined as

$$z_{0,H} = 0.1 \, z_{0,M} \tag{94}$$

which is taken from Jürrens (1996). The surface heterogeneity is demonstrated for the LITFASS-98 period in terms of time-averaged fractional plant cover f_p and roughness length

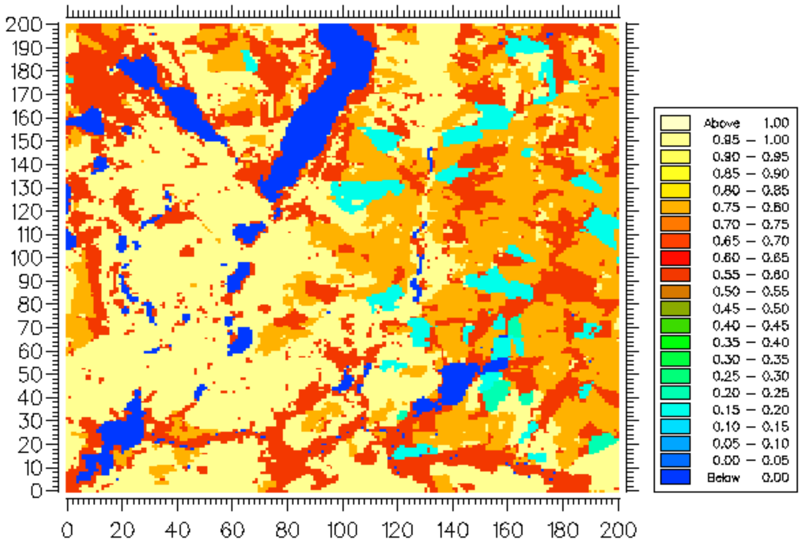

Figure 5.9: Time-averaged field of plant cover (%) over the LITFASS-98 simulation period.

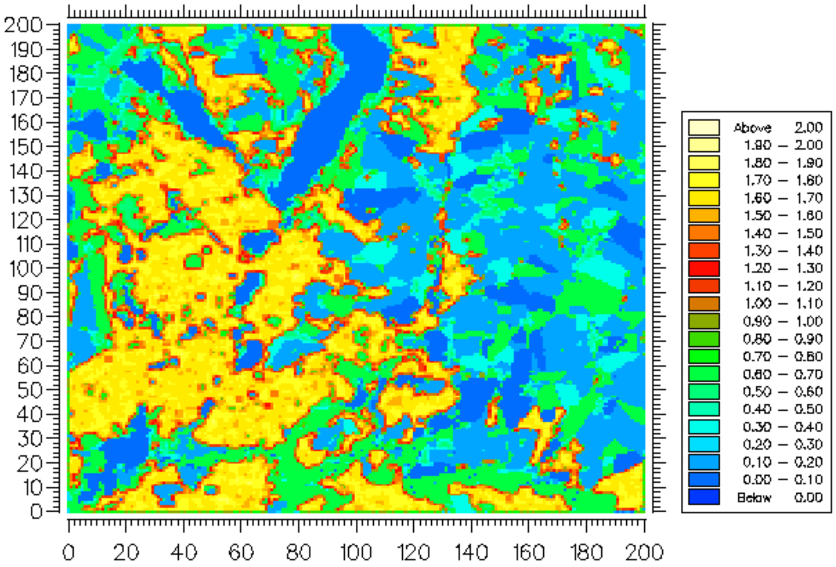

Figure 5.10: Time-averaged field of surface roughness over the LITFASS-98 simulation period.

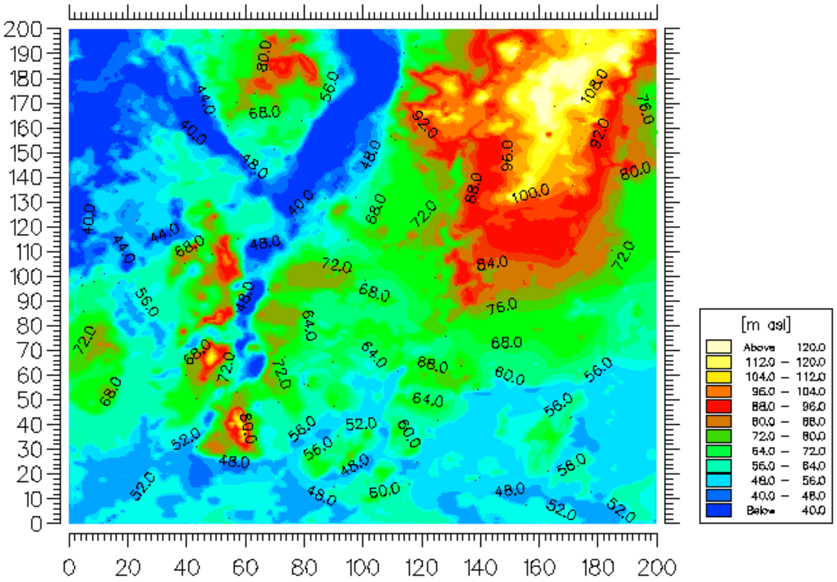

Figure 5.11: Orography plus time-averaged field of displacement height over the LITFASS-98 simulation period.

$z_{0,M}$ in Fig's. 5.9 and 5.10. For the sake of practical convenience the actual field of the displacement height is always added to the time-fixed orography (cf. Fig 2.7b) to have actually a time-variable orography field. That field averaged over the relevant period of LITFASS-98 is shown in Fig. 5.11.

A further group of external parameters immediately relevant to the radiative processes at the surface is related to the reflection of incoming solar radiation and to emission of infrared radiation from the ground. These parameters are albedo and emissivity. They were provided separately for vegetation and bare soil. The influence of precipitation on those parameters will be considered in the following Section 5.2 where the radiation balance components will be deduced from measurements. Here, the values of albedo for vegetation are differently updated (daily or monthly) in dependence of the average growth rate of each plant type. The corresponding data source has been extracted from a VDI Guideline (1994). Finally, we show as examples the distribution of the 'dry' albedo over the total LLM-integration area in Fig. 5.12 and the 'dry' emissivity of vegetation (Fig. 5.13) indicating the specific heterogeneity from this point of view. These values are also averaged in time over the LITFASS-98 period.

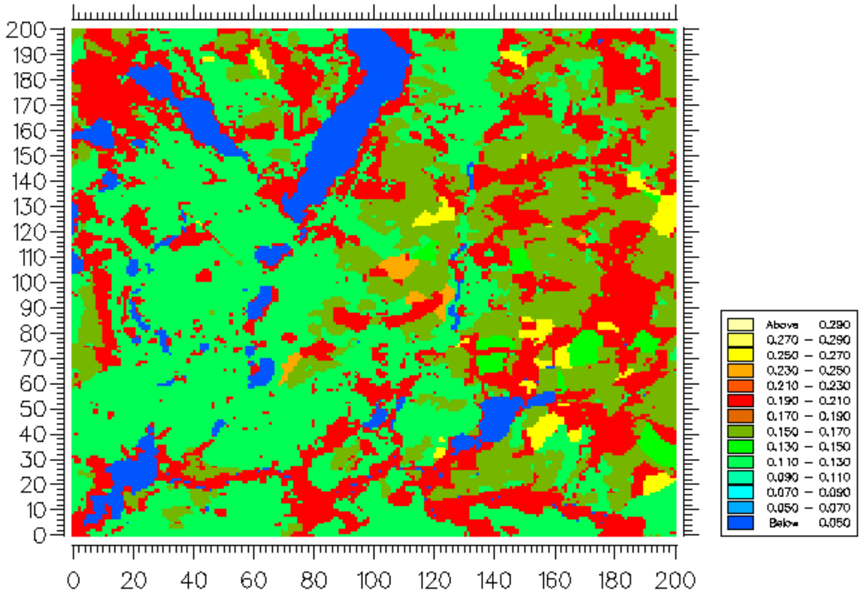

Figure 5.12: Time-averaged field of albedo (vegetation) over the LITFASS-98 simulation period.

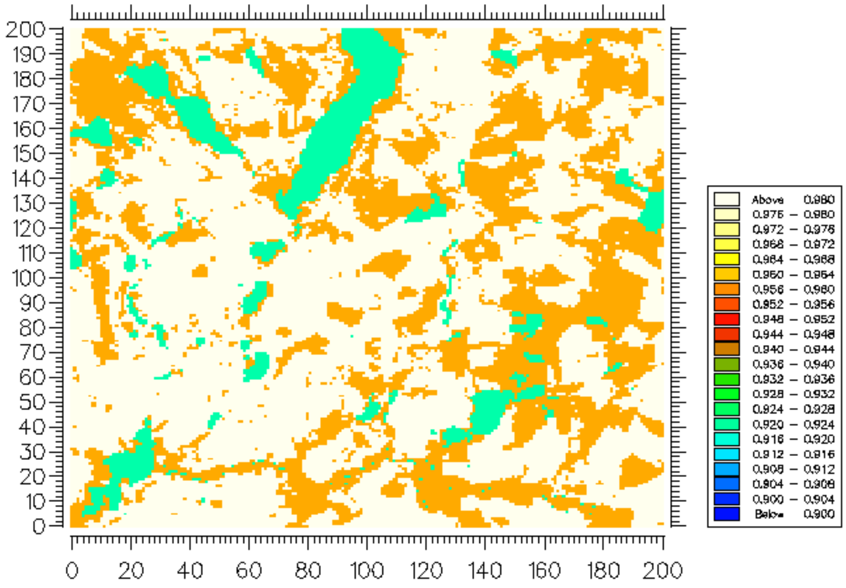

Figure 5.13: Time-averaged field of emissivity (vegetation) over the LITFASS-98 simulation period.

5.2 Radiative Forcing

The task we describe here consists in determining the radiation components of the energy balance at the surface by use of all radiation measurements available in and around the LLM integration area. Satellite information is also taken into account. All these different data sources relevant for our purpose to derive the radiative forcing are compiled in Tab. 5.7. The ground-based radiation measurements are of greatest importance. They are recorded, first of all, at the BSRN-station near the MOL, serving as the reference station, at the radiation measurement site Falkenberg, and at other Energy Balance Stations (EBS) (Lake Kossenblatt, in a pine forest near Storkow, and two special measurement places, in a barley and a triticale field). The latter were only available over the LITFASS-98 period.

Beyond this measurement campaign, further Global Radiation measurement stations have been added since summer 2000 to have meanwhile 8 of them. In Fig. 5.14 the net of radiation measurement points from these different sites is shown, where the mean local METEOSAT pixel positions relevant to our approach are also depicted. As one can see, the area of interest

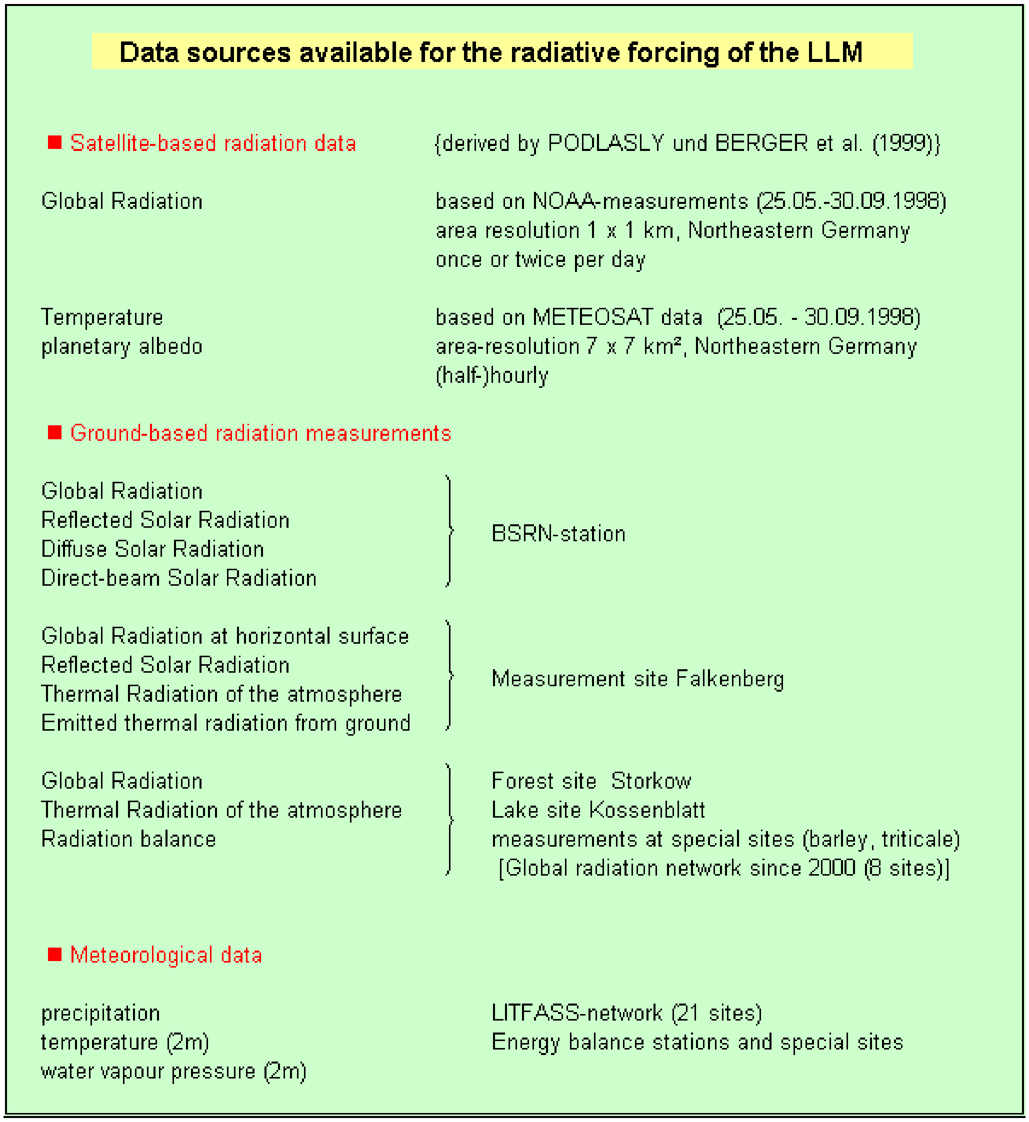

Data sources available for the radiative forcing of the LLM

■ Satellite-based radiation data	{derived by PODLASLY und BERGER et al. (1999)}
Global Radiation	based on NOAA-measurements (25.05.-30.09.1998) area resolution 1 x 1 km, Northeastern Germany once or twice per day
Temperature planetary albedo	based on METEOSAT data (25.05. - 30.09.1998) area-resolution 7 x 7 km^2, Northeastern Germany (half-)hourly
■ Ground-based radiation measurements	
Global Radiation Reflected Solar Radiation Diffuse Solar Radiation Direct-beam Solar Radiation	BSRN-station
Global Radiation at horizontal surface Reflected Solar Radiation Thermal Radiation of the atmosphere Emitted thermal radiation from ground	Measurement site Falkenberg
Global Radiation Thermal Radiation of the atmosphere Radiation balance	Forest site Storkow Lake site Kossenblatt measurements at special sites (barley, triticale) [Global radiation network since 2000 (8 sites)]
■ Meteorological data	
precipitation temperature (2m) water vapour pressure (2m)	LITFASS-network (21 sites) Energy balance stations and special sites

Table 5.7: Data base available for radiative forcing.

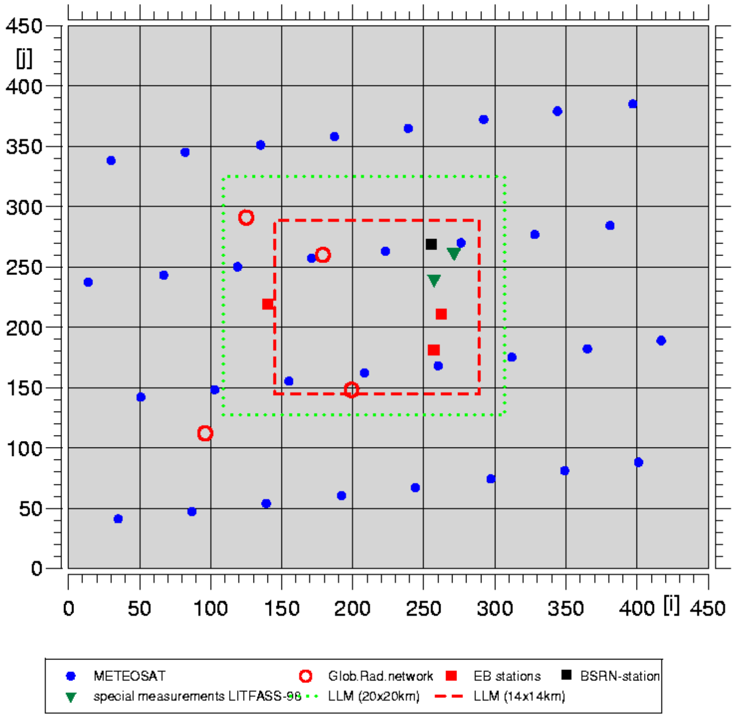

Figure 5.14: Placement of measurement sites recording radiation data.

is chosen considerably larger than the local LLM integration area to be able in any case to apply an interpolation method. In the background NOAA-data are also exploited in order to support the METEOSAT information with its coarser horizontal and spectral resolution. Normal meteorological information, like precipitation, 2m-temperature and water vapour pressure is also involved (Tab. 5.7). These data are provided from a special LITFASS precipitation network with 21 measurement points (see Section 5.3). For further explanation of the instrumental design concerning the radiation measurements during the LITFASS-98 main experimental phase we refer to Beyrich (2000).

For our purpose the satellite data have been made available by Podlasly and Berger (1999). They provided us with a comprehensive data set of METEOSAT and NOAA measurements over the period 25 May - 30 September 1998 with our LITFASS simulation time interval embedded. The METEOSAT data consist of temperature and planetary albedo, while the Global Radiation was derived directly from the NOAA satellite. In the latter case the radiation data have a high resolution of about 1×1 km^2 which would be appropriate for LLM. Unfortunately, these data are available only once ore twice a day over the area of interest. In contrast, the METEOSAT information can be obtained in a relatively high time-resolution, that is every 30 minutes, but due to its poor spectral resolution the Global Radiation data cannot be similarly derived (cf. Podlasly and Berger 1999).

This dilemma of different shortcomings of the two available satellite data sources can be reduced by a method to combine both. In effect, our approach rests on deducing a Global Radiation field from these satellite data by combining the available information with the ground-based measurements of Global Radiation as the key radiation component relevant to the LLM forcing. For the LITFASS-98 period the method cannot do without satellite information due to the small number of ground-based radiation stations inside the LLM integration area. The following approach may be characterized as some calibration of the available METEOSAT information of temperature and planetary albedo by the Global Radiation field, derived from NOAA data at METEOSAT pixels.

The area of satellite data shown in Fig. 5.15, which covers Northeast Germany with the LLM-area as a tiny sub-area in the eastern part in it. In this figure the 18 June 1998 at 12.30 UTC is chosen, when the NOAA data coincide almost exactly in time with the METEOSAT information. At first glance, the Global Radiation from NOAA data (Fig.5.15a) seems to be not highly correlated neither to the temperature (Fig. 5.15b) nor to the albedo (Fig. 5.15c). Here, qualitative arguments might be helpful to put forward the matter. In this line, we generally expect a significant relation between cloudiness on the one hand and temperature and albedo on the other hand. In case of compact clouds the satellite measures deeper temperatures together with a higher albedo, which must be correlated with a correspondingly reduced Global Radiation at the ground. Inversely, one expects in cloudless areas with relatively high values of temperature and smaller values of albedo increased values of Global Radiation at the ground.

This leads us to the definition of an Insolation parameter s, which is an appropriate combination of albedo *and* temperature, as available from METEOSAT data, in such a way that

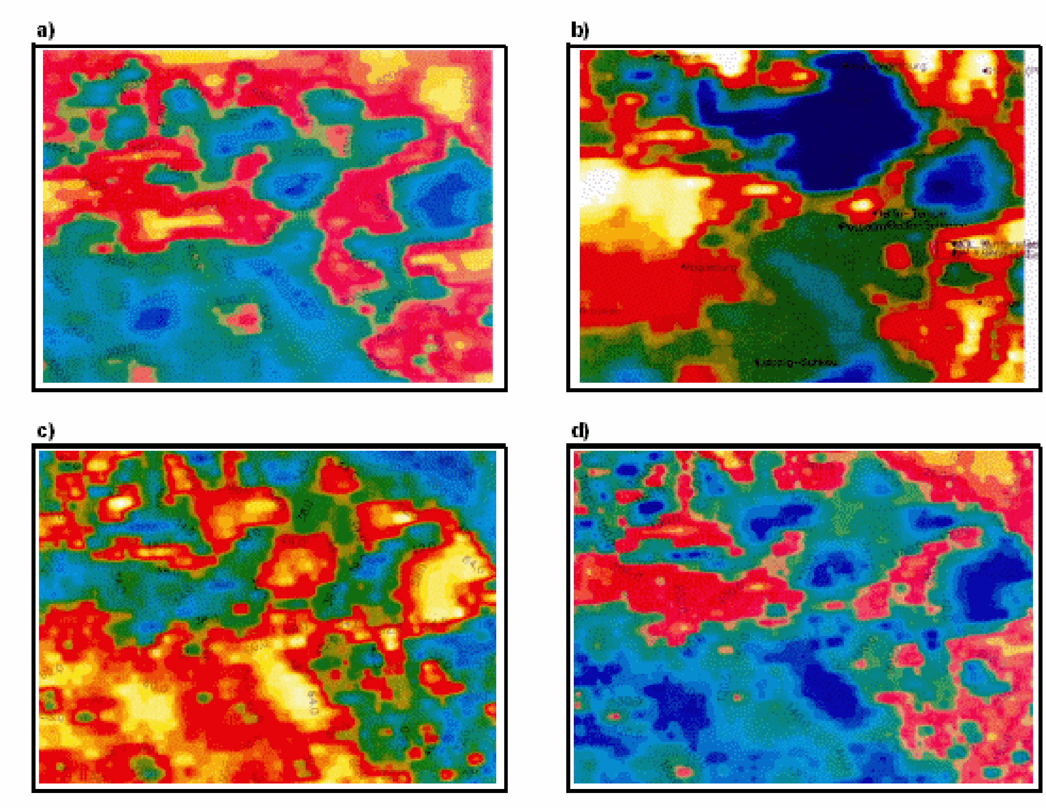

Figure 5.15:

a) Field of Global Radiation derived from NOAA data and adapted to the coarser METEOSAT resolution.

b) Temperature field based on METEOSAT data.

c) Field of Planetary albedo based on METEOSAT data.

d) Field of Insolation parameter.

All fields refer to north-east Germany (18 June 1998, 12:30 UTC).

it has a significantly high correlation to the known Global Radiation fields directly gained from the NOAA satellite. A comparison of the s-field in Fig. 5.15d with the NOAA Global Radiation field in Fig. 5.15a demonstrates such a desired correlation. By use of all available NOAA- and METEOSAT data taken out of the entire data set the Insolation parameter has been found as a result of statistics:

$$s = a_s T\,(1.0 - 0.01\alpha_p) \,+\, b_s\,. \tag{95}$$

α_p is the planetary albedo [%] and T [K] the temperature from METEOSAT, the constants are found to be $a_s = 0.0053K^{-1}$ and $b_s = 0.0227$. After deriving relation (95) from NOAA Global Radiation data, it can now be used to determine from the METEOSAT information (from T and α_p) the Insolation parameter field s every 30 minutes.

In the next step a local fitting of the s-field to the Global Radiation measurements at the ground is performed such that the s-field is slightly shifted in the horizontal until a measure of distance to the Global Radiation values at the given 5 measurement points becomes minimal. In Fig. 5.16 the s-field is shown for the same selected time as in Fig. 5.15 after the operations just described. Although this field has a relatively coarse structure due to the METEOSAT-pixel resolution and a 30 minutes-resolution in time, compared to the LLM-scale resolution, the s-field serves as a necessary background information towards a horizontally inhomogeneous and time-variable Global Radiation field at the surface. Thus, at measurement points associated Global Radiation (G-) and s-values are used to deduce a linear s, G-relation. In such a way we obtain all s-values available as G-values which are finally exploited as additional information to the genuine surface measurements in a horizontal interpolation onto the LLM-gridpoints.

Since the ground-based measured values are delivered every 10 minutes, a further time-interpolation from 30 down to 10 minutes is carried out to obtain finally a surface Global Radiation field G over the 20 × 20 km^2 LLM integration domain with 199 × 199 gridpoints and a 10-minute input frequency. As can be seen from Fig. 5.17, the method described above is able to provide the LLM with a horizontally inhomogeneous G-field, where real

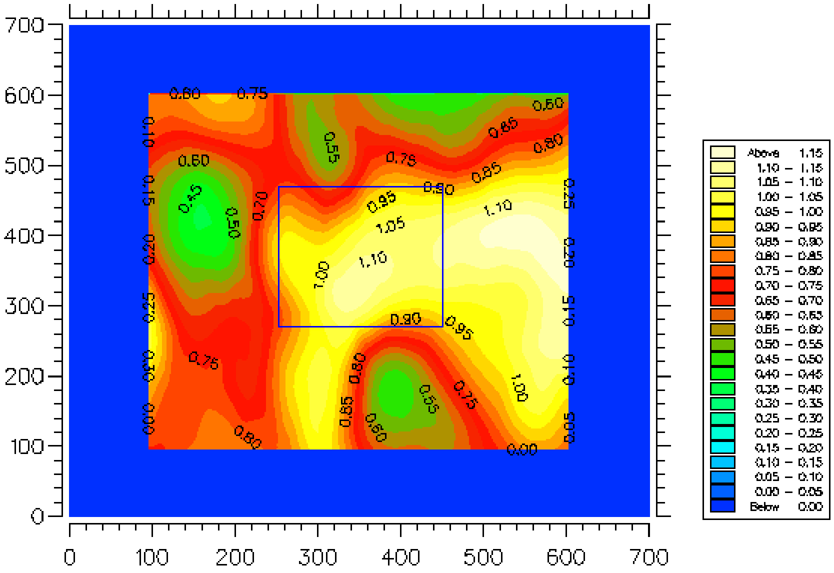

Figure 5.16: Distribution of Insolation parameter for 18 June 1998, 12:30 UTC. The LLM area is embedded in the centre.

cloudiness is involved. This approach has been used for all LLM integrations over our LITFASS-98 simulation period (1 June-20 June 1998). As mentioned above, the number of Global Radiation recording stations was only extended after this period, in summer 2000. In order to demonstrate the additional gain of information from this further technical effort, Fig. 5.18 shows the sequence of G in 10minute-time intervals over the LLM-area with rapid time-changes of that radiation pattern accompanied with rather sharp gradients.

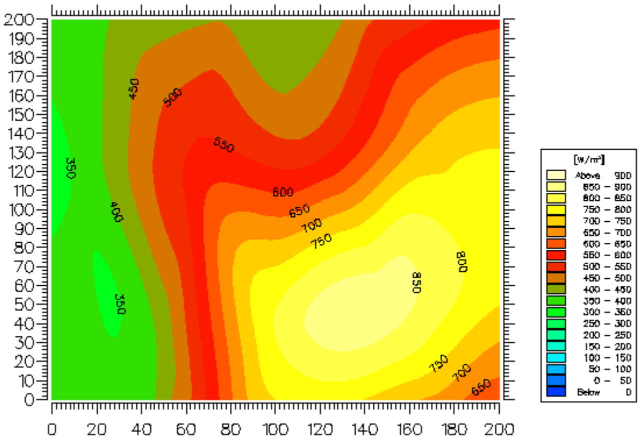

Figure 5.17: Global Radiation field in the LLM area for 18 June 1998, 12:30 UTC (see text).

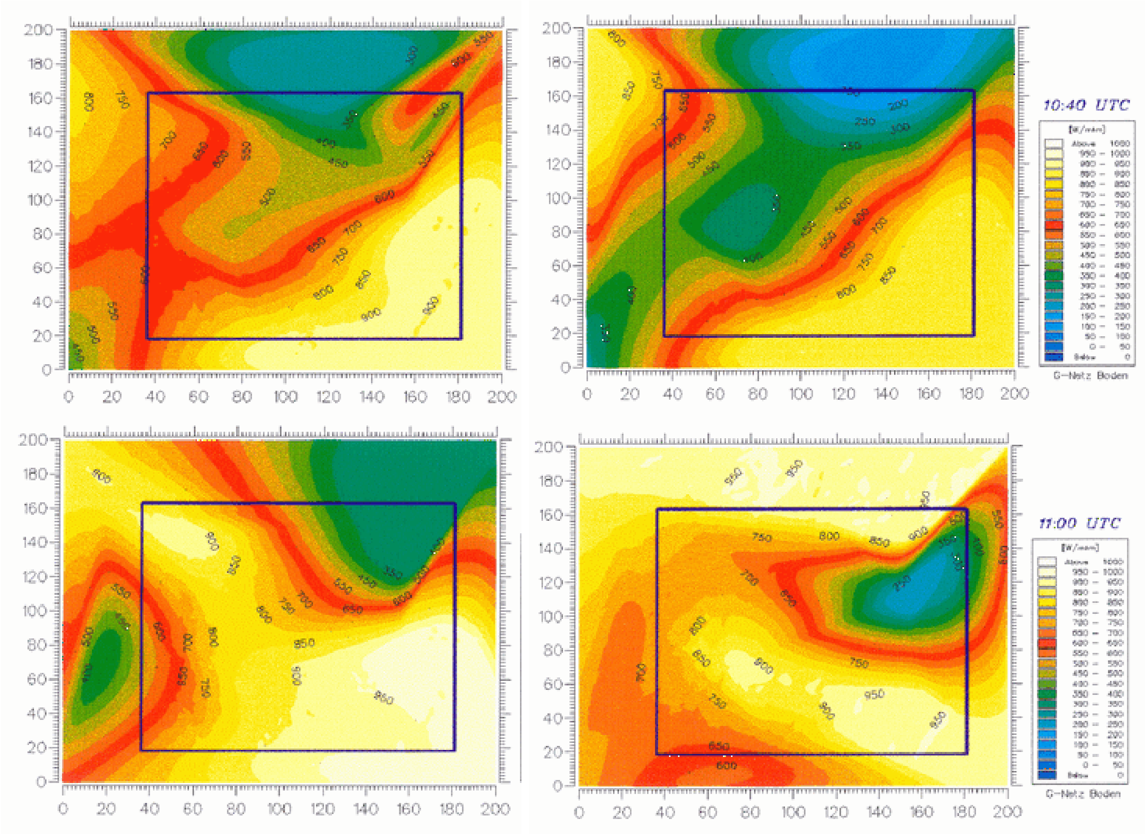

Figure 5.18: Time sequence of Global Radiation fields deduced every 10 minutes from an extended surface network on 21 June 2000. Top left: 10:30 UTC; top right: 10:40 UTC; bottom left: 10:50 UTC; bottom right: 11:00 UTC.

The Global Radiation G found in this way is, however, not the final result. To make the incoming solar radiation flux still more realistic, the inclination of the natural surface has to be taken into account. The corresponding correction necessary is, however, effective only to the Direct-beam Solar Radiation I. For that purpose we need an approach to split up G into its components I plus Diffuse Solar Radiation D, that is $G = I + D$. Assuming that this splitting has been carried out, the correction of I due to the orographic inclination can be performed. All details of that operation including the derivation of the inclination angle from the given orography up to the determination of the modified solar height (depending on the varying sun position over the day and the season) will be dropped here. This method is standard.

The splitting procedure needs, however, further explanation, and for that purpose we introduce a Global Radiation Reduction factor R_s, which may be defined with reference to Davies et al. (1975) as

$$G = G_0 \, R_s \, . \tag{96}$$

This relation separates the Global Radiation at the ground, G, into a Global Radiation component of the cloudless case G_0 multiplied by a Reduction factor R_s. The latter describes the reducing influence of clouds in the solar spectrum. After Davies et al. (1975) the parameterization of G_0 and R_s may be given as follows.

$$\begin{aligned} G_0 &= a_R + \frac{b_R}{2} \left(\frac{r_0}{r}\right)^2 S \, \sin\gamma \left[\psi_{wa}(\psi_{ws}\psi_{rs}\psi_0 + \sqrt{\psi_0})\right] \, , & (97) \\ R_s &= \left[1 - \left(1 - \frac{a}{G_0 m_a} \exp(-b m_a)\right) n\right] (1 - \alpha_c \alpha_g n) \, , & (98) \end{aligned}$$

with the following explanations and definitions of parameters in the G_0-relation (97): $(r/r_0)^2$, γ, S are measures of astronomical excentricity, solar height at given location and time, and solar constant, respectively. ψ_{wa}, ψ_{ws}, ψ_{rs}, ψ_0 are transmission coefficients due to water vapour absorption, water vapour scattering, Rayleigh-scattering and scattering from dust. The regression coefficients a_R and b_R are introduced to fit this relation to the local conditions of Lindenberg.

The R_s-relation (98) depends on parameters describing different cloud properties, a and b are coefficients specifying the cloud type, a_c is the cloud albedo seen from below, n describes the cloud coverage ($0 \leq n \leq 1$), m_a defines the optical mass of the atmosphere and α_g is the albedo of the ground. The reliability of relation (96) together with the parameterizations of G_0 and R_s has been proved by use of NOAA-radiation fields. For the problem discussed here and in the following we confine the parameterization to G_0. The determination of the Reduction factor R_s follows from (96) by use of ground measurements of G (actually determined from ground measurements and METEOSAT/NOAA-satellite data as described above). Such an R_s-field is shown in Fig. 5.23a.

After having found R_s, it is possible now to separate D and/or I from the preliminary G. Therefore, we assume that the ratio D/G is a function of R_s:

$$\frac{D}{G} = \frac{D}{D + I} = f(R_s) \, . \tag{99}$$

For the cloudless case, with $R_s = 1$, we expect the ratio to have a minimum, $f(1) = D/G_0$. If the sky becomes overcast ($I \rightarrow 0$), R_s approaches to a minimum and the ratio to unity. Fortunately, the Diffuse Solar Radiation D is directly recorded at the BSRN-station at MOL and each 10 minutes available. Taking advantage of these data, the function $f(R_s)$ can be determined. In Fig. 5.19 the ratio D/G is plotted against R_s from measurements and by

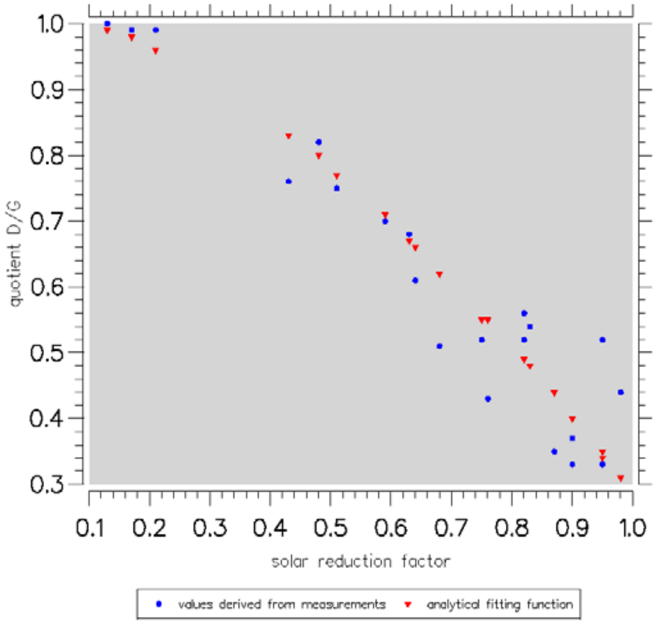

Figure 5.19: Quotient D/G as empirical function of solar Reduction factor (see text).

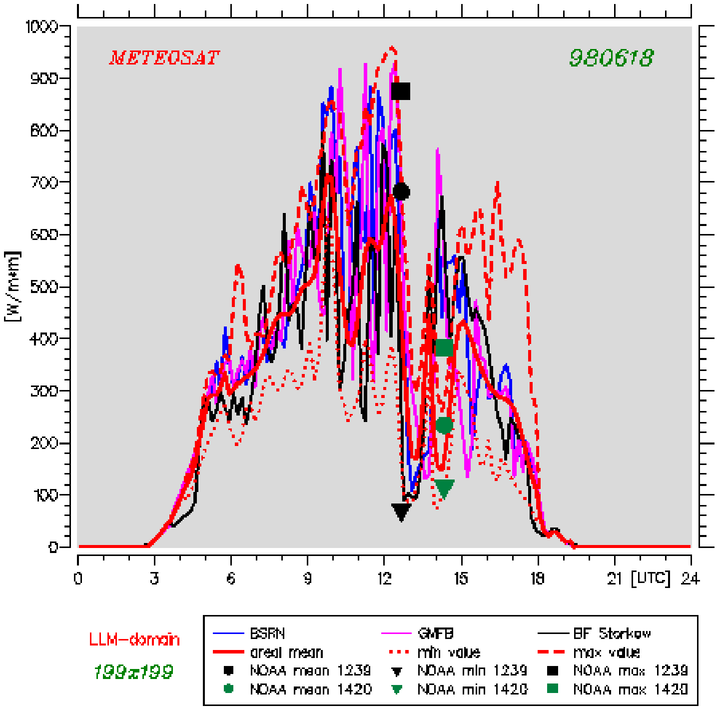

Figure 5.20: Diurnal variation of measured and derived Global Radiation over the LLM area (18 June 1998). Time variations of deduced area-average, -maximum and -minimum against selected NOAA- and surface measurements of Global Radiation at BSRN-station, forest station (BF Storkow) and Falkenberg site (GMFB).

using an analytical curve fitted to these data. The latter is assumed to be the appropriate tool to separate D and/or I from the given G which makes it immediately possible to modify I in the above sense and use that result together with the unchanged D to obtain the final composite of G.

Before we continue to derive further radiation balance components for the radiative forcing of the LLM the time-variation of G is shown in Fig. 5.20 for the same selected day (18 June 1998) from the LITFASS-98 period as in previous figures. This day was a particular occasion for LLM-simulations because of a helicopter flight with a sonde. By chance, this day was characterized by prevailing convective weather. The time-variations of G show in general rapidly passing small-scale cloud patterns accompanied by sharp peaks and gaps in the morning. At noon, a compact cloud field covers the entire LLM-area, from which a maximum of about 900 Wm^2 has been reduced down to 100 Wm^2. As seen in the figure, the various plots of G refer to three different recording stations and show in parallel the time-variations of the area-average, -maximum and -minimum which demonstrates the considerable spread of G-variations over the LLM-domain and so the radiative inhomogeneity at the surface.

In order to complete the Solar Radiation balance SB, we have to determine the Reflected Solar Radiation G_r, too, and to subtract it from the Global Radiation G:

$$SB \,=\, G \,-\, G_r\,. \tag{100}$$

Since D and I have already been derived in connection with the determination of G, we are now immediately able to carry out the necessary separation of G_r into the diffuse and the direct-beam component:

$$G_r \,=\, \alpha_d D \,+\, \alpha_{par} I\,. \tag{101}$$

Therefore, in accordance with (101), the determination of G_r can be reduced to the determination of the diffuse albedo α_d and the albedo of a parallel radiation beam α_{par}. Concerning the diffusive albedo α_d, we refer to comments at the end of Section 5.1 about the availability of external parameters like dry, diffuse albedo and emissivity, which are already prepared to be used separately for bare soil and vegetation. In case of precipitation both albedo components are modified provided the actual amount of rainfall exceeds 0.5mm over a 10minutes-interval. Then the surface is assumed to be wet. In this case the albedo of vegetation is reduced by 10 percent and the albedo of wet bare soil is treated in accordance to the VDI Guideline (1994). The diffuse albedo follows then by use of a weighted average of both components with the

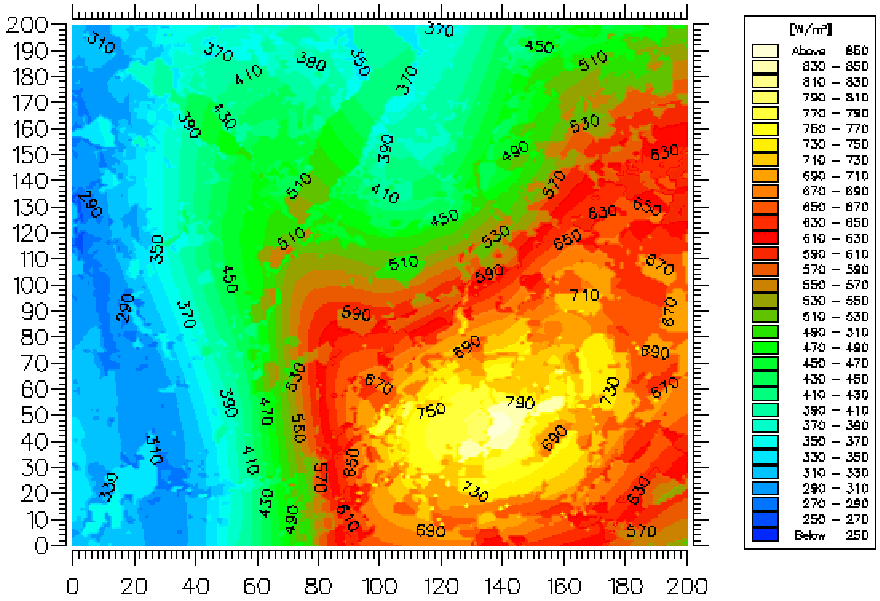

Figure 5.21: Example of Solar Radiation balance field over the LLM area (18 June 1998, 12:30 UTC).

fractional plant cover. This is similar to the treatment of the roughness length in (93). In the following step, the albedo of a parallel radiation beam is calculated as a function of α_d and solar height γ (Ritter, cf. Doms and Schättler 1999):

$$\alpha_{par} \;=\; \frac{1 + \dfrac{\gamma}{2(\alpha_d - 1)}}{\left(1 + \dfrac{\gamma}{\alpha_d - 1}\right)^2} \,. \tag{102}$$

Using α_d and α_{par}, the reflected component G_r can be found from (101), which leads to the Solar Radiation balance (100). An example of an SB-field is shown in Fig. 5.21.

In a final step we still have to determine the Thermal Radiation of the atmosphere A and the Thermal Radiation E emitted from the ground. In case of A we need a method which also operates on the basis of available Global Radiation data G. In a similar way an Amplification Factor M_{IR} is introduced in order to determine A by use of a reference value

$$A_0 \;=\; (\alpha_{IR} - \beta_{IR} \exp\{-\gamma_{IR} e_{2m}\})\; \sigma T_{2m}^4 \,, \tag{103}$$

valid for cloud-free conditions (Rietschel 1994), that is, by

$$A \;=\; M_{IR} A_0 \,. \tag{104}$$

Here, the general problem is shifted to the determination of M_{IR}, while A_0 can easily be approximated by use of temperature T_{2m} and water vapoure pressure e_{2m} at 2 meters above the ground as meteorological input-parameters taken from measurements. During simulation runs these data are directly provided from the LLM in order to determine the A_0-values in a consistent manner to the model. α_{IR}, β_{IR} and γ_{IR} are empirical constants with reference to Rietschel (1994), and σ is the Stefan-Boltzmann constant. The true problem is to estimate

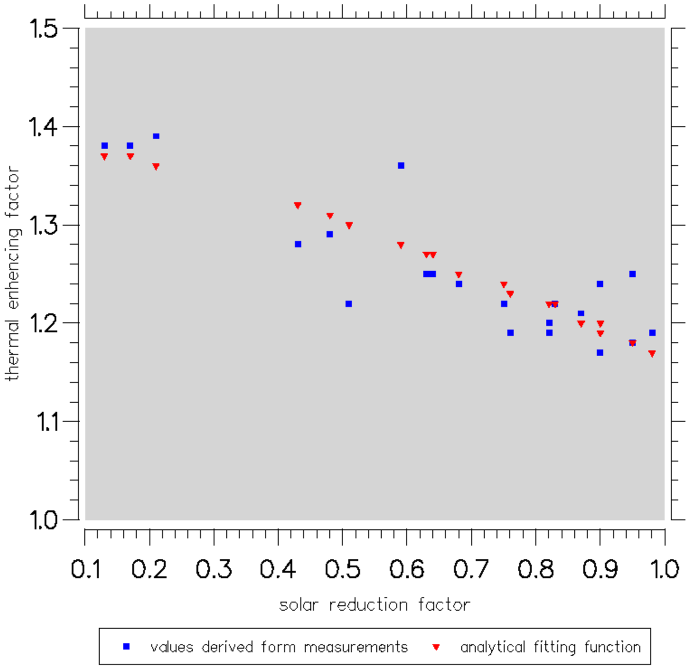

Figure 5.22: Empirical relationship between thermal Amplification factor and solar Reduction factor for a given time interval on 18 June 1998, 9 - 12 UTC (see text).

the factor $M_{IR} \geq 1$. In order to have an approach consistent with our treatment of the Solar Radiation component, it is reasonable to find out an empirical relation between R_s and M_{IR}, which is expected to have in a crude manner a reciprocal proportionality. This means, the enhancement of Thermal Radiation from the atmosphere compared to the cloud free case must directly be related to a reduced Global Radiation, which is expressed by a decreasing Reduction factor R_s. In our approach, this relation has been determined every 10 minutes and is shown for a selected time interval in Fig. 5.22. On the basis of this operation M_{IR} is given and the estimation of A follows using (104). Fig 5.23a,b demonstrates the consistent relation between R_s and M_{IR}.

In the following the Thermal Radiation emitted from the ground,

$$E = \varepsilon \sigma T_{sfc}^4 \tag{105}$$

must be estimated, Here, the problem confines to the use of the infrared emissivity ε, which has already been provided as an external parameter field. Similar to the diffuse albedo, these values have been provided separately for vegetation and bare soil and possibly modified owing to precipitation.

We close the Section with a marginal remark concerning the Photosynthetically active Radiation P, which is needed in the vegetation parameterization part after Dickinson of the soil model 'terra'. P is approximated by the very simple relation $P = 0.5G$. A view on Fig. 5.24 may finally serve us as a summary of the present section. This figure is self-explaining. To organize the important forcing due to radiation processes from below, four groups of input data are of interest. These are ground-based radiation measurements, preprocessed satellite data from NOAA- and METEOSAT-instruments, meteorological near-surface data and basic data as orography, land use and soil type maps to derive relevant external parameters from them. All these data are stored in order to make a synthesis having finally the ground-based fields relevant for the radiative forcing (Solar Radiation balance, infrared Amplification factor, precipitation (cf. Section 5.3), infrared emissivity, Photosynthetically active Radiation) and the external parameters (cf. Section 5.1) which are orography plus displacement height, roughness length, LAI, fractional plant cover, root depth and landpoint mask.

These data are always ready for LLM-access. In case of radiation data their input to the LLM takes place every 10 minutes of integration time. All computer runs are carried out at

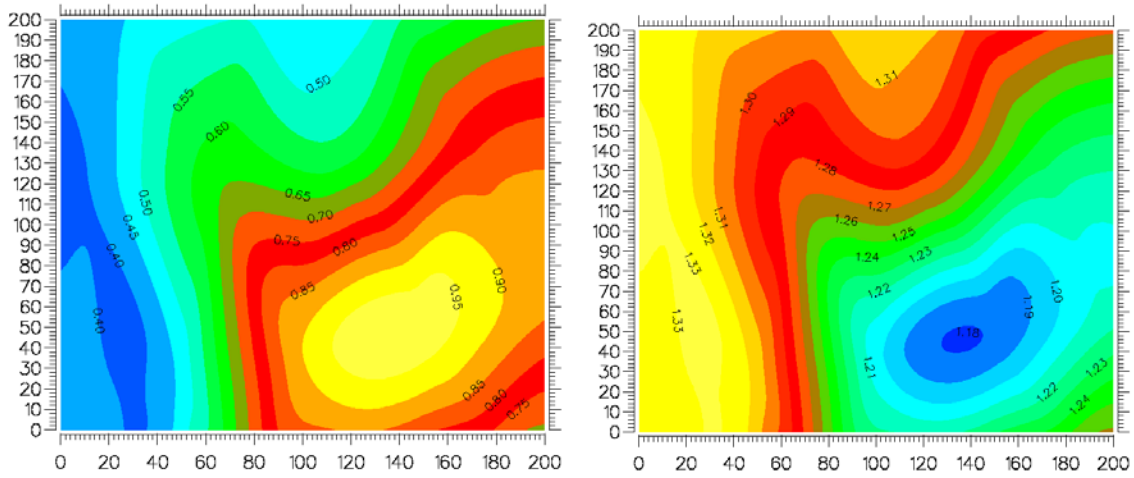

Figure 5.23: Consistent distributions of solar Reduction factor (left) and thermal Amplification factor (right) over the LLM area.

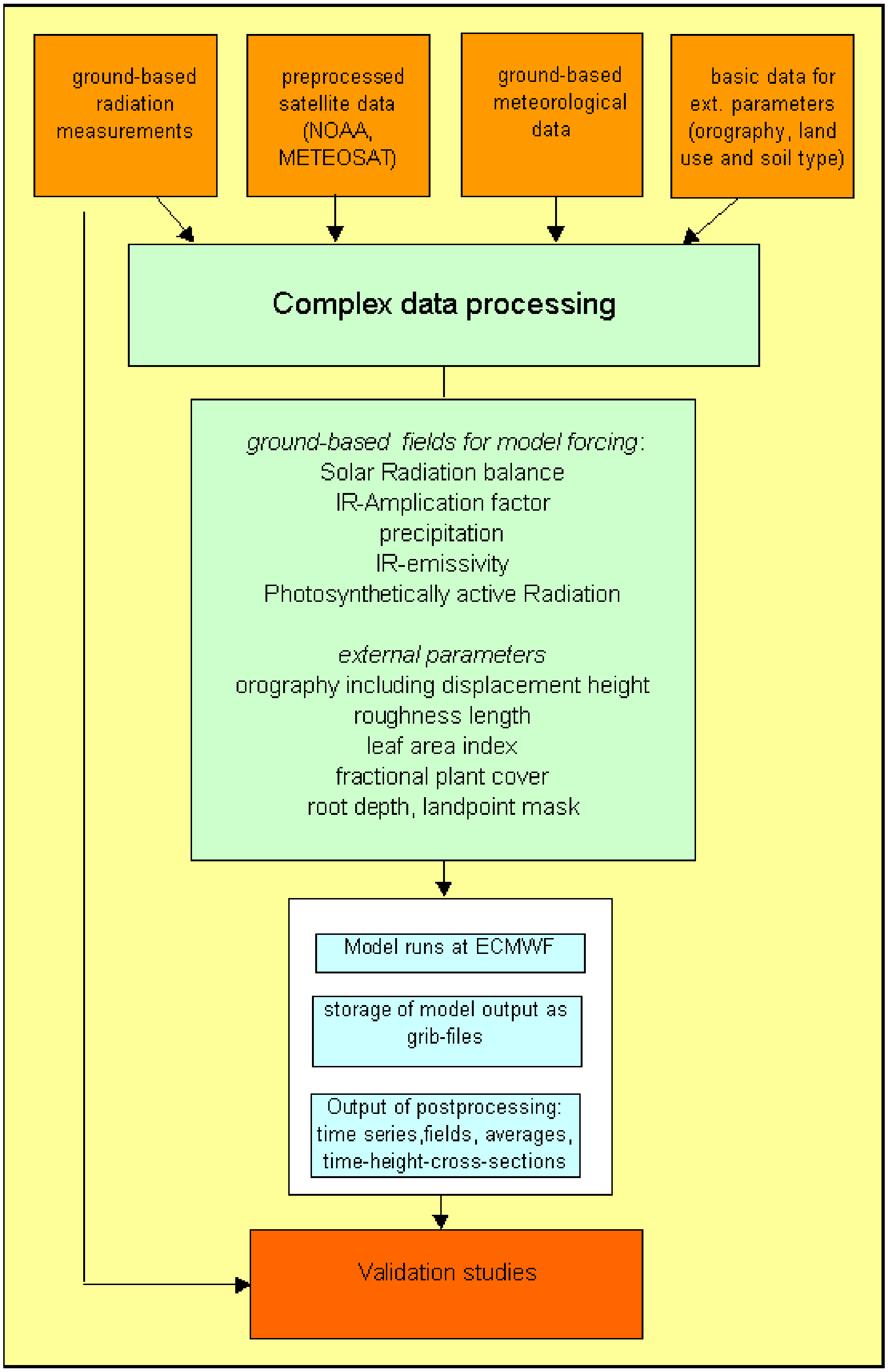

Figure 5.24: Summarizing scheme of data processing for physical forcing at lower boundary.

ECMWF on the VPP700 machine where all LLM output-arrays are also stored as Grib-files, and so the postprocessing is organized to be performed there, before results as time-series, selected fields, averages and specified sections of fields are transferred to Potsdam. There, the validation of the LLM products is executed by direct use of measurements, which are e.g. ground-based Radiation balance records. Ultimately, this kind of validation is part of a more general validation system as shown in Fig. 1.1.

5.3 Precipitation Forcing

We have already explained in Section 2.5 that in view of real-case simulations with the LLM its precipitation parameterization is ignored and the precipitation flux reaching the earth surface is inserted by a real-data field. This philosophy is similar to what has been carried out in the previous Section concerning the radiative forcing. In the following we describe the way how the horizontal distribution of precipitation at the surface is analyzed from given measurements. For that purpose a special network of Hellmann gauges commonly in use and automatically recording pluviometers has been established. RADAR data are not available.

In Fig. 5.25 the placement of 19 Hellmann gauges and 12 pluviometers is depicted. As can be seen, most of the pluviometers are placed within the extended LLM-area (199 × 199 gridpoints), while the gauges are distributed also far outside. At 7 places gauges and pluviometers have the same location. For these stations the pluviometer measurements are only used. Both instruments differ from each other by summing up the rainwater over quite different time intervals. In the gauges the rain water is gathered to obtain sums over 24 hours, normally observed at 5, 6 or 7 UTC in the morning, while the pluviometer records yield very high-resolved sums over every 10 minutes. By a simple operation the pluviometer values will be used as reference measurements to derive pseudo-values from the 24hour-Hellmann-data with the same high time-resolution. Then all measurements are put together for a following analysis.

The production of such pseudo-values may be demonstrated by Fig. 5.26. In Fig. 5.26a a pluviometer record is shown over 1 June 1998 at the village Limsdorf, placed in the LLM-area. Already in the morning a maximum of 5.6 mm/10min occurred during a heavy shower, and further showers with diminishing intensity took place during the second half of this day.

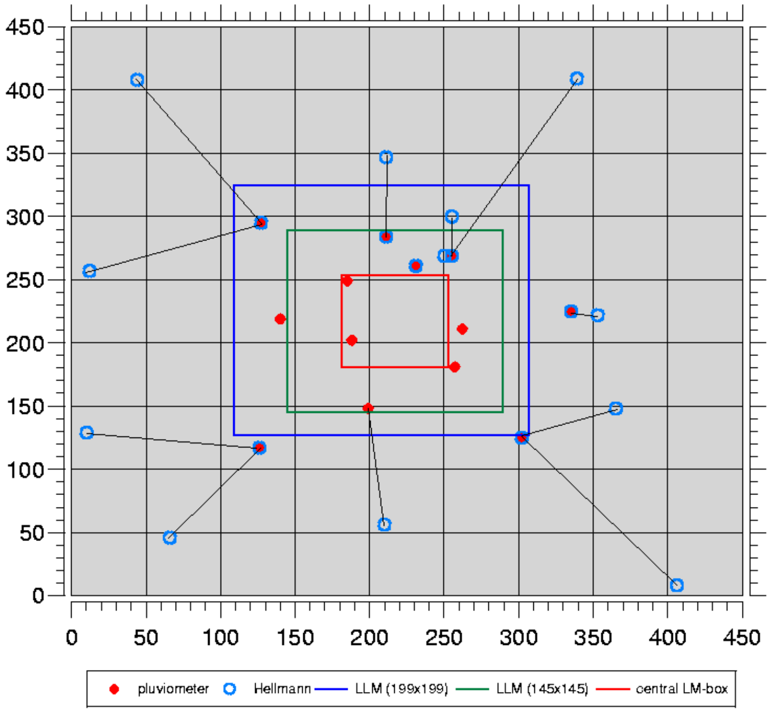

Figure 5.25: Placement of pluviometers and Hellmann gauges within and around the LITFASS area.

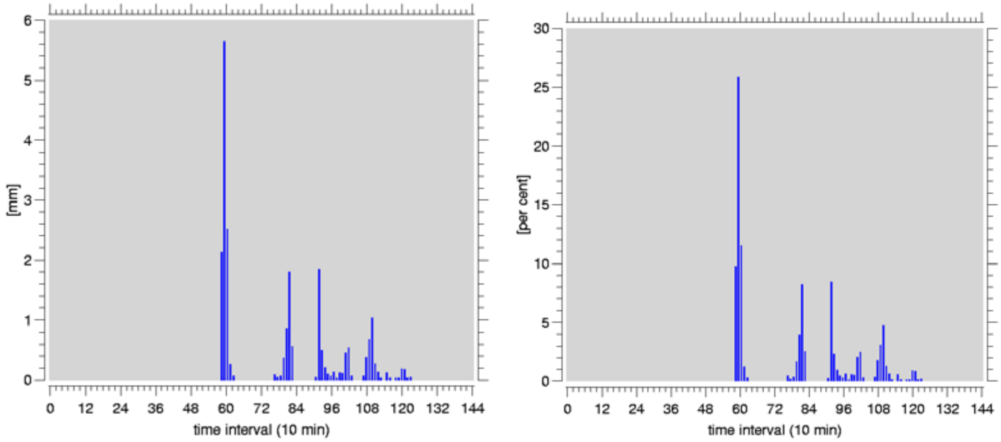

Figure 5.26: Time series of precipitation sums on 1 June 1998 at Limsdorf.
Left: Precipitation sums (mm/10min) in the diurnal course (144 time intervals of 10 minutes).
Right: Percentage distribution of 10-minute precipitation sums referred to daily sum (144 time intervals of 10 minutes).

The total sum amounts to 21.8 mm/day. With reference to this sum the time-series shown can easily be transformed into a corresponding time-variable percentage-distribution (Fig. 5.26b). Such a percentage-distribution found from each given pluviometer is then assumed to be valid for the nearest Hellmann-stations. (This is symbolized by connecting lines in Fig. 5.25). From this approximation the pseudo-values with a 10minute-resolution can be determined from the 24 hour-sum of the respective gauge. The irregular horizontal distribution of precipitation obtained every 10 minutes as explained above is the data basis for the following interpolation onto the LLM-gridpoints. This interpolation rests on a triangulation standard method.

The outcome of such treatment is shown in Fig. 5.27 for the same convection situation of the 1 June 1998 at 9:50 UTC, with a maximum near Limsdorf (cf. the peak at this time in

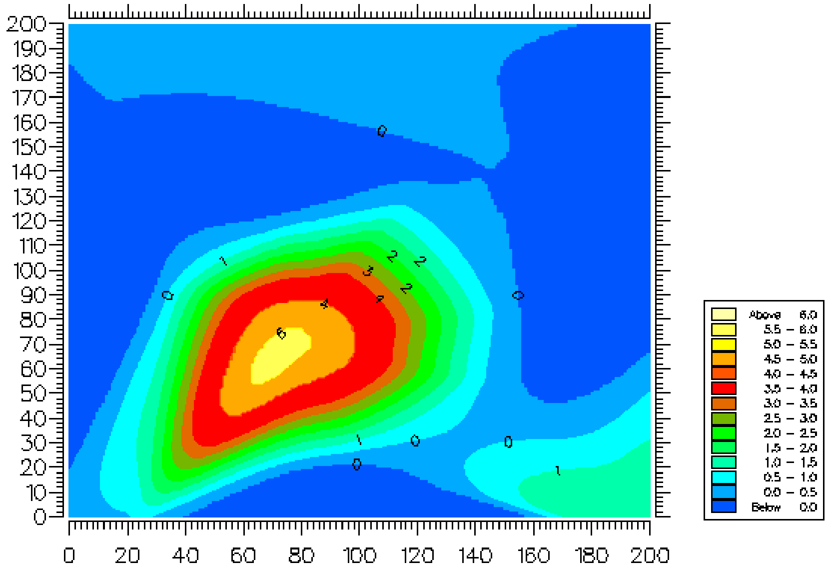

Figure 5.27: Deduced precipitation field over the LLM area on 1 June 1998, 9:50 UTC.

Fig. 5.26a). In this way precipitation forcing fields are made ready for the LLM-access every 10 minutes similar to that of radiation data. In case of large-scale precipitation our method presented seems to be sufficient. In case of convective rain events, however, further research supported from RADAR data is desirable in order to find out more adequate fine-scale field structures.

5.4 Soil-Moisture Modelling

Soil-moisture modelling is a specific problem of great importance for real-world simulations with the LLM. Obviously, that topic is seen to be closely related to the precipitation analysis we have treated in Section 5.3. The soil-moisture is a very complex factor caused by water influx due to precipitation. It interacts permanently with a diversity of processes like interception, surface runoff, infiltration, evapotranspiration, vertical water transport within the soil and runoff into the ground water. These processes again depend strongly on the soil properties, and they have very different characteristic time-scales. The longest of them make up the memory of the soil which is important to consider for the soil moisture initialization. This problem is of particular interest and must be solved in a pragmatic way.

While the LLM integration mode is generally characterized by a time-dependent external forcing founded on measurements – these are composite profiles (Chapter 4), external parameters (Section 5.1), surface radiation (Section 5.2) and precipitation (Section 5.3) – soil moisture measurements are only available at one measurement point at the Falkenberg site. As will be pointed out, this single measurement is absolutely insufficient to support an initialization approach needed and seems also to be unsuitable for the validation of simulation. It follows that LLM-simulations themselves are thought to be used as a possible soil moisture initialization procedure. These LLM-integrations are pre-runs started sufficiently long before the beginning of the actual run in order to produce a soil moisture spin-up towards a realistic initial field. The initial soil-moisture state of such a spin-up LLM-run is assumed to be a reasonable approximation, and this run will be controlled from the real time-dependent radiative and precipitation forcing as discussed above. We have to be aware, however, that

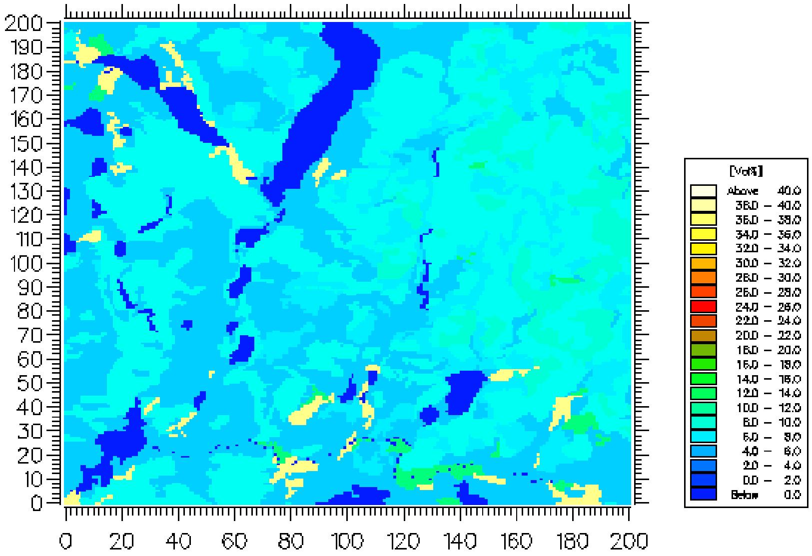

Figure 5.28: Initial field of soil moisture referred to the upper soil-model layer (1 June 1998, 00 UTC).

the approach is dependent on the potential of the coupled soil-model (Jacobsen and Heise 1982, Doms and Schättler 1999).

Because all LLM-simulations we have made were strictly connected with the measurement equipment installed for the project LITFASS-98 and further on for LINEX 2000, corresponding pre-runs were dictated from these facts and from the availability of real data before these campaigns. In case of LITFASS-98 it would have been desirable to have the basic data for the radiative forcing and of precipitation already since April 1998, in order to start the spin-up simulations in time with respect to a very dry May. Unfortunately, satellite data have not been available in that time, and the rain gauge network was still in preparation. While in case of LINEX 2000 the spin-up runs were possible already since 10 August 2000, our LITFASS-98 simulation had to be performed without such a desirable soil-moisture spin-up before.

For LINEX 2000 the spin-up start at 10 August was accepted due to heavy rain during August which makes the soil-memory from the months before possibly lost. In case of LITFASS-98 with its simulation time from 1 June to 20 June 1998 we are going to point out the soil moisture course from LLM-integrations over that time at a selected gridpoint which coincide with the only measurement point, and the model had to start with an approximate soil-moisture field without a necessary pre-run. That approximation is as follows. By use of the only measured value the percentage of the field capacity at the measurement point is known as an additional useful information. Since the horizontally inhomogeneous distribution of the field capacity over the LLM-domain is also known from the associated soil-type map, the assumption of the same percentage at each gridpoint leads immediately to an inhomogeneous soil-moisture field. This is assumed to be valid for both active model layers. In Fig. 5.28 the result is shown for the 1 June 1998. It is valid for the upper layer of the soil-model 'terra' having a thickness of 0.1m. (The present soil-model version has two active layers. The second layer, below, reaches from 0.1 m to 1 m depth.)

In the Fig. 5.29 the time variation of the soil-moisture at the gridpoint Falkenberg is shown as the result of an extensive LLM-simulation over all 20 days of the LITFASS-98 simulation period against the measurements there. For that experiment the LLM has externally

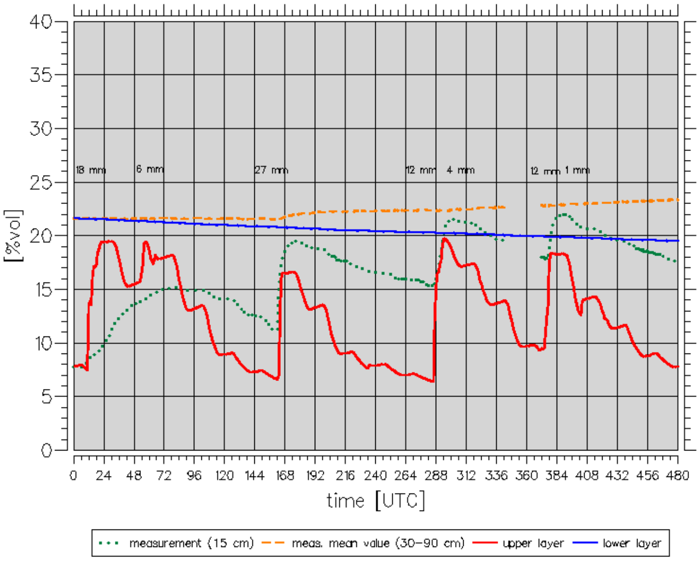

Figure 5.29: Time series of measured and LLM-simulated soil moisture over the LITFASS-98 simulation period from 1 June - 20 June 1998.

been driven at the lateral and upper boundaries only by radiosonde information, because composite profiles have been available only at 9 days of the whole simulation period (9-14, 18-20 June 1998). In parallel to the measured and simulated soil-moisture curves the 24 hour-rain-sums at 7 days with precipitation can also be seen in Fig. 5.29.

Prior to an interpretation of the LLM-results against measurements some comments about the measurements must be given. It is important to note that the uppermost measurement point is in a depth of 0.15 m, while further three points are placed at depths of 0.3, 0.6 and 0.9 m. In order to have initial values from these points for the given soil-model, the value at 0.15 m depth is used to be valid in the uppermost active model layer with its thickness of 0.1 m, while a vertical mean taken from the three lowest points is assumed to be valid in the second active soil-model layer.

Fig. 5.29 demonstrated that these values seem to be unsuitable for the model validation. At least, it can be seen that for the uppermost layer the curve derived from measurements differs significantly from the LLM-simulation. The reason is that the upper measurement point with its depth of 0.15 m is not appropriate to be used in the upper soil-model layer having a depth of 0.1 m. But it is unavoidable to do so. As one can see this kind of initialization error seems incidentally diminished due to considerable precipitation on 1 June 1998. The model simulation shows a more believable result in the upper layer compared to the measured values (which are provided every 10 minutes). Already in the afternoon of that first day a strong shower led to a considerable increase of the soil moisture in the upper layer from 8 %vol. to about 20 %vol. As a consequence, the second integration day started from a much higher soil moisture value while the measured one remained much smaller from a rather slow growth rate. On the second day no precipitation occurred. This led to a decrease of soil-moisture. Measurements, however, indicated a further slow increase. The moisture was obviously transported downwards with some delay. After a further moisture increase from precipitation on 3 June the upper model layer dried out over the next days down to 7 % vol. The degree of drying out seems to be caused by a small plant cover of 0.27 due to assumed grassland. That decrease is, however, not continuous and shows a diurnal course.

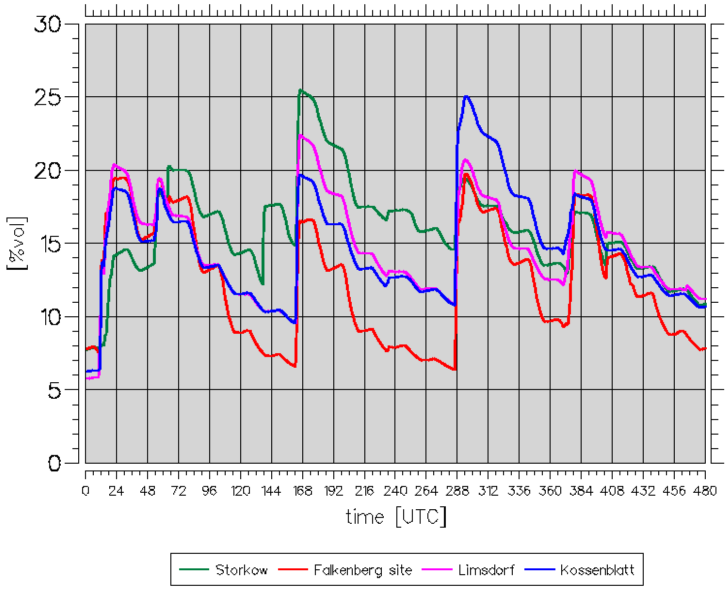

Figure 5.30: Time series of LLM-simulated soil moisture at different locations within the LLM area from 1 June - 20 June 1998.

Here, we drop a further quantitative discussion in this way.

In general, it should be noticed that the soil moisture of the uppermost layer in the model indicates a very sensitive response to precipitation, and it tends to be either significantly higher or smaller than the measured values. From that point of view we have made the decision to initialize each 24-hour run with a simulated moisture value, while the virtue of the measurement is not obvious as long as it is recorded actually 5 cm deeper than the 10-cm thickness of the uppermost soil-model layer. In case of the second active layer a comparison between measured and simulated values cannot be qualified although they show a slightly contrary trend.

Coming to an end, in Fig. 5.30 we show to what extent the soil-moisture can vary over the LLM-integration area as the result of simulations over the above mentioned 20-day LITFASS-98 period as in the previous Fig 5.29. In Fig. 5.30 the same time-variation of the soil-moisture from the uppermost layer at the Falkenberg measurement site is shown and further curves from three selected locations (Fig. 5.31) are added to demonstrate the possible inhomogeneity following from LLM-integrations. The added places are the stations Storkow, Limsdorf and Kossenblatt, where on average over the LITFASS-98 simulation period relative maxima of precipitation occurred.

The corresponding curves in Fig. 5.30 are a sample from the inhomogeneous soil-moisture distribution demonstrating one aspect of a great manifold of results from the rather extensive simulations with the LLM. The simulated soil-moisture variations in time and location indicate the result of a complex interplay between the processes in the soil, in the near-surface atmospheric region and at the interface between both subsystems. Here, these special results were shown first of all to complete the description and documentation of the present state of the LLM implying a great variety of aspects, theories and pragmatic concepts in strict relation to the observational potential and the richness of an elaborated data-pool due to the LITFASS project.

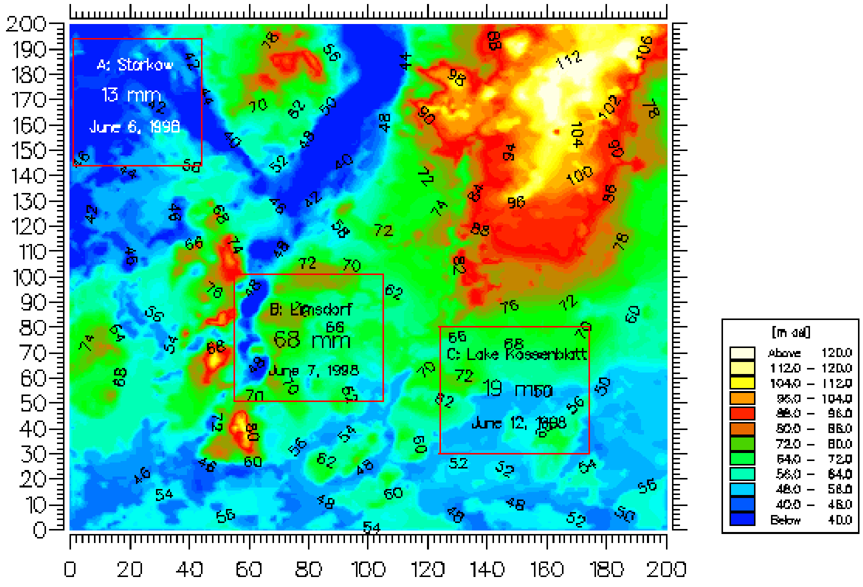

Figure 5.31: Locations with measured maximum precipitation sums over the LITFASS-98 simulation period.

References

Arakawa, A., 1984: Boundary conditions in limited-area models. *Short- and Medium Range Weather Prediction Research Publ. Series*, No. 13, 403-433.

Bailey, W. C., and J. A. Davies, 1980: Bulk stomatal resistance control on evaporation. Agricultural Canada Research Station, Beaverlodge, Alberta Department of Geography, Mc. Master University Hamilton, Ontario.

Beyrich, F. (ed.), 2000: LITFASS-98 Experiment 25.05.1998-30.06.1998. *Experiment Report, Deutscher Wetterdienst, Forschung und Entwicklung, Arbeitsergebnisse Nr. 62*, 78 p.

Binder, P., and H.-J. Herzog, 1995: A radiative upper boundary condition in for a 3-dimensional meso-γ-scale NWP model. *Res. Activities in Atmosph. and Ocean, Modelling Rep. No. 21*, WMO/TD-No. 665.

Bougeault, Ph., 1983: A non-reflective upper boundary condition for limited-height hydrostatic models. *Mon. Wea. Rev.*, 111, 420-429.

Brown, A. R., S. H. Derbyshire, and P. J. Mason, 1994: Large-eddy simulation of stable atmosheric boundary layers with a revised stochastic subgrid model. *Q. J. R. Meteorol. Soc.*, 120, 1485-1512.

Brücher, W., 1997: Numerische Studien zum Mehrfachnesting mit einem nicht-hydrostatischen Modell. *Mitteilungen aus dem Institut für Geophysik und Meteorologie der Universit zu Köln.* Heft 119.

Chen, J. H., 1973: Numerical boundary conditions and computational modes. *J. of Comput. Physics*, 13, 522-535.

Chlond, A., 1999: Grobstruktursimulation- eine Methode zur Berechnung turbulenter atmosphärischer Strömungen. *Max-Planck-Institut für Meteorologie, Examensarbeit Nr. 66*, Hamburg, Juli 1999, 181 S.

Davies, H. C., 1976: A lateral boundary formulation for multi-level prediction models. *Quart. J. R. Met. Soc.*, 102, 405-418.

Davies, A., W. Schertzer, and M. Nunez, 1975: Estimating global solar radiation. *Boundary-Layer Meteorology*, 9, 33-52.

Doms, G., and U. Schättler, 1999: The Nonhydrostatic Limited-Area Model LM (Lokal Modell) of DWD. Part I: Scientific Documentation, Prelim. Vers. LM_F90, Jan. 1999, 169 p., Deutscher Wetterdienst, Geschäftsbereich Forschung und Entwicklung, Postbox 100465, D-63004, Offenbach, Germany; available at *www.cosmo-model.org.*

Görsdorf, U., F. Beyrich, H. Dier, U. Leiterer, J. Güldner, and H.-J. Herzog, 2000: Composite vertical profiles of wind, temperature and humidity for use in numerical modelling. *Extended Abtracts of 5th Int. Symposium on Tropospheric Profiling: Needs and Technology*, pp.65-68, Adelaide, Australia.

Herzog, H.-J., 1995: Testing a radiative upper boundary condition in a nonlinear model with hybrid vertical coordinate. *Meteorol. and Atmosph. Phys.*, 55, 185-204.

Herzog, H.-J., and A. Fiedler, 1999: Bericht über 3D semi-implizite Testläufe mit einer LES-Version des Lokalmodells. Internal Working Report, August 1999.

Hierold, W., U. Schumacher, R. Ziethen and D. Becker, 1977: Bodenübersichtskarte für das LITFASS-Gitterelement Lindenberg des DWD. Zentrum für Agrarlandschafts- und Landnutzungsforschung e.V., Forschungsstation Eberswalde.

Ikawa, M., and K. Saito, 1991: Description of a nonhydrostatic model developed at the forecast research department of the MRI. *Techn. Reports of the Met. Res. Institute*, No. 28, Dec. 1991, 238 p.

Jacobsen, I., and E. Heise, 1982: A new economic method for the computation of the surface temperature in numerical models. *Contrib. Atm. Phys.*, 55, 128-141.

Jürrens, R., 1996: Parameterisierung der Gebietsverdunstung zur Verwendung in meso- und makroskaligen meteorologischen Simulationsmodellen. *Berichte des Instituts für Meteorologie und Klimatologie der Universität Hannover*, Band 53.

Kallberg, P. W., and J. K. Gibson, 1977: Lateral boundary conditions for a limited area version of the EMWF-model. *The GARP Programme on Numerical Experimentation, Report No. 44*, 103-105.

Kanak, K. M., D. K. Lilly, and J. T. Snow, 2000: The formation of vertical vortices in the convective boundary layer. *Q. J. R. Meteorol. Soc.*, 126, 2789-2810.

Klemp, J. B., and R. D. Durran, 1983: An upper boundary condition permitting internal gravity wave radiation in numerical mesoscale models. *Mon. Wea. Rev.*, 111, 430-444.

Klemp, J. B., and R. B. Wilhelmson, 1978: The simulation of three-dimensional convective storm dynamics. *J. Atm. Sci.*, 35, 1070-1096.

Löpmeier, F. J., 1983: Agrarmeteorologisches Modell zur Berechnung der aktuellen Verdunstung (AMBAV). *Beiträge zur Agrarmeteorologie*, Nr. 7, Deutscher Wetterdienst, Zentrale agrarmeteorologische Forschungsstelle Braunschweig.

Mason, P. J., 1994: Large-eddy simulation: A critical review of the technique. *Q. J. R. Meteorol. Soc.*, 120, 1-26.

Mason, P. J., and A. R. Brown, 1999: On Subgrid Models and Filter Operations in Large Eddy Simulations. *J. Atm. Sci.*, 56, 2101-2114.

Miller, M. J., and A. J. Thorpe, 1981: Radiation conditions for the lateral boundaries of limited-area numerical models. *Quart. J. R. Met. Soc.*, 107, 615-628.

Miyakoda, K., and A. Rosati, 1977: One-way nested grid models: The interface conditions and the numerical accuracy. *Mon. Wea. Rev.*, 105, 1072-1107.

Müller, E. et al., 1995: LITFASS - a nucleus for a BALTEX field experiment. *Deutscher Wetterdienst, Forschung und Entwicklung, Arbeitsergebnisse Nr. 33*, 17 p.

Orlanski, J., 1976: A simple boundary condition for unbounded hyperbolic flows. *J. of Comput. Physics*, 21, 251-269.

Perkey, D. J., and C. W. Kreitzberg, 1976: A time dependent lateral boundary scheme for limited area primitive equation models. *Mon. Wea. Rev.*, 104, 744-755.

Podlasly, Ch., and F. Berger, 1999: Bereitstellung von Strahlungsgrössen aus NOAA- und METEOSAT-Messungen für den Strahlungsantrieb des LLM. Abschlussbericht zum DWD-Projekt MOP/63/98. Technische UniversitätDresden, Institut für Hydrologie und Meteorologie, Lehrstuhl für Meteorologie.

Rietschel, 1994: Raumklimatechnik, Band 1 Grundlagen. Hrsg.: Esdorn, H., Springer-Verlag, Berlin Heidelberg New York.

Rosenow, W., 1998: Personal communication.

Saito, K., G. Doms, U. Schättler, and J. Steppeler, 1998: 3-D Mountain Waves by the Lokal-Modell of DWD and the MRI Mesoscale Nonhydrostatic Model. *Papers in Meteorol. and Geophys.* 49, 1, 7-19.

Scotti, A., C. Meneveau, and D. K. Lilly, 1993: Generalized Smagorinsky model for anisotropic grids. *Phys. Fluids*, A5 (9), 2306-2308.

Scotti, A., C. Meneveau, and M. Fatica, 1997: Dynamic Smagorinsky model on anisotropic grids. *Phys. Fluids*, 9 (6), 1856-1858.

Skamarock, W. C., and J. B. Klemp, 1992: The stability of time-split numerical methods for the hydrostatic and the nonhydrostatic elastic equations. *Mon. Wea. Rev.*, 120, 2109-2127.

Smagorinsky, J., 1963: General circulation experiments with the primitive equations: 1. The basic experiment. *Mon. Wea. Rev.*, 91, 99-164.

Stevens, D. E. et al., 2000: Small-Scale Processes and Entrainment in a Stratocumulus Marine Boundary Layer. *J. Atm. Sci.*, 57, 567-581.

Stull, R. B., 1988: An introduction to boundary layer Meteorology. Kluwer Academic Publishers, Dordrecht/Boston/London, 666 p.

Thomas, S., and C. Girard, 1998 a: Semi-implicit scheme for the DWD LM model. Internal Working Report, August 1998, 27 p.

Thomas, S., C. Girard, and R. Benoit, 1998 b: A new adiabatic Kernel for the MC2 model. *Atmosphere-Ocean*, 36(3), 241-270.

Uchijima, Z., 1976: Maize and rice. In: J.L. Monteith, Ed.: Vegetation and the atmosphere, Volume 2, Academic Press London.

VDI Guideline 1994: Wechselwirkungen zwischen Atmosphäre und Oberflächen. Berechnung der kurz- und langwelligen Strahlung. *Verein Deutscher Ingenieure VDI 3789 Blatt 2*, Oktober 1994.

Vogelgesang, R., 1993: Agrarmeteorologisches Modell zur Berechnung von aktueller Verdunstung und Bodenfeuchte. *Deutscher Wetterdienst, Abteilung Agrarmeteorologie, FE-Vorhaben AM 1 -Nr. 85/01.*

Zimmermann, F., 1994 a: Biotopkartierung Brandenburg - Kartierungsanleitung. Landesumweltamt Brandenburg, Potsdam.

Zimmermann, F., 1994 b: Biotopkartierung Brandenburg - Erfassungsstand und Umsetzung. *Naturschutz und Landschaftspflege*, Heft 2, Potsdam.

An Epilogue to Part I

Although in the Introduction announced that the entire LLM-report will contain nine Chapters, the presented Part I with its first five Chapters may be already reason enough to us for some comments and acknowledgements. First of all, the authors dedicate their paper to Dr. E. Müller. He gave the decisive impetus to the LITFASS-project, and it was particularly his basic idea to determine near-surface turbulent fluxes over a realistic inhomogeneous area like Lindenberg by use of a high-resolving nonhydrostatic simulation model. It was a great challenge for us to start working in this field and to bring that task till to the present state. We will not deny our feeling to have worked not only hard over a longer time but to have also always been conscious of taking part in a DWD-pilot project of sustainable meaning, where all the investment over that project time is now available to connect observatory capacity immediately with the urgent needs of NWP - and to have contributed so far with our efforts in this line. We appreciate very much E. Müller's productive impatience, criticism and his permanent interest over most of the project time until his retirement.

Furthermore, all the countless working meetings and discussions in various circles of colleagues from the NWP modelling groups of the Research/Development field and the Observatory Lindenberg have been indispensible. In that way a close cooperation with Dr. E. Heise, the leader of the NWP-parameterization group, must be emphasized, who himself was involved in the LITFASS-project from the very beginning. In the first years of the project Prof. Th. Foken has been the leader and coordinator. After that, Dr. F. Beyrich's intensive conduction of LITFASS brought us great benefit due to his indivisible sense of responsibility both for the measurement - and the simulation component. Concerning important details, we are thankful to Prof's H. Fortak, G. Groß and to Dr. A. Dörnbrack for several hints, advices and their general interest to our topic. Almost all extensive LLM-integrations has been carried out at the ECMWF. The care for the great many of series of LLM-runs was excellent. We are very grateful to the people in the Computing Centre there, who were involved with our jobs. In particular, N. Kreitz from the User Support has actually supported us very intensively.

Concerning ourselves, the first author was told to be responsible for the whole LLM-subproject of LITFASS, while he is also responsible for the subjects of Chapters 1-4 and 7 in Part II. Dr. G. Vogel is responsible for the content of Chapter 5 and in Part II for Chapters 6 and 8. Mrs. Dr. U. Schubert's contributions are overlapping. She has solved all problems of programming and program organization concerning the specific LLM-problem of external real-data updating at low, lateral and upper boundaries, and moreover, she has organized and managed all computing runs at ECMWF, the postprocessing there included. She wrote Chapter 9 about the LLM-computing problems. Mrs. A. Fiedler is responsible for all programs in parallel code contained in Chapters 2-4 (lateral boundary technique, inclusion of 3D-turbulent flux termes, TKE-SGS model) and for preparing all Figures in these Chapters. Mrs. R. Kirchner's contributions and untiring efforts concern the widespread delivery and preparation of model- and measurement data necessary for the LLM and for different purposes of validation. Finally, the authors are very grateful to Mrs. E. Sulz for her reliable assistance in the wide field of postprocessing and to Mrs. Ch. Baudach, who wrote the text in that final form.

List of COSMO Newsletters and Technical Reports

(available for download from the COSMO Website: www.cosmo-model.org)

COSMO Newsletters

Newsletter No.1, February 2001.

Newsletter No.2, February 2002.

COSMO Technical Reports

No. 1, Dmitrii Mironov and Matthias Raschendorfer (2001): *Evaluation of Empirical Parameters of the New LM Surface-Layer Parameterization Scheme. Results from Numerical Experiments Including the Soil Moisture Analysis.*

No. 2, Reinhold Schrodin and Erdmann Heise (2001): *The Multi-Layer Version of the DWD Soil Model TERRA_LM.*

No. 3, Günther Doms (2001): *A Scheme for Monotonic Numerical Diffusion in the LM.*

No. 4, Hans-Joachim Herzog, Ursula Schubert, Gerd Vogel, Adelheid Fiedler and Roswitha Kirchner (2002): *LLM – the High-Resolving Nonhydrostatic Simulation Model in the DWD – Project LITFASS. Part I: Modelling Technique and Simulation Method.*

COSMO Technical Reports

Issues of the COSMO Technical Reports series are published by the *Consortium for Small-Scale Modelling* at non-regular intervals. COSMO is a European group for numerical weather prediction with participating meteorological services from Germany (DWD, AWGeophys), Greece (HNMS), Italy (UGM, ARPA-SMR) and Switzerland (MeteoSwiss). The general goal is to develop, improve and maintain a non-hydrostatic limited area modelling system to be used for both operational and research applications by the members of COSMO. This system is initially based on the Lokal-Modell (LM) of DWD with its corresponding data assimilation system.

The Technical Reports are intended

- for scientific contributions and a documentation of research activities,
- to present and discuss results obtained from the model system,
- to present and discuss verification results and interpretation methods,
- for a documentation of technical changes to the model system,
- to give an overview of new components of the model system.

The purpose of these reports is to communicate results, changes and progress related to the LM model system relatively fast within the COSMO consortium, and also to inform other NWP groups on our current research activities. In this way the discussion on a specific topic can be stimulated at an early stage. In order to publish a report very soon after the completition of the manuscript, we have decided to omit a thorough reviewing procedure and only a rough check is done by the editors and a third reviewer. We apologize for typographical and other errors or inconsistencies which may still be present.

At present, the Technical Reports are available for download from the COSMO web site (www.cosmo-model.org). If required, the member meteorological centres can produce hardcopies by their own for distribution within their service. All members of the consortium will be informed about new issues by email.

For any comments and questions, please contact the editors:

Günther Doms
guenther.doms@dwd.de

Ulrich Schättler
ulrich.schaettler@dwd.de